Tuning Anomalous Hall effect and Spin Polarized Current in Magnetic Ultrathin Films

by

Bochao Li

A Dissertation Presented in Partial Fulfillment
of the Requirements for the Degree
Doctor of Philosophy

Approved November 2018 by the
Graduate Supervisory Committee:

Tingyong Chen, Chair
Robert Nemanich
Peter Bennett
Quan Qing

ARIZONA STATE UNIVERSITY

December 2018

ABSTRACT

In this dissertation I studied the anomalous Hall effect in MgO/Permalloy/Nonmagnetic Metal(NM) based structure, spin polarized current in YIG/Pt based thin films and the origin of the perpendicular magnetic anisotropy(PMA) in the Ru/Co/Ru based structures.

The anomalous Hall effect is the observation of a nonzero voltage difference across a magnetic material transverse to the current that flows through the material and the external magnetic field. Unlike the ordinary Hall effect which is observed in nonmagnetic metals, the anomalous Hall effect is only observed in magnetic materials and is orders of magnitude larger than the ordinary Hall effect. Unlike quantum anomalous Hall effect which only works in low temperature and extremely large magnetic field, anomalous Hall effect can be measured at room temperature under a relatively small magnetic field. This allows the anomalous Hall effect to have great potential applications in spintronics and be a good characterization tool for ferromagnetic materials especially materials that have perpendicular magnetic anisotropy(PMA).

In my research, it is observed that a polarity change of the Hall resistance in the MgO/Permalloy/NM structure can be obtained when certain nonmagnetic metal is used as the capping layer while no polarity change is observed when some other metal is used as the capping layer. This allows us to tune the polarity of the anomalous Hall effect by changing the thickness of

a component of the structure. My conclusion is that an intrinsic mechanism from Berry curvature plays an important role in the sign of anomalous Hall resistivity in the MgO/Py/HM structures. Surface and interfacial scattering also make substantial contribution to the measured Hall resistivity.

Spin polarization(P) is one of the key concepts in spintronics and is defined as the difference in the spin up and spin down electron population near the Fermi level of a conductor. It has great applications in the spintronics field such as the creation of spin transfer torques, magnetic tunnel junction(MTJ), spintronic logic devices.

In my research, spin polarization is measured on platinum layers grown on a YIG layer. Platinum is a nonmagnetic metal with strong spin orbit coupling which intrinsically has zero spin polarization. Nontrivial spin polarization measured by ARS is observed in the Pt layer when it is grown on YIG ferromagnetic insulator. This result is contrary to the zero spin polarization in the Pt layer when it is grown directly on SiO_2 substrate. Magnetic proximity effect and spin current pumping from YIG into Pt is proposed as the reason of the nontrivial spin polarization induced in Pt. An even higher spin polarization in the Pt layer is observed when an ultrathin NiO layer or Cu layer is inserted between Pt and YIG which blocks the proximity effect. The spin polarization in the NiO inserted sample shows temperature dependence. This demonstrates that the spin current

transmission is further enhanced in ultrathin NiO layers through magnon and spin fluctuations.

Perpendicular Magnetic Anisotropy(PMA) has important applications in spintronics and magnetic storage. In the last chapter, I study the origin of PMA in one of the structures that shows PMA: Ru/Co/Ru. By measuring the ARS curve while changing the magnetic field orientation, the origin of the PMA in this structure is determined to be the strain induced by lattice mismatch.

To My Parents

ACKNOWLEDGMENTS

I would like to thank my advisor Dr. Tingyong Chen for his guidance throughout my Ph.D study.

I would also thank the support and guidance from colleagues inside the group and outside the group including Gejian Zhao, Ji Zhang, Jessica Gifford, Dr. Dongrin Kim, Miguel Bueno and Charles Snider, Dr. Chufeng Li and many others.

Many thanks to Professor Peter Bennett, Professor Robert Nemanich and Professor Quan Qing for being my committee member and advising me on my thesis.

Lastly I want to greatest gratitude to my parents for their selfless support during my Ph.D study.

TABLE OF CONTENTS

CHAPTER Page

LIST OF FIGURES

Figure Page

Figure Page

Figure Page

Figure Page

Figure Page

Chapter 1

Introduction

In this chapter, I will make an introduction to the theoretical background in my thesis. Magnetism is one of the most important properties of materials. It is a study of interaction between materials and magnetic field. The phenomena of magnetism had been observed by people in ancient times and a typical example of early applications of magnetism is compass which leads to the discovery of new continents. Even nowadays, magnetism plays an important role in hard drive and magnetic memory devices.

1.1 Magnetic materials

When a material is placed in a magnetic field, the material will be affected by the magnetic field called magnetized. The degree that the material is magnetized is described by a vector M, the dipole moment per unit volume. If we assume that the magnetization is proportional to the external applied magnetic field H, which can be written as:

$$\boldsymbol{M} = \chi \boldsymbol{H} \tag{1.1}$$

The proportionality constant χ is known as the magnetic susceptibility of the given material[1].

Materials may be grouped into different types depending on the sign and magnitude of χ. When χ is negative, that is when the induced magnetization is opposite to $\boldsymbol{H}$, then the material is called diamagnetic. When χ is positive and small, the materials are known as paramagnetic materials. When χ is a very large positive number, the materials can be ferromagnetic or ferrimagnetic materials.

Diamagnetism is caused by the response of the orbital electrons to the external magnetic field. Classically, if we consider an electron circulating around the nucleus, the orbiting angular frequency can be calculated according to Newton's second law:

$$\mathrm{F} = \mathrm{m}\omega_0^2 r \tag{1.2}$$

The F is the attractive Coulomb force between the electron and the nucleus. The magnetic moment of the electron can be written as:

$$\mu_0 = IA = \frac{e}{2}\omega_0 r^2 \tag{1.3}$$

If we assume a magnetic field is applied perpendicular to the plane of the electron orbit, then in addition to the Coulomb attraction of the nucleus, the electron experiences a Lorentz force of the external magnetic field which points radially outward:

$$\mathrm{F} - \mathrm{eBr}\omega = \mathrm{m}\omega^2 r \tag{1.4}$$

Due to the additional Lorentz force, the angular frequency ω is now different from ω_0. In the limit of the small field, the new frequency can be calculated as:

$$\omega = \omega_0 - \frac{eB}{2m} \tag{1.5}$$

We can see that frequency becomes smaller because of the applied field and the corresponding magnetic moment also becomes smaller, from (2.3) we can calculate that the change in magnetic moment[1]:

$$\Delta\mu = -\left(\frac{e^2r^2}{4m}\right)B \tag{1.6}$$

We can see that the induced moment is opposite the magnetic field, hence called diamagnetic material.

Apart from orbital electrons, conduction electrons in conductors also contribute to diamagnetism. In the presence of external magnetic field, the conduction electrons do cyclotron motion, quantum mechanical treatment needs to be employed to calculate the conduction electron's contribution to diamagnetism[1].

The diamagnetic susceptibility can be observed in solids with full atomic shells such as rear gas crystals and ionic crystals. In such solids, the orbital and spin moment all cancel out so there is no paramagnetic contribution. In solids with incompletely filled shells, paramagnetic effect is dominant and much stronger than diamagnetism, so diamagnetic contribution is smeared out[1].

Paramagnetism exists in atoms with incompletely filled atomic shells. Such atoms usually exhibit nonzero angular and spin moment and they combine together to form the total magnetic moment of the atom. If the external magnetic field is present, the total moment will precession along the axis of the external field, showing a positive magnetization along the external field. The total magnetic moment can be written as[2]:

$$\boldsymbol{\mu} = \mathrm{g}\left(-\frac{e}{2m}\right)\boldsymbol{J} \tag{1.7}$$

$\boldsymbol{J}$ is total angular momentum of the orbital electrons which includes the contributions of all the orbital and spin angular momentums and g is called Lande factor which depends on the relative orientations of the orbital and spin angular momentum. When an external magnetic field is applied, Zeeman splitting results. The Zeeman energy can be calculated as:

$$\mathrm{E} = -\boldsymbol{\mu} \cdot \mathbf{B} = \mathrm{g}\mu_B B m_j \tag{1.8}$$

The energy depends on the magnetic quantum number m_j. Without magnetic field, Atoms with different m_j have same energy called degeneracy, after the application of external field, the degeneracy is lifted. We only consider the simple case where $\boldsymbol{J} = \frac{1}{2}$ so m_j can take the value of $+\frac{1}{2}$ or $-\frac{1}{2}$, resulting in double Zeeman splitting. If we consider that N1 and N2 are numbers of atoms with magnetic quantum number $-\frac{1}{2}$ and $+\frac{1}{2}$ respectively and N1+ N2=N where N is the total number of atoms. According to Boltzmann statistics, the

distribution of atoms in each state obeys Boltzmann distribution and the two populations are related by[2]:

$$\frac{N_2}{N_1} = e^{-\Delta E/kT} \tag{1.9}$$

The magnetization M is given by:

$$M = g\mu_B(N_1 - N_2) = Ng\mu_B \tanh(\frac{g\mu_B B}{kT}) \tag{1.10}$$

For a weak field, under approximation $\tanh(x) \approx x$, we can calculate the susceptibility of paramagnetic materials as[2]:

$$\chi = \frac{\mu_0 N(g\mu_B)^2}{kT} \tag{1.11}$$

From equation (2.10) we can see that at weak external field, M is linearly proportional to B, but as field becomes stronger, M saturate at the value of $Ng\mu_B$, this is the case when all the dipoles of the site atoms align with the field, it can also happen when temperature T approaches to zero.

The above paragraph shows site atoms contribution to paramagnetism. This paragraph we will show that conduction electron also make contribution to paramagnetism. A lot of metals show paramagnetism and this comes from the contribution of conduction electrons. The paramagnetic contribution of conduction electrons arises from the spin while the diamagnetic contribution of conduction electrons come from their orbital motion as has discussed above. Conduction electron paramagnetism arises from the fact that the spin magnetic moment of conduction electrons tends to align with the external

magnetic field. Deeper understanding can be realized by taking into account the Fermi-Dirac distribution[2][3].

As can be found in Figure 1, if no external magnetic field is applied, there are equal numbers of spin-up and spin-down electrons, resulting a zero net magnetization. When the external field is applied along z-axis, the energy of the electrons parallel to the field will be lowered by $\mu_B B$ while those antiparallel to the field will be raised by $\mu_B B$. To ensure thermal equilibrium, some of the electrons at the Fermi level will change from antiparallel to parallel configuration, leading to a net magnetization of the conduction electrons. Please note that electrons far away from the Fermi level is frozen by the Pauli-exclusion principle and thus cannot make the flip. Therefore, paramagnetism originated from conduction electrons can only be explained by quantum mechanical considerations.

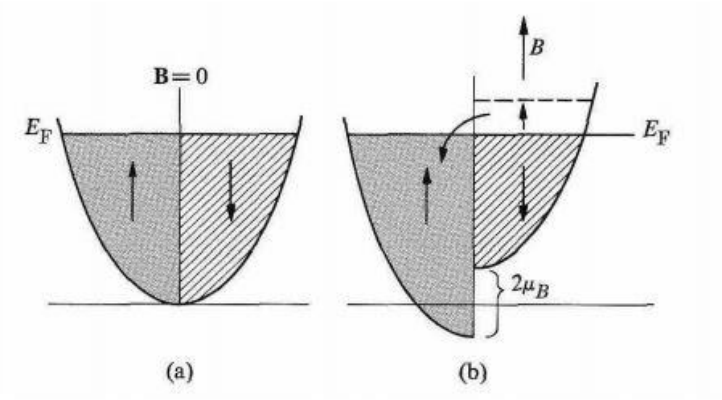

Figure 1.1 Illustration of spin paramagnetism[10]

To estimate the magnetic susceptibility, assume that only electrons within the energy interval of $\mu_B B$ around the Fermi level participate the

flipping, their concentration is given by $N_{eff} = \frac{1}{2} g(E_F)\mu_B B$, where $g(E_F)$ is the density of state at the Fermi level. Because each flip increases the magnetization by $2\mu_B$, the net magnetization can be given by[1]:

$$\boldsymbol{M} \approx N_{eff} 2\mu_B = \mu_B^2 g(E_F) B \tag{1.12}$$

So the paramagnetic susceptibility is[1]:

$$\chi_p \approx \mu_0 \mu_B^2 g(E_F) \tag{1.13}$$

From equation (2.13) we can see that the paramagnetic susceptibility is essentially independent of temperature, this arises from the fact that in Fermi-Dirac distribution, only electrons near the Fermi level can be thermally excited and flipped by the magnetic field, electrons far away from Fermi level are essentially frozen by quantum effect.

Ferromagnetism arises from the phenomenon of spontaneous magnetization. Ferromagnetic materials can be found in both metals and insulators. For ferromagnetism in insulators, the molecular magnetic moment is aligned in some favorable directions in the crystal and the molecular field model is employed to describe the phenomena. The model implies the presence of an internal field to produce the spontaneous magnetization. The field is assumed to arise from the interaction between molecules and is proportional to the magnetization. Ferromagnetism in metals are usually found in transition metals and rear-earth metals. These elements have partially filled 3d or 4f shells and the conduction electrons in these shells contribute to the ferromagnetic property. Itinerant-electron model is used to describe the

ferromagnetism in metals. If we assume that the element has partially filled 3d band and we can divide it into two subbands, each representing the two spin orientations. If we assume the exchange interaction exists and this tend to align the spin in the up direction and this will help the electrons to transfer from down to up direction to lower the energy. This will results in unbalanced subbands and a net magnetization and the result is the saturation magnetization observed in ferromagnetism[2].

Ferromagnetism only appear below a certain temperature and this temperature is denoted as Curie temperature T_C, the magnitude of T_C is about 1000 K but each material has its own T_C. Above T_C, the thermal excitation breaks the long range order and no ferromagnetism is observed, in fact the material under this temperature region exhibits paramagnetic property. If the temperature falls below T_C, spontaneous magnetization is observed and the lower the temperature, the stronger the spontaneous magnetization[2].

Apart from ferromagnetism, there are other two types of magnetic order which we call antiferromagnetism and ferrimagnetism respectively. In ferromagnetism if the temperature is below Curie temperature, all spins are assumed to be aligned in the same direction. In antiferromagnetism, all spin dipoles are assumed to have same moment but adjacent spins point to opposite direction resulting in a zero net magnetization. Antiferromagnetism can be found in many compounds involving transition metals but cannot be found in pure elements. In these compounds, ions at different lattice positions have

opposite easy magnetization axis, resulting in zero net magnetization. In ferrimagnetism neighboring dipoles point to the opposite direction but the moments are not equal. In this case the moments cannot cancel each other completely and resulting in a nonzero net magnetization. Figure 2 is a brief illustration of the three types of magnetic order discussed above[3].

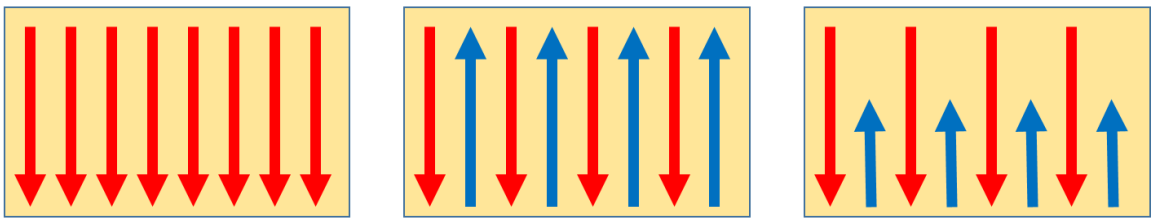

Figure 1.2 (a) Ferromagnetism (b) Antiferromagnetism (c) Ferrimagnetism

Many applications in our daily lives can be found using magnetic materials. For example, soft magnetic materials can be found in the transformers, motors and generators. Besides, hard magnetic materials play an important role in applications that require large coercivity [1]. Magnetic materials also have important applications in data storage devices. With the development in nanoscience technology, the advantage of magnetic technology over the conventional charge storage technology has become more and more manifest because of the low energy consumption and non-volatile property found in these devices[2].

1.2 Hall Effect

1.2.1 Ordinary Hall Effect

The Hall effect is discovered by Edwin Hall in John Hopkins University. Later, people discovered many more different kinds of Hall effects such as Anomalous Hall Effect, Quantum Hall Effect, Spin Hall Effect etc. In normal Hall effect, charge current passing through a conductor under a magnetic field will experience a Lorentz force by the magnetic field. This force is perpendicular to the magnetic field and the current flow direction. The charge carriers care deflected to the side of the sample, a measurable electric voltage will be observed across the sample. In the steady state, the electric force due to the charge accumulation will cancel out the Lorentz force. We can deduce the Hall voltage as[1][2][3]:

$$V_H = \frac{I_x B_z}{nte} \tag{1.14}$$

The Hall voltage in ordinary Hall effect is linearly proportional to the external magnetic field and inversely proportional to the thickness of the sample. The Hall resistance is defined as the Hall voltage divided by the current. We can also deduce the Hall coefficient as[3]:

$$r_H = \frac{1}{ne} \tag{1.15}$$

The Hall coefficient in the ordinary Hall effect is inversely proportional to the density of the charge carrier. Also, the Hall coefficient can be positive or negative, depending on the type of the charge carrier in the conductor.

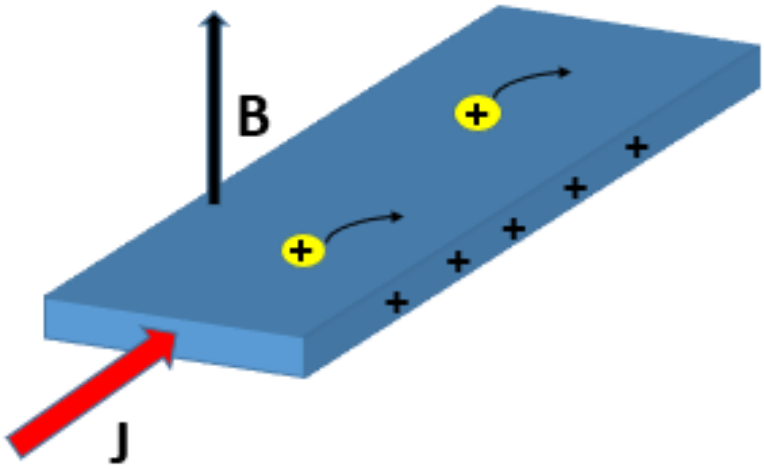

Figure 1.3: Schematic diagram about Ordinary Hall Effect

1.2.2 Anomalous Hall Effect

The anomalous Hall effect can be discovered in magnetic metals and is much stronger than the ordinary Hall effect[5]. The underlying mechanism of AHE is different from that in OHE. In the AHE, the charge carriers in the material is deflected due to the magnetization of the material, not the external magnetic field although the magnetization can be induced by the external field. In AHE, electrons of opposite spins are deflected to the two side of the sample due to the spin-orbit coupling. The Hall resistivity in AHE can be written as[4][5][6]:

$$\rho_H = R_0 H + 4\pi R_s M \tag{1.16}$$

The second term is the AHE contribution to the Hall resistivity. It depends on the magnetization of the sample and R_s is the intrinsic property of the sample. In magnetic materials, the dependence of M on external magnetic field is hysteresis loop, therefore the dependence of Hall resistivity in AHE on external field is no longer linear but shows hysteresis loop.

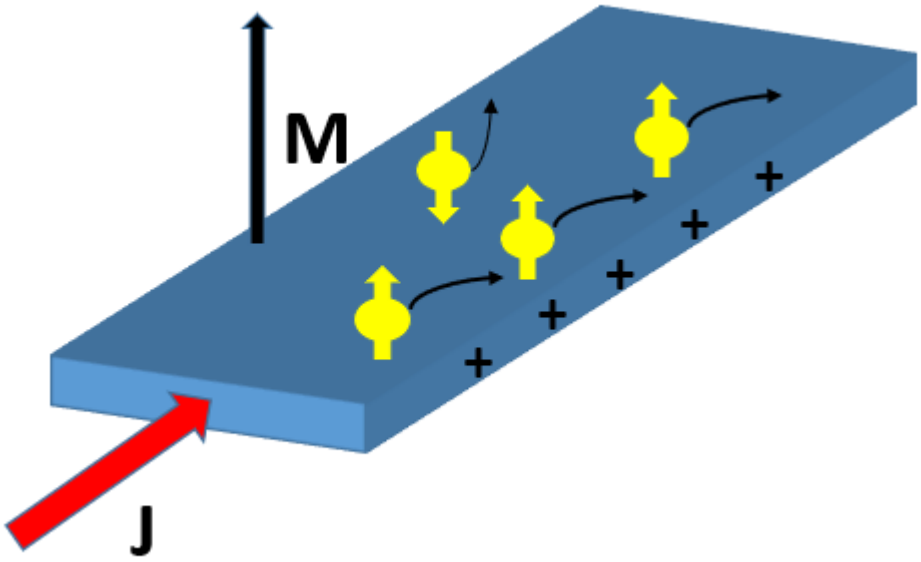

Figure 1.4: Schematic diagram about Anomalous Hall Effect

1.2.3 Spin Hall Effect

The Spin Hall Effect is different from OHE and AHE because it happens without external magnetic field purely due to spin-orbit coupling. It happens in nonmagnetic metal with no external field required. When a charged current

pass through this material, equal numbers of electrons with opposite spins are deflected to two opposite edges of the sample through spin orbit coupling. Because the same numbers of electrons accumulate on two edges of the sample due to spin Hall Effect, the spin Hall effect cannot be measured by electrical equipment such as voltmeter[7][8].

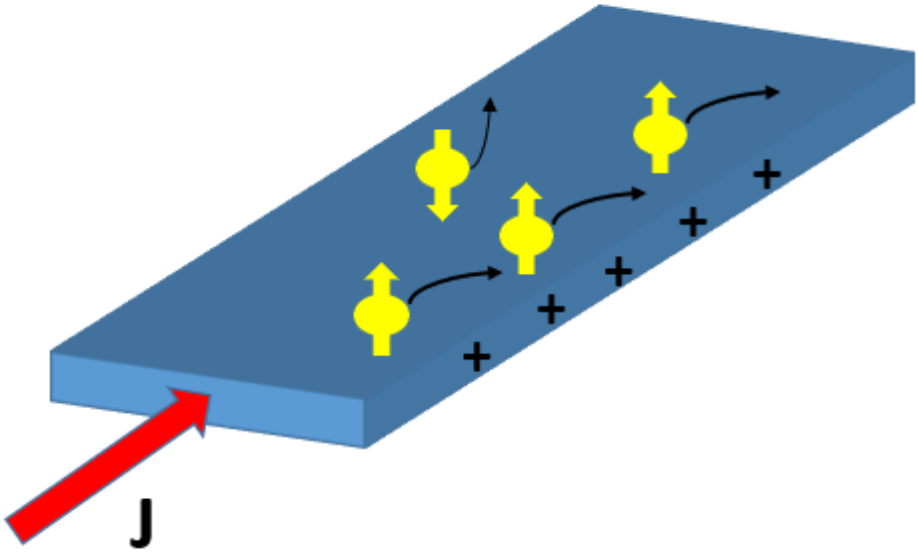

Figure 1.5: Schematic diagram about Spin Hall Effect.

1.2.4 Spin-Orbit Coupling

The spin-orbit coupling is the main mechanism in AHE and SHE. The spin-orbit coupling can happen in single atoms and in crystal solids. For the spin-orbit coupling in single atoms, considering an electron orbiting a nucleus. If we go to the rest frame of the electron, this is equivalent to the nucleus orbiting the electron. The motion of the nucleus charge creates a

circulating current and there is a corresponding magnetic field. The spin of the electron couples with this magnetic field creating an additional energy term. This is the big picture of spin-orbit coupling in single atoms. For the spin-orbit coupling in solids, the electrons move in crystal solids will feel the electric fields of the lattice potential, in the rest frame of the electron, this is transformed into magnetic field. The spin of the electron couples with the magnetic field giving an additional energy term. The electrons will be deflected to different directions with different spin orientation[6][9].

1.2.5 Mechanisms of Anomalous Hall Effect

The detailed theoretical mechanism of Anomalous Hall effect has been conducted by many condensed matter theorists. The current theories propose that there are three mechanisms that causes the Anomalous Hall Effect: Intrinsic Mechanism, Skew Scattering and Side Jump[6].

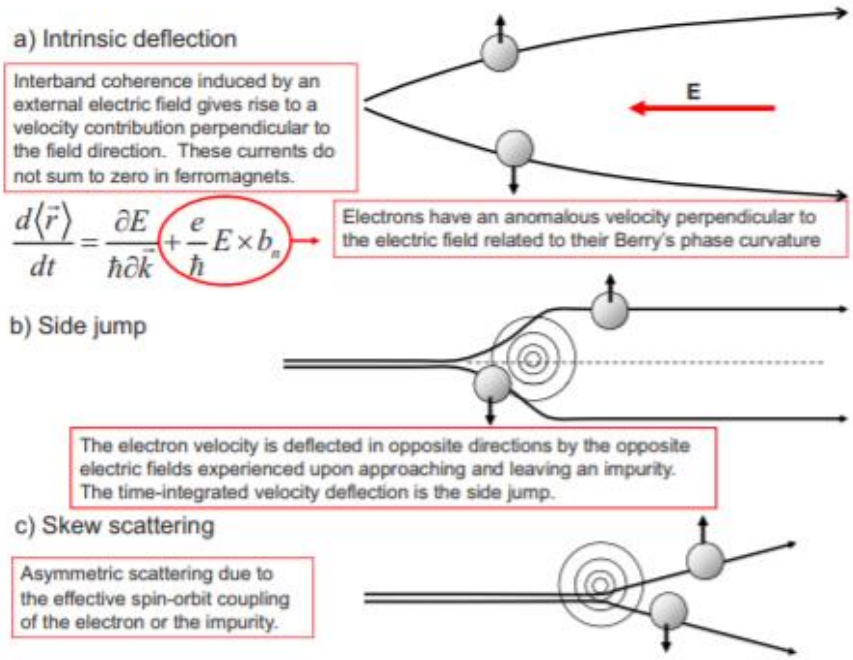

Figure 1.6: Illustration of three mechanisms of Anomalous Hall effect[6]

The intrinsic mechanism is the first theoretical explanation of the Anomalous Hall effect introduced by Karplus and Luttinger[6]. It is considered as the most important contribution to anomalous Hall effect. It claims that the AHE originates from the spin-orbit interaction in Bloch bands in crystals. It is due to crystalline structure not to impurities thus called intrinsic mechanism. Later it was found that the intrinsic mechanism is actually caused by the Berry curvatures in momentum space and can be expressed as the sum of the berry curvatures in the momentum space[11-14].

Now it is agreed that the intrinsic contribution to the anomalous Hall effect is pure quantum mechanical in nature due to the Berry curvature in momentum space and can be quantitatively analyzed if the exact band structure of the magnetic material can be calculated[36]. Considering a system

described by the Hamiltonian H which also depends on a set of external parameters $\mathbf{R}(t)$. The Hamiltonian can thus be written as $H(\mathbf{R}(t))$. At each time t, the instantaneous eigenstate and the corresponding energy levels of this Hamiltonian is written as $|n(\boldsymbol{R})>$ and $\varepsilon_n(\boldsymbol{R})$ respectively. In the adiabatic approximation in which the external parameter is assumed change very slowly with time, if the system starts from one of the eigenstates, it will remain in this time dependent eigenstate during the time evolution plus a phase factor. It can be written as:

$$|\psi_n(t)> = e^{i\gamma_n(t)}\exp[-\frac{i}{\hbar}\int_0^t \varepsilon_n(\boldsymbol{R}(t'))dt'] \times |n(\boldsymbol{R}(t))> \tag{1.17}$$

The first phase factor is called berry phase and is generally nonzero in quantum mechanics. The second phase factor is called dynamic phase factor which depends on time. If we insert this equation back to the time dependent Schrodinger equation that governs the system:

$$H\big(\boldsymbol{R}(t)\big)|\psi_n(t)> = i\hbar\frac{\partial}{\partial t}|\psi_n(t)> \tag{1.18}$$

The exponential in the Berry phase factor can be solved for:

$$\gamma_n(t) = \int_C \; d\boldsymbol{R}\cdot\boldsymbol{\mathcal{A}}_n(\boldsymbol{R}) \tag{1.19}$$

The term $\boldsymbol{\mathcal{A}}_n(\boldsymbol{R})$ is a vector valued function in parameter space and is called Berry connection. It can be calculated by the following equation:

$$\boldsymbol{\mathcal{A}}_n(\boldsymbol{R}) = i < n(\boldsymbol{R})|\frac{\partial}{\partial \boldsymbol{R}}|n(\boldsymbol{R})> \tag{1.20}$$

We can see that the Berry connection is purely an intrinsic property that is governed by the adiabatic time dependent Hamiltonian of the system. During

the time evolution if the system goes through a closed path in the parameter space and returns to the original Hamiltonian at time t, the Berry phase factor can be written as:

$$\gamma_n(t) = \oint d\boldsymbol{R} \cdot \boldsymbol{\mathcal{A}}_n(\boldsymbol{R}) \tag{1.21}$$

We can see that even though the Hamiltonian goes back to its original state, the Berry phase is generally given by a closed line integral and is generally not zero. This means that the quantum state of the system generally doesn't go back to the original state in adiabatic evolution due to the Berry phase factor.

We have seen that the Berry connection is a vector valued function in parameter space. One can define another vector valued function which is called Berry curvature and can be written as:

$$\Omega^n_{\mu\nu} = \frac{\partial}{\partial R^\mu}\,\mathcal{A}^n_\nu(\boldsymbol{R}) - \frac{\partial}{\partial R^\nu}\,\mathcal{A}^n_\mu(\boldsymbol{R}) = i[\left\langle \frac{\partial n(\boldsymbol{R})}{\partial R^\mu} \middle| \frac{\partial n(\boldsymbol{R})}{\partial R^\nu} \right\rangle - (\nu \leftrightarrow \mu)] \tag{1.22}$$

From the above equation and the fact that $< \frac{\partial n}{\partial \boldsymbol{R}} | n' > (\varepsilon_n - \varepsilon_{n'}) =< n| \frac{\partial H}{\partial \boldsymbol{R}} | n' >$, one can derive another equation to calculate the Berry curvature:

$$\Omega^n_{\mu\nu}(\boldsymbol{R}) = i \sum_{n' \neq n} \frac{\langle n|\partial H/\partial R^\mu|n'\rangle\langle n'|\partial H/\partial R^\nu|n\rangle - (\nu \leftrightarrow \mu)}{(\varepsilon_n - \varepsilon_{n'})^2} \tag{1.23}$$

The Berry phase factor can be written in terms of Berry curvature instead of the Berry connection by using the Stokes' theorem:

$$\gamma_n(t) = 0.5 \int_S \; dR^\mu \wedge dR^\nu \, \Omega^n_{\mu\nu}(\boldsymbol{R}) \tag{1.24}$$

The S is the surface enclosed by the closed loop C. If the parameter space is three dimensional as is the case of the momentum space in lattice, the

definition of Berry curvature can be simplified as the curl of the Berry connection:

$$\boldsymbol{\Omega}_n(\boldsymbol{R}) = \nabla_{\boldsymbol{R}} \times \boldsymbol{\mathcal{A}}_n(\boldsymbol{R}) \tag{1.25}$$

The expression of the Berry phase in terms of the Berry curvature can also be simplified to a vector valued surface integral:

$$\gamma_n(t) = 0.5 \int_S \, d\boldsymbol{S} \cdot \boldsymbol{\Omega}_n(\boldsymbol{R}) \tag{1.26}$$

Now the Berry curvature is a vector valued function and can be related to the Berry curvature tensor via the Levi-Civita symbol $\Omega^n_{\mu\nu} = \epsilon_{\mu\nu\xi}(\Omega_n)_\xi$.

Now we can discuss the Berry curvature in lattice crystals and we can see that Berry curvature can give rise to an anomalous current transverse to the electric field that contribute to the anomalous Hall effect. In anomalous Hall effect measurement, electrical current passes through the material due to the external applied constant electric field $\mathbf{E}$. In order to incorporate the electric field into the Hamiltonian without breaking the translational symmetry of the lattice, we can use the gauge transformation to express the electric field in terms a time dependent vector potential $\mathbf{A}$(t):

$$H(t) = \frac{[\hat{\boldsymbol{p}} + e\boldsymbol{A}(t)]^2}{2m} + V(\boldsymbol{r}) = H\left(\boldsymbol{q} + \frac{e}{\hbar}\boldsymbol{A}(t)\right) = H(\boldsymbol{q}, t) \tag{1.27}$$

Now the parameter momentum $\mathbf{q}$ and time t can be viewed as the independent parameters and we can denote its instantaneous eigenstates as $|u_n(\boldsymbol{q}, t)>$. If we assume that initially the system starts at $|u_n>$ and the entire process is adiabatic, the time dependent wave function can be given by:

$$|u_n\rangle - i\hbar \sum_{n' \neq n} \frac{|u_{n'}\rangle\langle u_{n'}|\partial u_n/\partial t\rangle}{\varepsilon_n - \varepsilon_{n'}} \tag{1.28}$$

Using Hamilton mechanics the velocity can be given by:

$$v_n(\boldsymbol{q}) = \frac{\partial \varepsilon_n(\boldsymbol{q})}{\hbar \partial \boldsymbol{q}} - i\left[\left\langle \frac{\partial u_n}{\partial \boldsymbol{q}} \middle| \frac{\partial u_n}{\partial \boldsymbol{t}} \right\rangle - \left\langle \frac{\partial u_n}{\partial t} \middle| \frac{\partial u_n}{\partial \boldsymbol{q}} \right\rangle\right] = \frac{\partial \varepsilon_n(\boldsymbol{q})}{\hbar \partial \boldsymbol{q}} - \Omega_{ql}^n \tag{1.29}$$

The second term is the Berry curvature term which is incorporated into the velocity of the charge carrier. If we introduce another momentum vector $\mathbf{k} = \boldsymbol{q} + \frac{e}{\hbar}\boldsymbol{A}(t)$, the system can be written in terms of $\mathbf{k}$ instead of $\mathbf{q}$, the velocity can be written as:

$$v_n(\boldsymbol{k}) = \frac{\partial \varepsilon_n(\boldsymbol{k})}{\hbar \partial \boldsymbol{k}} - \frac{e}{\hbar}\boldsymbol{E} \times \boldsymbol{\Omega}_n(\boldsymbol{k}) \tag{1.30}$$

The second term is the Berry curvature contribution to the current, we can see that it is always perpendicular to the electric field which is exactly the behavior of the Hall current. Thus we can see that the anomalous Hall current may come directly from the intrinsic quantum property of the lattice structure without depending on any extrinsic interference.

It is known that only ferromagnetic materials exhibit anomalous Hall effect while nonmagnetic metals only have ordinary Hall effect, therefore not all materials have that extra Berry curvature term that contribute to the Hall conductivity. The Berry curvature term in a crystal can be analyzed on the symmetrical bases. Ideal crystal band under single electron approximation possesses both time reversal symmetry and spatial inversion symmetry. Under

time reversal symmetry, both $\mathbf{v}$ and $\mathbf{k}$ changes sign while $\mathbf{E}$ is fixed, the Berry curvature term is required to obey:

$$\boldsymbol{\Omega}_n(-\boldsymbol{k}) = -\boldsymbol{\Omega}_n(\boldsymbol{k}) \tag{1.31}$$

Under spatial inversion symmetry $\mathbf{v}$, $\mathbf{k}$ and $\mathbf{E}$ all change signs and the Berry curvature term is required to obey:

$$\boldsymbol{\Omega}_n(-\boldsymbol{k}) = \boldsymbol{\Omega}_n(\boldsymbol{k}) \tag{1.32}$$

Combine the above two equations we can find that if the system has both time reversal symmetry and spatial inversion symmetry, the Berry curvature is zero $\boldsymbol{\Omega}_n(\boldsymbol{k}) = 0$. As a result, the anomalous Hall effect only arises in materials in which the time reversal symmetry and spatial inversion symmetry are not both conserved. In ferromagnetic material, the ferromagnetic ordering due to the spin orbit coupling breaks the time reversal symmetry, this can give rise to a nonzero Berry curvature term and anomalous Hall effect[36].

The Hall conductivity can be expressed in terms of Berry curvature by integrating in the Brillouin zone and summing over all occupied bands. If we only consider the Hall conductivity in the x-y plane, we can only use the z component of the Berry curvature and the conductance can be given by[37]:

$$\sigma_{xy} = \frac{e^2}{\hbar} \int \frac{d^3k}{(2\pi)^3} \sum_n f_{nk} \Omega_n^z(\boldsymbol{k}) \tag{1.33}$$

From above we can see that the intrinsic contribution to anomalous Hall effect can be calculated by integrating and summing over all occupied bands below the Fermi energy. By employing the Stokes' theorem, the volume integral can be converted into a surface integral of the Berry vector potential on the Fermi surface[36][38].

Detailed band structure and Berry curvature calculation of fcc Fe has been calculated by Yao et al. using the full potential linearized augmented plane wave method with the generalized gradient approximation(GGA) method.

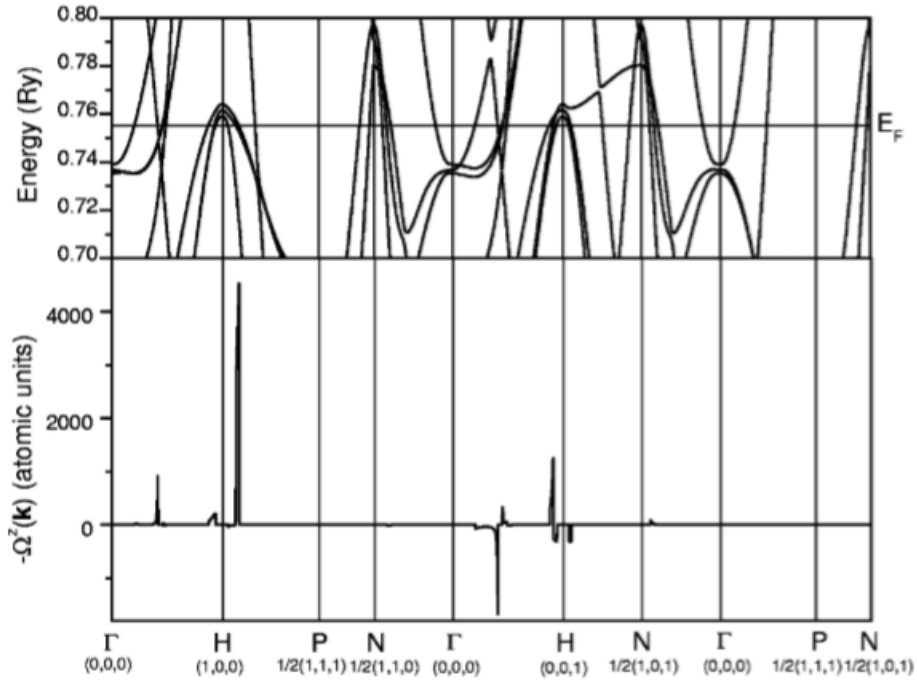

Figure 1.7: Band structure and Berry curvature along symmetric line in momentum space[39].

The above is the result of the band structure and Berry curvature calculation by Yao et al. They showed that the Berry curvature shows highly

irregular behavior that both sharp peaks and dips can appear. The sharp irregularities of the Berry curvature originate from pairs of the spin-orbit coupled band in a small k interval[39].

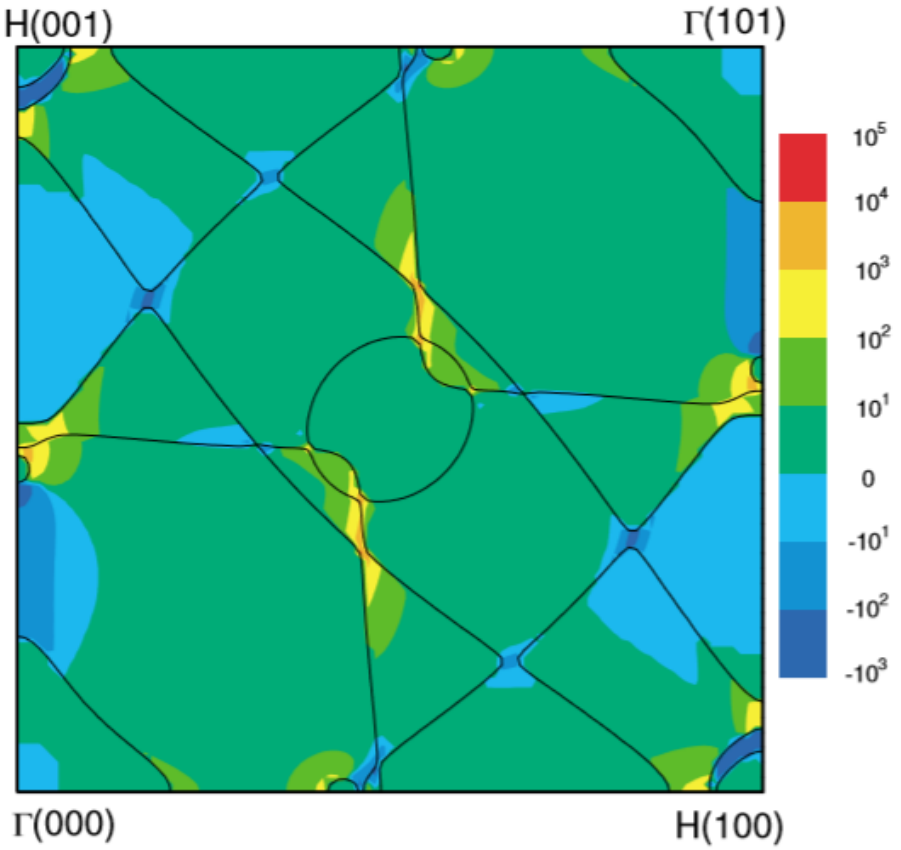

Figure 1.8: The integrated Berry curvature seen from the Fermi surface in (010) plane[36][39].

The above graph is the integrated Berry curvature on the (010) Fermi surface of fcc Fe. As can be seen from the graph, the Berry curvature is very small in general k values but shows sharp peak values in areas where the avoided crossing of Fermi lines occur due to spin orbit coupling[39]. It is those small regions that make major contributions to the anomalous Hall effect in

ferromagnetic materials. This result further demonstrates that the spin orbit coupling is crucial behind anomalous Hall effect.

Skew scattering is another important effect that contributes to anomalous Hall effect. The mechanism of skew scattering is spin-orbit interaction of electrons with the impurities. The moving electrons will experience the electric field of the impurities and in the rest frame of the electrons, this is equivalent to a moving magnetic field. The electrons with different spin orientation is deflected to different directions. In skew scattering, the scattering amplitude of the electrons with opposite spins to two sides of the material is not equal, thus comes the net electron accumulation across the material and the Hall voltage. The skew scattering theory proposes that there is a linear relationship between the AHE resistivity and the longitudinal resistivity of the material[6][15],

$$\rho_{AHE} \propto \rho_{xx} \tag{1.34}$$

The last contribution to anomalous Hall effect is side jump. Like the skew scattering mechanism, side jump is also caused by the unequal scattering of spin up and spin down electrons by impurities or disorders in the crystal. The electron can be viewed as Gaussian wave packet in quantum mechanics. When a Gaussian wave packet incident on a spherical impurity potential and scattered, if spin orbit coupling term is considered, there will be a displacement of the wave packet transverse to the incident direction. The

AHE resistivity cause by the side jump mechanism is proportional to the square of the longitudinal resistivity[6][16][17],

$$\rho_{AHE} \propto \rho_{xx}^2 \tag{1.35}$$

1.2.6 Recent works in Anomalous Hall effect

A lot of works has been done about the anomalous Hall effect in bulk magnetic materials and pure magnetic thin films. In particular, a sign change in anomalous Hall conductivity has been observed in various structures such as $CuCrSe_{1-x}Br_x$(the doping of Br in CuCrSe spinel)[36][37] and Co/Pd multilayer structures. Also, using the general gradient approximation plus on-site Coulomb interaction(GGA+U) and (GGA) methods, Fuh et al. have calculated the band structure and anomalous Hall conductance of the fcc Ni. They changed the Fermi level while fix the band structure and showed that the Hall conductivity can be positive and negative while varying the Fermi level. This result further corroborates the theory by Haldane that the anomalous Hall conductivity is a Fermi surface effect and depends sensitively on the Fermi surface[40].

In recent years, people also studied the AHE in ferromagnetic/nonmagnetic(FM/NM) multilayer structures. It was found that besides bulk contribution from ferromagnetic metals, FM/NM interface scattering and surface scattering also play a substantial role in the AHE resistivity[20-33]. The magnetic multilayers studied includes: Co/Au[20],

Co/Cu[21], Co/Pt[22], Fe/Gd[23], Fe/Cr[24], MgO/(Co/Pt)n/MgO[25], Pt/Co/Ru[26][27] and Co/Pd[28-33] etc.

In Fe/Cr multilayer structures, the Hall resistivity vs longitudinal resistivity was found to follow $\rho_{AHE} \propto \rho_{xx}^{1.8\sim2.2}$ which deviates from the intrinsic mechanism which states that $\rho_{AHE} \propto \rho_{xx}^{2}$. The Hall coefficient in Fe/Cr multilayers differs considerably from that in bulk materials as a consequence of the interface scattering and antimagnetic coupling[24]. In Co/Au superlattices, with tuning the Co and Au layer thickness, perpendicular magnetic anisotropy(PMA) can be obtained. The magnetoresistance and Hall voltage in the structure that exhibits PMA is orders of magnitude larger than in the structure that shows in plane magnetic anisotropy[20]. In Co/Pt and [Pt/Co]/Ru/[Co/Pt] superlattices, strong PMA can all be obtained by tuning the layer thickness. The PMA is attributed to the hybridization between the 3d Co orbitals and the 5d Pt orbitals at the interface. The relationship between the Hall resistivity and the longitudinal resistivity all deviates from the square law which indicates that the AHE is dominated by the interface scattering[22][26][27]. Ultrasensitive anomalous Hall effect has been identified in SiO2/Fe-Pt/SiO2 sandwich structure which is attributed to interfacial electron scattering[34]. The Co/Pd multilayer structure has been most extensively studied. Not only can the PMA obtained by manipulating the Co thickness, the polarity of the AHE signal can also be achieved by thickness manipulation[28-33]. In Co/Pd

bilayers, the anomalous Hall conductivity increases roughly linearly with Co thickness suggesting the interfacial scattering contribution to the AHE signal. The AHE signal due to the interface scattering has opposite sign to that due to the bulk contribution[28]. In Co/Pd multilayer systems, study has found that bulk, interface scattering and surface scattering all contribute to the overall anomalous Hall resistivity. The AHE due to surface scattering has opposite sign to that from interface scattering. This results in the polarity change in the AHE signal in the temperature dependent AHE measurement and the multilayer with different repetition. The change in polarity was also claimed to originate from the change in the position of the Fermi level of the 3d bands in the Co/Pd multilayer structure[32][33].

1.3 Spin Polarization

Due to the Pauli exclusion principle for Fermions, the electrons in deep energy bands are frozen and only electrons near the Fermi level can be excited and contribute to the conductivity. The Spin polarization is defined as the difference in the density of states of spin up and spin down electrons near the Fermi Level. The formula is given by:

$$\mathrm{P} = \frac{N_{\uparrow}(E_f) - N_{\downarrow}(E_f)}{N_{\uparrow}(E_f) + N_{\downarrow}(E_f)} \tag{1.36}$$

For nonmagnetic metals, there are equal number of spin up and spin down electrons near the Fermi level, so that the spin polarization P=0. For another

extreme case half metal, all electrons near the Fermi level has only one spin orientation therefore the spin polarization P=1. For general ferromagnetic metals, the spin polarization is in the range 0<P<1.

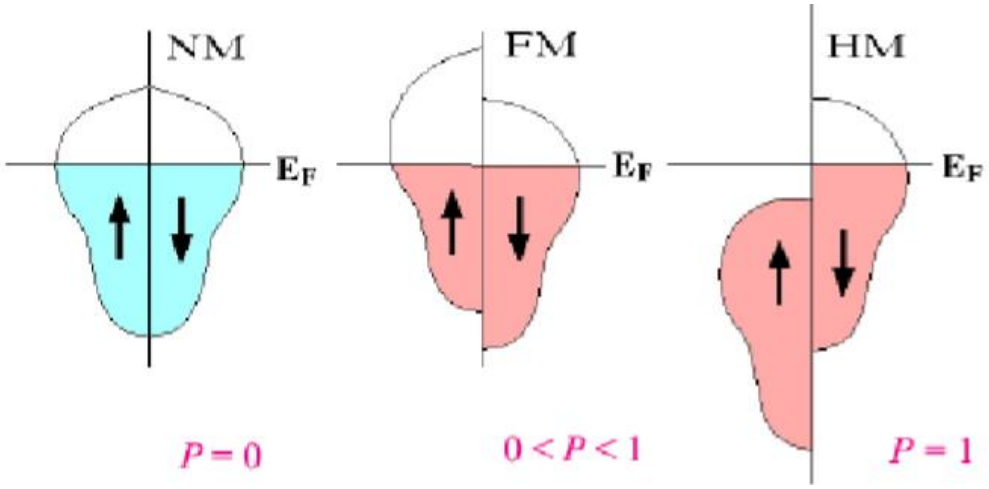

Figure 1.9: (a)Nonmagnetic metals have spin polarization P=0. (b) Ferromagnetic metals have spin polarization 0<P<1. (c)Half metals have spin polarization P=1.

The above equation only applies for the ideal case namely the material to be measured is perfect bulk crystals. In our lab, we use point contact to measure the spin polarization of the material, the equation has to be modified for specific measuring technique. For very small contact size area, the contact area can smaller than the mean free path of the electrons, this is in the ballistic region. One has the spin polarization equation[18]:

$$\mathrm{P} = \frac{N_{\uparrow}(E_f)v_{\uparrow f} - N_{\downarrow}(E_f)v_{\downarrow f}}{N_{\uparrow}(E_f)v_{\uparrow f} + N_{\downarrow}(E_f)v_{\downarrow f}} \tag{1.37}$$

The $v_{\uparrow f}$ and $v_{\downarrow f}$ are Fermi velocities at the Fermi level. In large contact area which is in diffusive region, the equation is modified as[18]:

$$P = \frac{N_{\uparrow}(E_f)v_{\uparrow f}^2 - N_{\downarrow}(E_f)v_{\downarrow f}^2}{N_{\uparrow}(E_f)v_{\uparrow f}^2 + N_{\downarrow}(E_f)v_{\downarrow f}^2} \quad (1.38)$$

1.4 Andreev Reflection Spectroscopy

Andreev reflection occurs at the interface of a normal metal and superconductor when they are in contact with one another. When an electrical current is sent in to travel from the normal metal to the superconductor through the interface, a certain is converted into a supercurrent while the other left considered nonequilibrium charge Q*. The nonequilibrium charge can relax into supercurrent over the charge relaxation distance.

There are several cases in the current tunneling at the normal metal and superconductor interface. Classically, there is always a high barrier at the normal metal-superconductor interface so some of the electrons transform into nonequilibrium charge Q*. By considering the quasiparticles injected into the superconductor and the corresponding injection rate, we can calculate the fraction of the charge current transformed into Q*. At very low temperature near absolute zero and the bias voltage across the interface roughly equal the superconducting gap eV=Δ, the entire current converts into the supercurrent and not to the nonequilibrium charge because there are an equal number of electron and hole mixture. If the bias voltage is much higher

than the superconducting gap eV> Δ, there are some percent of the current transform into nonequilibrium charge Q*. If eV>> Δ, almost all current is in the form of nonequilibrium charge Q*. The fraction of current in the nonequilibrium charge state varies from zero to unity as the bias voltage increases from the value of superconducting gap to infinity[18][19].

For another case where the ideal interface is assumed. In this scenario, there is no potential barrier, the tunneling process is dominated by a mechanism called Andreev reflection named after Andreev. For very low temperature and bias voltage across the interface much lower than the superconducting gap eV<< Δ, the electrons passing through the interface of the normal metal and superconductor cannot enter as quasiparticle but reflected back as hole. In the meantime, two electrons two electrons with opposite orientation of spins transmit into the superconductor as cooper pairs. This process is called Andreev reflection and each electron transfers two charges, as a result the differential conductance is doubled than that in the normal state. In the case eV>> Δ or higher temperature where T ~ Tc, nearly all the charges pass through as nonequilibrium charges Q* thus the differential conductance is the same as that in the normal state. As temperature decreases from above Tc to 0, the fraction of electrons transform to nonequilibrium charges drop from 1 to 0 and the differential conductance double[18][19].

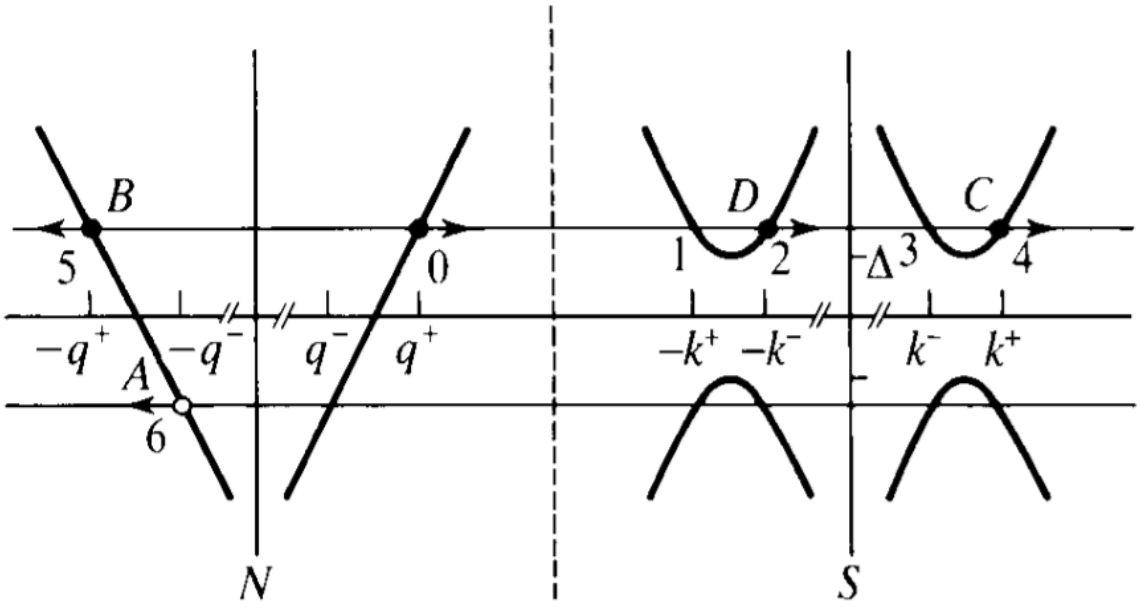

Figure 1.10: The Andreev reflection process. The circles and dots are holes and electrons respectively[19].

No potential barrier is only the ideal case, generally there are always some sort of potential barrier at the superconductor/normal metal interface. This barrier will cause Andreev reflection to be replaced by normal reflection. The potential barrier can be caused by surface oxidation or different fermi velocities between the two materials. To address this issue, Blonder et al. introduced the BTK model which simulate the potential barrier at the interface as a delta function. The strength of the delta function is denoted as Z. The equation associated with this model is called Bogoliubov equation. An electron incident on the interface with energy E can transmit through the interface or Andreev reflected or normally reflected. The possibilities for various outcome can be written as a function of the tunnel barrier Z. This model can simulate the theoretical differential conductance curves for a superconductor/normal metal

junction for different values of Z, ranging from low Z values for pure Andreev reflection to high Z values for normal reflection case. For all of the cases with different Z, when the voltage across the tunnel junction is high, the differential conductance will reduce to that of the normal case[19].

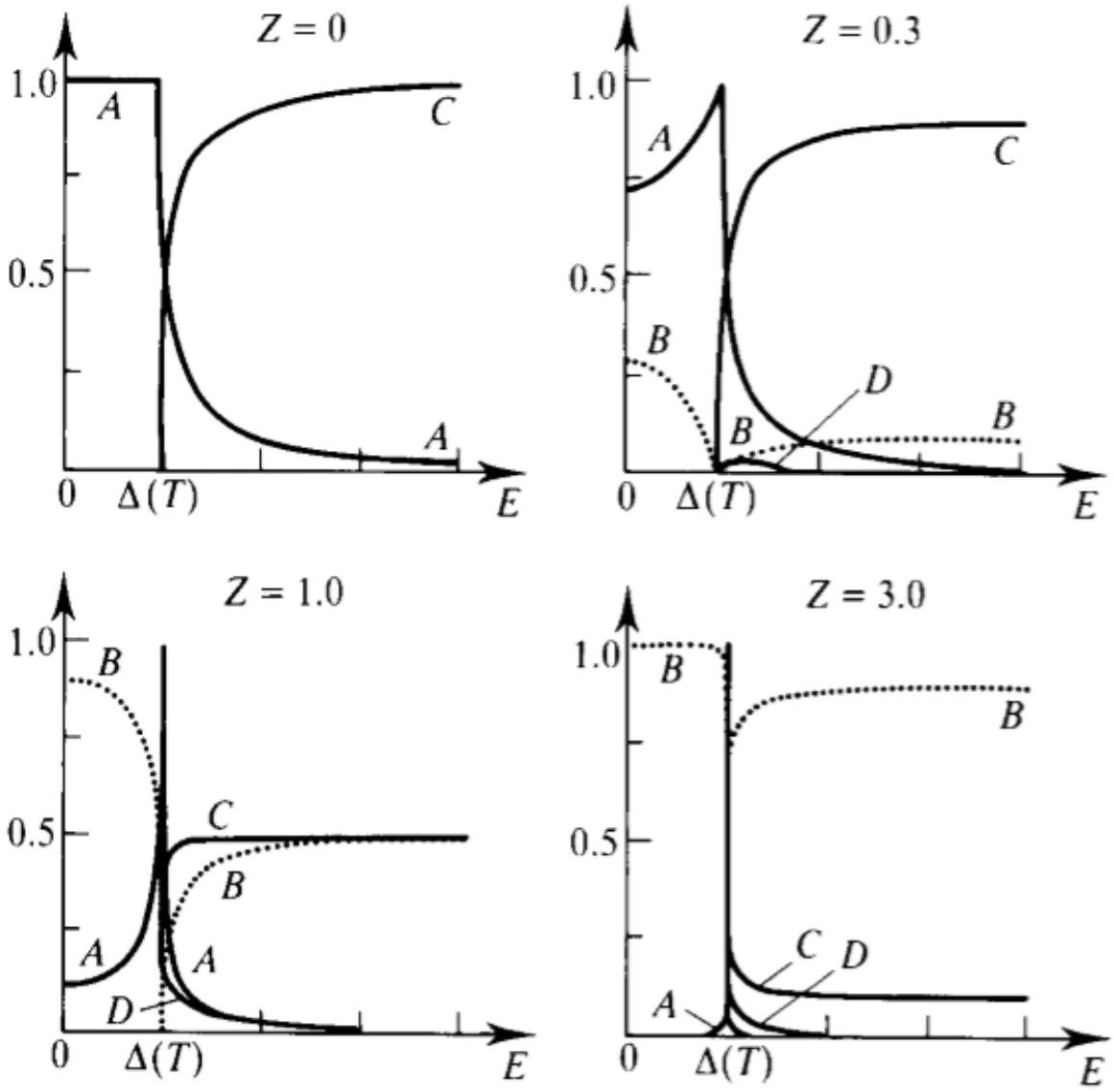

Figure 1.11: Probability for different mechanisms as a function of different values of Z. A denotes Andreev reflection. B denotes normal reflection. C denotes transmission without branch crossing. D denotes transmission with branch crossing[19].

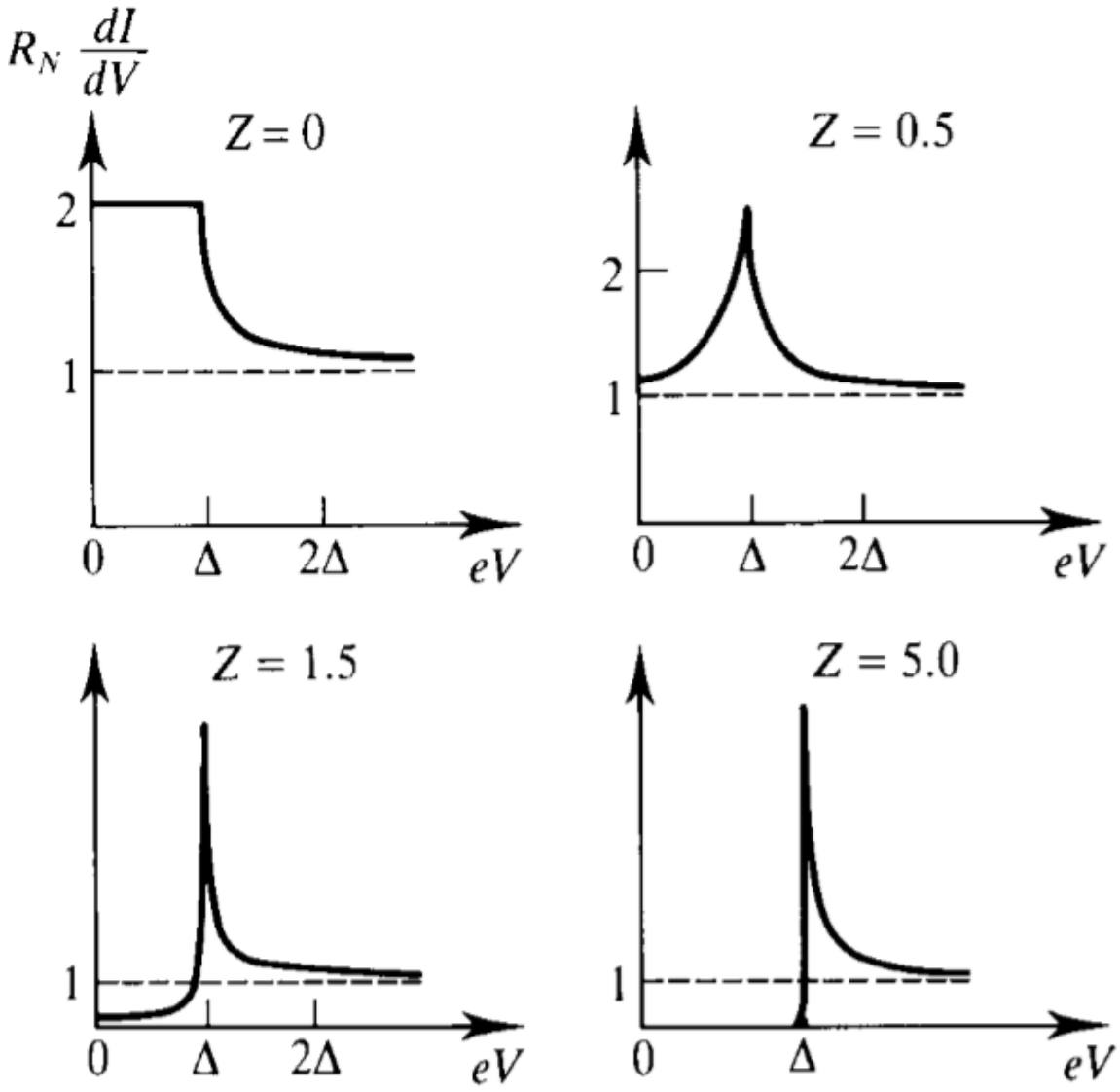

Figure 1.12: Differential conductance curves for various Z factors at T=0. As can be seen, for large bias voltage, all differential conductance saturates to that of the normal case[19].

The Point Contact Andreev Reflection(PCAR) has been a great tool to measure the spin polarization of a given material. The differential conductance vs biased voltage curve which is closely related to the PCAR process can be generated and compared to the result of the BTK model. In real experiments,

the point contact methods create additional resistance that is not related to the ARS process. Especially in my research where the samples are mostly thin films, the additional resistance is quite large compared to the resistance that is related to the ARS. Therefore, the additional resistance has to be taken into account when extracting the ARS information. The additional resistance has the effect of broadening the ARS curves[35]. The effect of the additional resistance on the Pt/YIG structure for different Pt thickness can be seen in Figure 1.11.

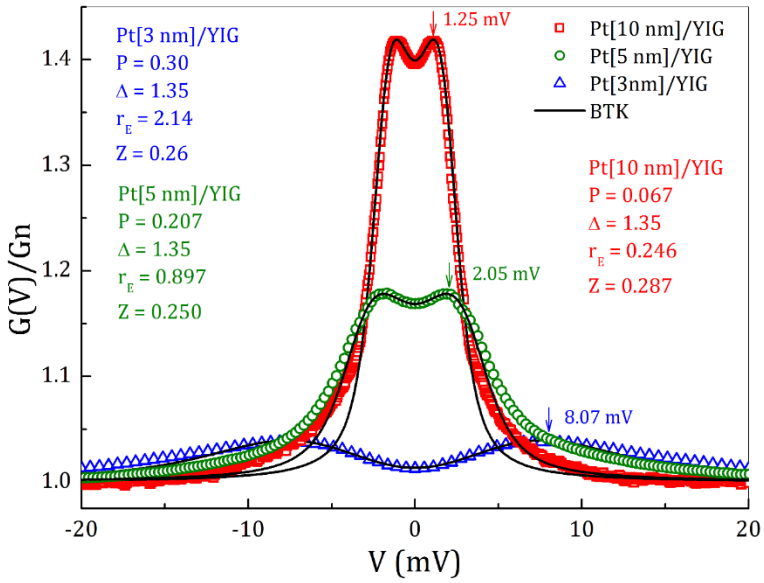

Figure 1.13: The additional resistance of the thin film has the effect of broadening the ARS curve.

REFERENCE

1. Rolf E. Hummel, “Electronic Properties of Materials.”
2. Stephen Blundell, “Magnetism in Condensed Matter.”

3. Charles Kittel, “Introduction to Solid State Physics.”

4. Robert O’Handley, “Modern Magnetic Materials: Principles and Applications.”
5. Soshin Chikazumi, “Physics of Ferromagnetism.”
6. Naoto Nagaosa et al., “Anomalous Hall effect,” reviews of modern physics, volume 82, April–June 2010
7. J. E. Hirsch, “Spin Hall effect”, Phys. Rev. Lett. 83, 1834 (1999)
8. M. I. Dyakonov and V. I. Perel, “Current-induced spin orientation of electrons in semiconductors”, Phys. Lett. A35, 459 (1971)
9. M. Born, “Atomic Physics”, Dover Publications Inc, New York (1989)
10. R. Karplus, J. M. Luttinger, “Hall effect in ferromagnetics” Phys. Rev. 95, 1154 (1954)
11. M. V. Berry, “Quantal phase factors accompanying adiabatic changes”, Proc. R. Soc. Lond. A 392, 45 (1984)
12. M. V. Berry, “Quantal phase factors accompanying adiabatic changes” Proc. R. Soc. 392, 45 (1984)
13. M. C. Chang and Q. Niu, “Berry phase, hyperorbits, and the Hofstadter spectrum: Semiclassical dynamics in magnetic Bloch bands” Phys. Rev. B 53, 7010 (1996)

14. G. Sundaram and Q. Niu, “Wave-packet dynamics in slowly perturbed crystals: Gradient corrections and Berry-phase effects” Phys. Rev. B 59, 14915 (1999)
15. A. Fert and A. Friederich, “Skew scattering by rare-earth impurities in silver, gold, and aluminum” Phys. Rev. B 13, 397 (1976)
16. L. Berger, “Side-Jump Mechanism for the Hall Effect of Ferromagnets” Phys. Rev. B 2, 4559 (1970).
17. N. A. Sinitsyn, "Semiclassical theories of the anomalous Hall effect” J. Phys.: Condens. Matter 20, 023201 (2008).
18. Jessica Gifford, “Andreev Reflection Spectroscopy: Theory and Experiment.”
19. Tinkham et al., “Introduction to Superconductivity.”
20. W Vavra et al., “Magnetoresistance and Hall effect in epitaxial Co-Au superlattices,” Phys. Rev. B 42, 4889 (1990).
21. F. Tsui et al., “Scaling Behavior of Giant Magnetotransport Effects in Co/Cu Superlattices,” PhysRevLett.72.740 (1994)
22. C. L. Canedy, “Extraordinary Hall effect in (111) and (100)-orientated Co/Pt superlattices,” Journal of Applied Physics 81, 5367 (1997)
23. W. J. Xu et al., “Anomalous Hall Effect in Fe/Gd Bilayers,” EPL (Europhysics Letters), Volume 90, Number 2 (2010)
24. S. N. Song et al., “Anomalous Hall effect in (110)Fe/(110)Cr multilayers,” Appl. Phys. Lett. 59, 479 (1991)

25. S. L. Zhang et al., "Large enhancement of the anomalous Hall effect in Co/Pt multilayers sandwiched by MgO layers," Appl. Phys. Lett. 97, 222504 (2010)
26. J. Zhao et al., "Large extraordinary Hall effect in $[Pt/Co]_5/Ru/[Co/Pt]_5$ multilayers," Physical Review B 81, 172404 (2010)
27. C. Christides et al., Journal of Applied Physics 97, 013901 (2005)
28. Z. B. Guo et al., "Effects of surface and interface scattering on anomalous Hall effect in Co/Pd multilayers," Physical Review B 86, 104433 (2012)
29. Xinli Kou et al., "Magnetic anisotropy and anomalous Hall effect of ultrathin Co/Pd bilayers," Journal of Applied Physics 112 093915 (2012)
30. O. Shaya et al., "Extraordinary Hall effect in Co-Pd bilayers," Journal of Applied Physics 102, 043910 (2007)
31. Sangrok Kim et al., "Magnetic properties of Pd/Co multilayer films studied by Hall effect," Journal of Applied Physics 73, 6344 (1993)
32. D. Rosenblatt et al., "Reversal of the extraordinary Hall effect polarity in thin Co/Pd multilayers," Appl. Phys. Lett. 96, 022512 (2010)
33. V. Keskin et al., "Temperature and Co thickness dependent sign change of the anomalous Hall effect in Co/Pd multilayers: An experimental and theoretical study," Appl. Phys. Lett. 102, 022416 (2013)

34. Y. M. Lu et al., “Ultrasensitive anomalous Hall effect in SiO2/Fe-Pt/SiO2 sandwich structure films,” Appl. Phys. Lett. 100, 022404 (2012)
35. T. Y. Chen et al., “Pronounced effects of additional resistance in Andreev reflection spectroscopy”, Physical Review B 81, 214444 (2010)
36. Di Xiao et al., “Berry phase effects on electronic properties”, Reviews of Modern Physics, volume 82, July–September 2010
37. Yugui Yao et al., “Theoretical Evidence for the Berry-Phase Mechanism of Anomalous Hall Transport: First-principles Studies on CuCr2Se4−xBrx”, Phys. Rev. B 75, 020401(R) (2007)
38. F. D. M. Haldane, “Berry Curvature on the Fermi Surface: Anomalous Hall Effect as a Topological Fermi-Liquid Property”, Phys. Rev. Lett. 93, 206602 (2004)
39. Yugui Yao, et. al., “First principles calculation of anomalous Hall conductivity in ferromagnetic bcc Fe”, Phys. Rev. Lett. 92, 037204 (2004).
40. Huei-Ru Fuh et al., “Intrinsic anomalous Hall effect in nickel: An GGA+U study”, PHYSICAL REVIEW B 84, 144427 (2011).
41. David J. Griffiths, “Introduction to Quantum Mechanics”, Prentice Hall (1995).

42. Qi Wang et al., “Large intrinsic anomalous Hall effect in half-metallic ferromagnet $Co_3Sn_2S_2$ with magnetic Weyl fermions”, Nature Communications volume 9, Article number: 3681 (2018)
43. Wei-li Lee et al., “Dissipationless Anomalous Hall Current in the Ferromagnetic Spinel $CuCr_2Se_{4-x}Br_x$”, Science. 2004 Mar 12;303(5664):1647-9.
44. A. Fert et al., “Left-Right Asymmetry in the Scattering of Electrons by Magnetic Impurities, and a Hall Effect”, Phys. Rev. Lett. 28, 303 (1972)
45. T. Jungwirth et al., “Anomalous Hall effect in ferromagnetic semiconductors”, Phys Rev Lett. 2002 May 20;88(20):207208.
46. N. P. ONG et al., “Geometry and the Anomalous Hall Effect in Ferromagnets”.
47. Xinjie Wang et al., “Fermi-surface calculation of the anomalous Hall conductivity”, Phys. Rev. B 76, 195109 (2007)
48. Zhong Fang et al., “The Anomalous Hall Effect and Magnetic Monopoles in Momentum Space”, *Science* Vol. 302, Issue 5642, pp. 92-95 03 Oct 2003.

Chapter 2

Experiment

2.1 Abstract

In this chapter, experimental apparatus used in this research will be introduced. In my study, the magnetic thin films are deposited by a home-made magnetron sputtering system which can hold 10 sputtering targets inside the chamber. The thickness of the thin film is calibrated by the Rutherford backscattering(RBS) technique. The magnetic property including the hysteresis curve is measured by the vibrating sample magnetometer(VSM). The spin polarization is measured in liquid helium temperature by a home-made point contact Andreev reflection spectroscopy(ARS) system. A home-made magnetic transport system with a rotating magnet and a probe station is used to measure the magnetoresistance, Hall resistance and other transport measurements.

2.2 Magnetron sputtering

In our lab we use magnetron sputtering to grow thin films. The sputtering process takes place in discharged(plasma) gas environment. Usually the ultrapure Ar gas is used to produce the plasma state. Before the Ar gas is let into the chamber, the chamber must be pumped to reach a base pressure of less than 1×10^{-7} torr. This is because poor vacuum would harm the purity of

the Ar gas so that the Ar is mixed with the O_2 and other compositions in air and sputtered onto the sample. The sample fabricated would be contaminated by the air in the chamber which would degrade the purity and composition of the sample. In our lab, the vacuum can go to 1×10^{-8} torr with the cryopump in action.

Figure 2.1: The sputtering system in our lab.

To achieve high vacuum in our chamber, we use two types of vacuum pumps: turbo pump and cryopump.

The turbo pump is used to achieve rough vacuum before the high vacuum cryopump takes into action or when loadlock is used to send samples into the chamber. This is because the high vacuum cryopump is a very delicate machine which cannot expose to atmospheric pressure. Typically, the turbo pump first pump the chamber from atmosphere pressure to about 10^{-5} torr before the cryopump runs[3].

The cryopump is used to pump the chamber into high vacuum of about $2*10^{-8}$ torr. The mechanism of cryopump is that gas molecules of different kinds can condense on cold surface[3].

During the sputtering process, a high voltage between the sputtering target and the ground is created so the target has a high negative voltage of around 300V. The sample substrate to be sputtered is place just above the sputtering target. Because the high negative voltage around the sputtering target, the pure Ar gas around the target is ionized to form plasma. The process can be given by the following equation[1]:

$$Ar + e^- = Ar^+ + 2e^- \tag{2.1}$$

In the plasma state the Ar is ionized to create a mixer of Ar atoms and positively charged Ar^+ ions and electrons. This state is in dynamic equilibrium which means that the above reaction takes place in both direction at the same time. Some energy is released as UV and visible light

radiation so that one can see purple colour glowing gas when the plasma is formed. Because the target is negatively charged, the positive Ar^+ ions will be accelerated by the electric field created by the target and will bombard onto the atoms of the target surface. When the energy of the Ar^+ ions knocking on the target is within appropriate range, the sputtering process will take place in which the atoms on the target are knocked off and evaporated on the the substrate.

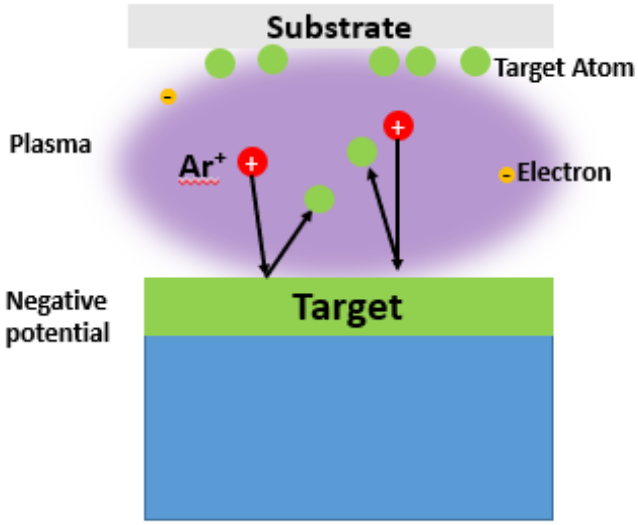

Figure 2.2: Schematic diagram for sputtering process.

During the sputtering process, the pressure to the Ar air plays a crucial role in the final sputtering yield. In the magnetron sputtering, the preferred Ar pressure is a few mtorr. In our lab, the Ar pressure is fixed at 6 mtorr during sputtering. Too high and too low pressure will both result in lower sputtering yield. If the pressure is too low, less Ar^+ will be ionized resulting in

a low deposition rate. In reality, at very low Ar pressure, the plasma state will not even be able to be created at all. If the Ar pressure is too high, the deposition rate will also suffer due to the shorter mean free path and too many scattering in the plasma[1][2].

The sputtering deposition described above has a very low deposition rate. To improve sputtering yield, magnetron sputtering is developed. In magnetron sputtering, strong magnets are placed under the sputtering targets. Ring shaped magnetic fields are created above the targets. Due to the magnetic fields, the electrons in the plasma are confined just above the targets, moving in helical paths along the magnetic field line. The density of electrons above the target is greatly enhanced in this way, resulting in increased chance of ionizing the Ar atoms. The deposition yield is greatly increased in this way[1].

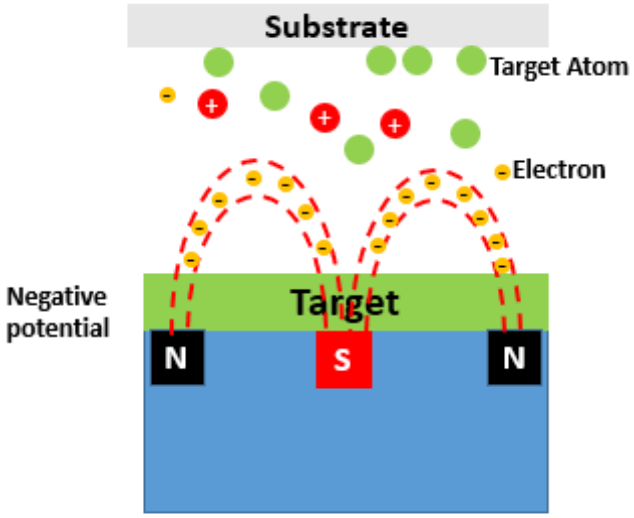

Figure 2.3: Schematic diagram of magnetron sputtering.

Sometimes the sputtering targets are insulators such as MgO and YIG. In these cases, if the target is provided a negative electric potential as described earlier, the positive charge will accumulate onto the target, preventing the Ar^+ from further bombarding on to the target. A solution to this problem is to provide the target with radio frequency(RF) alternating voltage. In the radio frequency sputtering process, during the short time when the target is provided positive voltage, electrons are attracted onto the target, neutralizing the positive charge accumulating on the target, thus preventing the positive charge being accumulated on the surface[1][2].

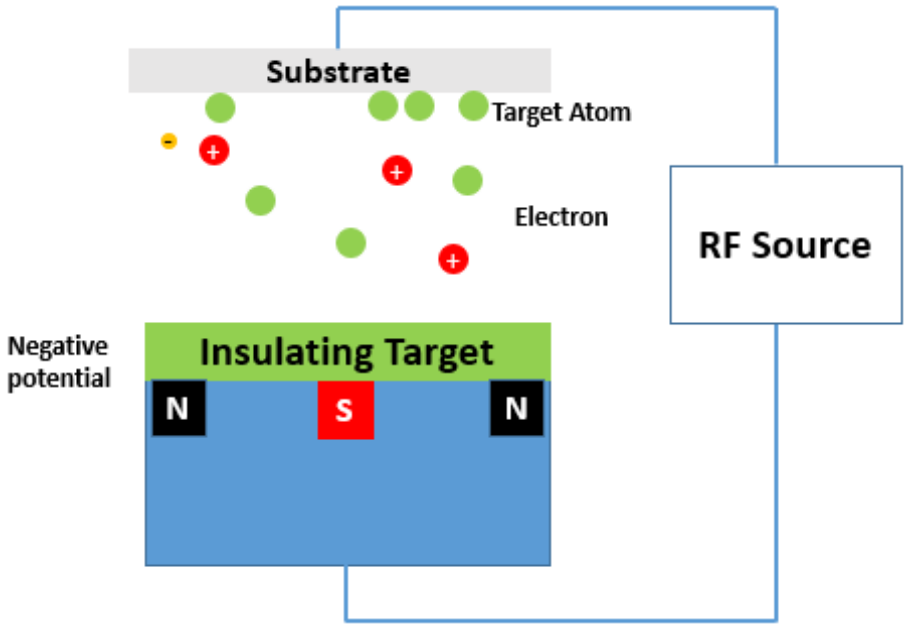

Figure 2.4: Schematic diagram of RF sputtering.

2.3 Rutherford Backscattering

We grow different kinds of thin films on the substrate and we need to know the thickness of the thin films accurately in order to do good research. Rutherford Back Scattering (RBS) is employed in our lab to perform the thickness calibration of our samples.

RBS is an analytical method used in material science to determine the structure and composition of materials by measuring the backscattering of a beam of alpha particles impinging on the sample. Figure 2.5 is an illustration of the RBS process.

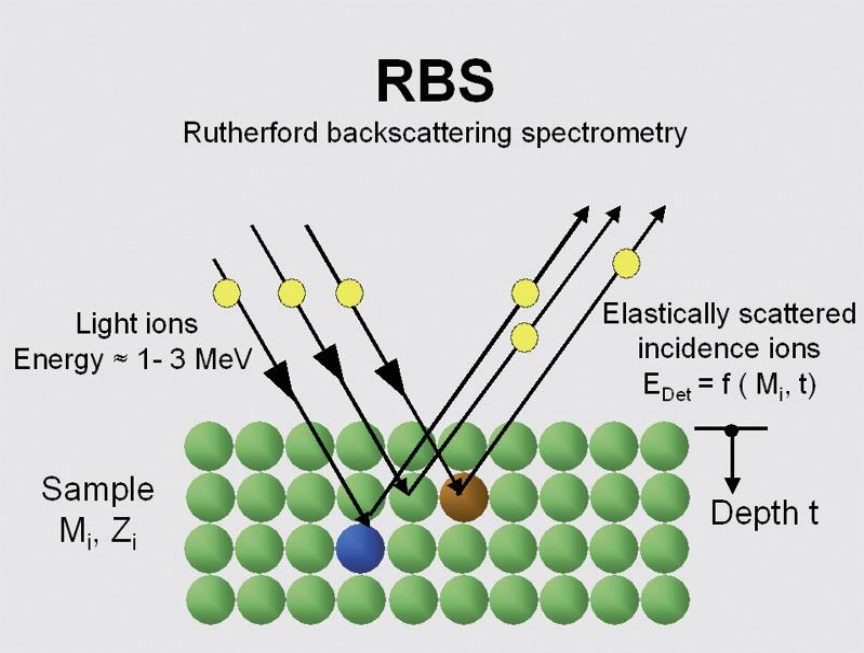

Figure 2.5: Rutherford Backscattering Mechanism[7].

When the alpha particles impinge on a piece of sample, a small portion of the particles will be elastically scattered backward due to the collision with the ion cores of the sample. In RBS, the detector is positioned on the same

side of the incoming particle beam to receive the backscattered alpha particles. The energy of the backscattered alpha particle is:

$$E_1 = kE_0 \tag{2.2}$$

where k is known as the kinematic factor, it can be written as[4][5][6]:

$$k = \left[\frac{m_1 cos\theta_1 \pm \sqrt{m_2^2 - m_1^2 (sin\theta_2)^2}}{m_1 + m_2}\right]^2 \tag{2.3}$$

where the subscript 1 and 2 refer to the alpha particle and the particle on the sample respectively. The probability of observing the backscattered alpha particle is given by the differential cross section of the scattering [4][5][6]:

$$\frac{d\omega}{d\Omega} = \left[\frac{Z_1 Z_2 e^2}{4E_0}\right]^2 \frac{16}{(sin\theta)^4} \tag{2.4}$$

The detector can count the number of alpha particles backscattered with different energy. The thickness of the sample can be interpreted by analyzing the particle yield vs energy spectrum.

RBS spectra of Cu and Pt sputtered in our chamber is shown in figure 2.6 and figure 2.7. The peak in the spectra is the characteristic of the material in the sample. The thickness of the thin film can be calculated by fitting the spectra with the RBS analysis software XRUMP, as can be seen in figure 10 and figure 11, the black solid lines represent the number of detected particles vs energy spectra, the red solid line represents the XRUMP fitting. For figure 5, the narrow peak at 275 meV is Cu thin film, the long tailing off represents

the thick SiO2 substrate, the deposition time for this sample is 240 s and the thickness of the Cu film is fitted as 194.3 Å[4][5][6].

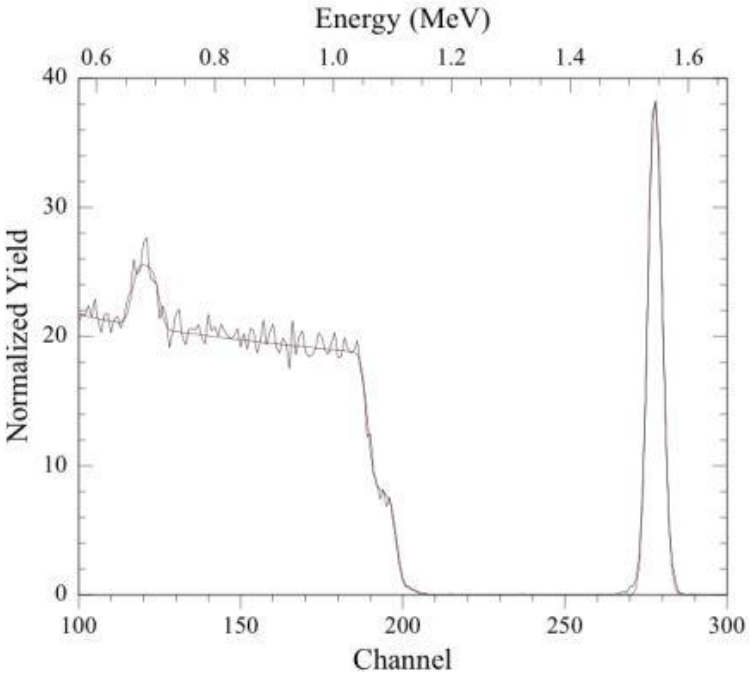

Figure 2.6: RBS curve fitting for Cu thin film in our lab.

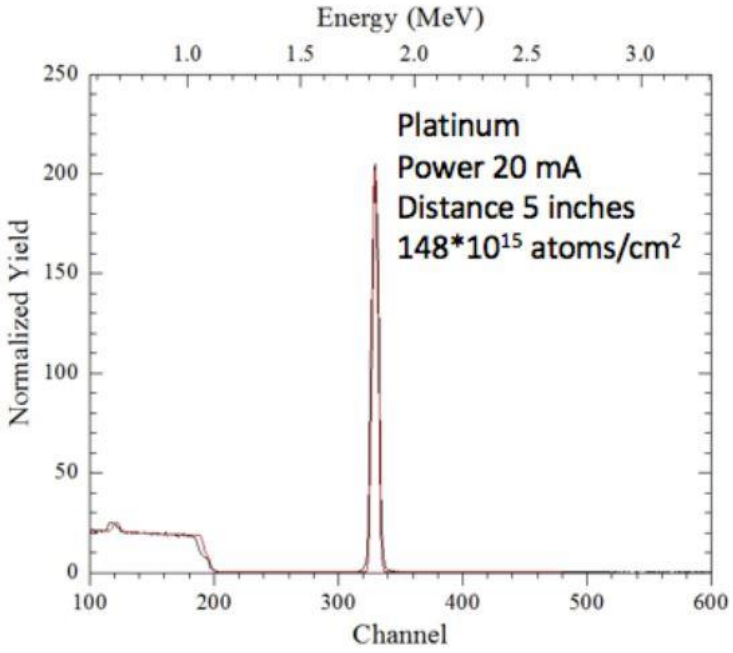

Figure 2.7: RBS curve fitting for the Pt thin film in our lab.

The thickness of the film can be calculated by the following equation:

$$T(\mathring{A}) = N(\frac{1}{cm^2}) \times \frac{1}{n_0} \times V(cm^3) \times \frac{1(\mathring{A})}{10^{-8}(cm)} \tag{2.5}$$

2.4 Vibrating Sample Magnetometer

The Vibrating Sample Magnetometer(VSM) was invented in MIT Lincoln Lab by Simon Foner in the mid of 20th century[8]. VSM can accurately measure the magnetization of a sample under external magnetic fields. It functions in room temperature and is easy to setup. The mechanism of VSM is Faraday's law of magnetic induction.

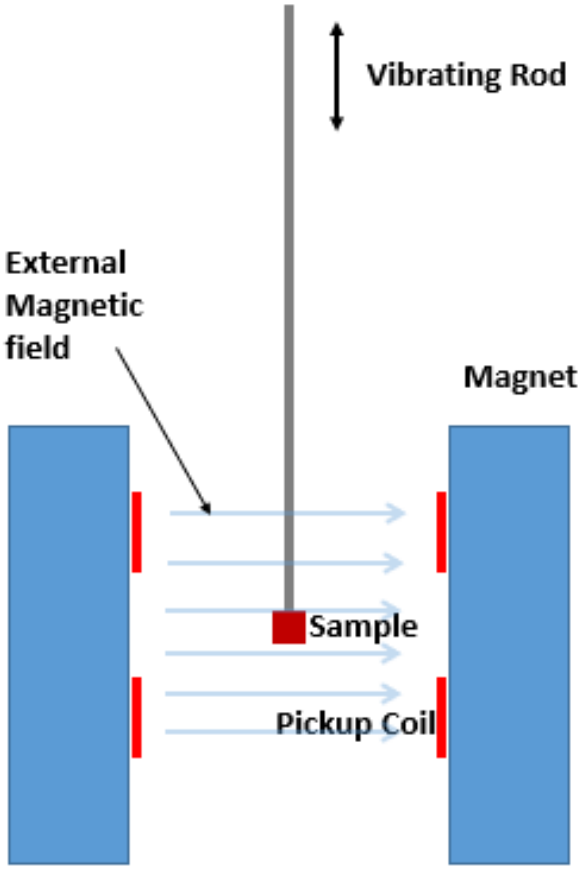

Figure 2.8: Schematic diagram of VSM.

As can be seen from the diagram, the uniform external magnetic field is provided by an electromagnet. The field can sweep slowly so that a field dependent magnetization curve can be obtained. This curve shows hysteresis loop property for ferromagnetic materials. A Hall probe is mounted near the uniform field region to measure the external magnetic field. The external magnetic field should not be confused with the small vibrating magnetic field generated by the magnetization of the sample. In the measuring process, the sample vibrates vertically perpendicular to the external magnetic field with a small amplitude in high frequency. Four pickup coils are mounted around the

sample the receive the signal. The sample is magnetized by the external field and is vibrating at frequency f, the magnetic field due to the sample can be written as:

$$B = Ce^{i\frac{ft}{2\pi}M} \tag{2.6}$$

C is constant and we can see that the magnetic field caused by the magnetization of the sample also vibrates sinusoidally. According to Faraday's law, this changing magnetic field will induce a voltage in the pickup coil which is given by[8]:

$$V \propto \frac{dB}{dt} = \frac{Cf}{2\pi} e^{i\frac{ft}{2\pi}M} \tag{2.7}$$

We can see that this voltage signal vibrates in the same frequency as the vibrating rod and is sent to a lock-in amplifier for signal processing. The lock-in amplifier can measure small signal with certain frequency accurately, in this case, the lock-in is tuned to measure all signals in the vibrating frequency of the sample so that the magnetic field produced by the sample magnetization can be accurately measured. This signal is compared by a signal generated by a reference sample so that the accurate magnetization of the sample can be retrieved. In our lab, a Ni sphere is used as the reference sample. We can see that the pickup coil is not sensitive to the external magnetic field but only can measure the vibrating magnetic field generated by the sample. Also, radio frequency electromagnetic field exists in our daily lives such as the 50Hz frequency of the AC electricity. To avoid the

contamination from these signals, the frequency of the vibrating rod is tuned such that to avoid these common values[8].

The VSM instrument in our lab is bought from Lakeshore company, the model is Lakeshore 7304. The measurement moment from the sample can be as small as 5×10^{-6}emu under external magnetic field as high as 14.5kG. The adjustment air gap between the magnet meets the sample and magnetic field strength requirements. The Noise level is 5×10^{-6}emu at 0.9" gap and 50×10^{-6}emu at 1.6" gap[9].

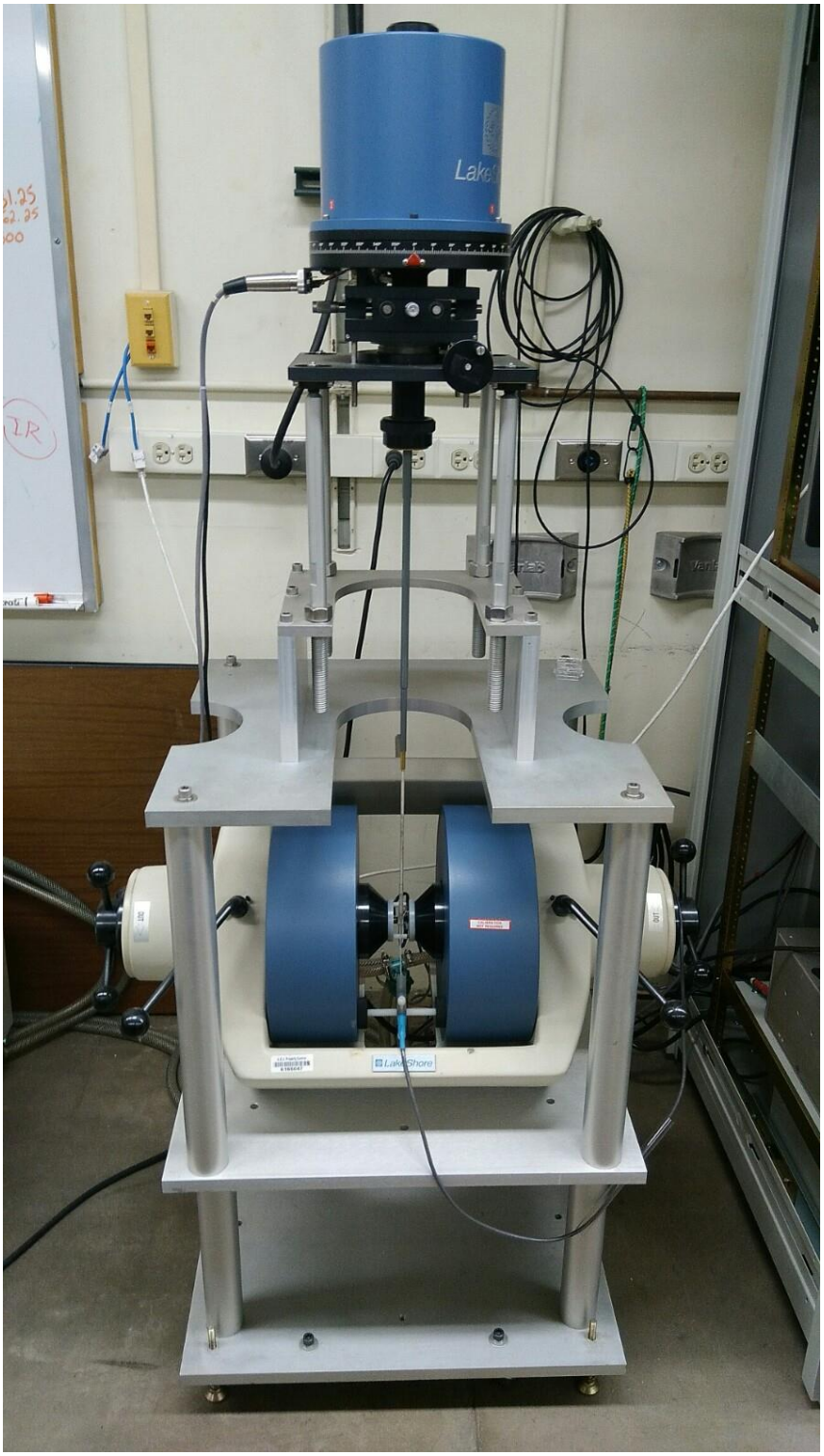

Figure 2.9: Photo of the Lakeshore 7304 VSM in our lab.

2.5 Magnetic Transport system

In our lab, we use the home built magnetic transport system as one way to measure the magnetoresistance and the Hall signal of the thin film samples.

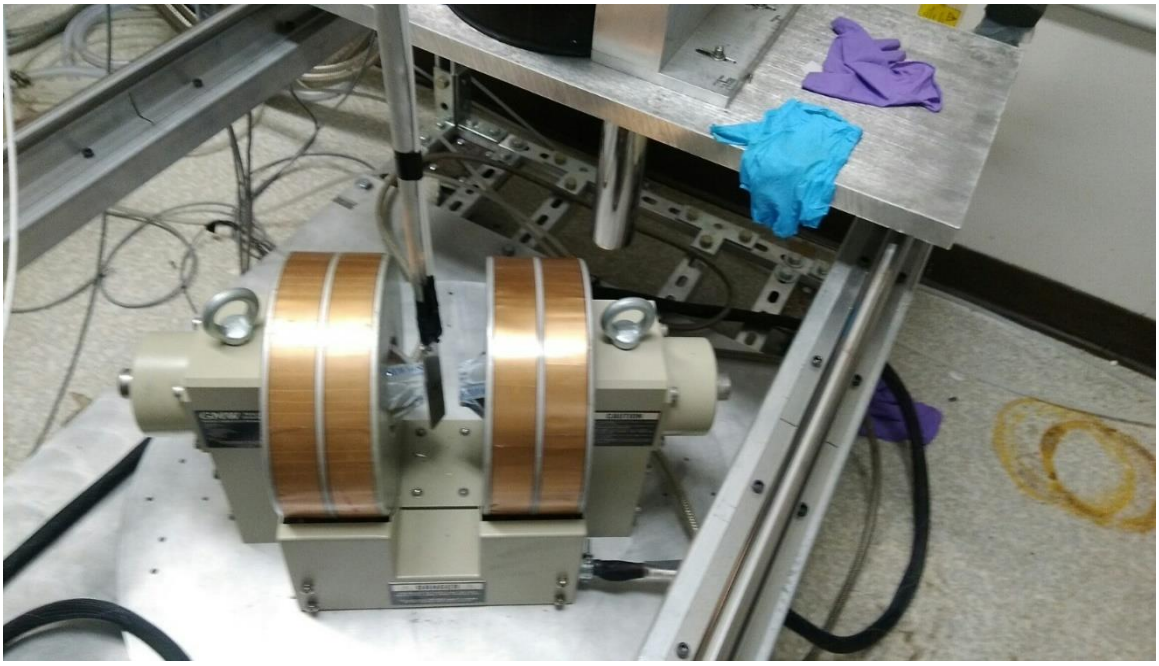

Figure 2.10: Picture for the magnetic transport system in our lab.

The magnetic transport system in our lab is essentially the four point contact measuring technique combined with a electromagnet. During the measurement, the sample is placed between the air gap of the magnet to ensure uniform magnetic field applied to the sample. The gap of the electromagnet is adjustable to meet different magnetic field strength requirements. The magnet can also be rotated so that the magnetic field angular dependence of the physical property can be measured.

The four point contact method is used in the magnetic transport system to measure the magnetoresistance and Hall effect because the two point contact

measurement is not as accurate as the four point contact measurement. Also, the two point contact method can only measure resistance while the four point contact measurement can measure Hall signal[10][11].

In the two point contact measurement, the resistance of the sample is obtained by measuring the voltage across the sample and the current that flows through the sample and taking division R=V/I. However the resistance of the wire is not negligible in experiments that require high accuracy and this will result in error of the ammeter reading and thus the resistance calculation.

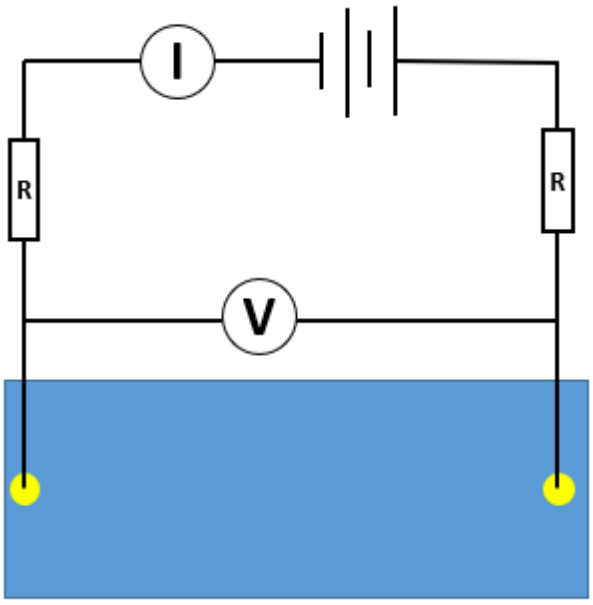

Figure 2.11: Illustration of the two-point contact method for resistance measurement.

To address the problem of the wire resistance, four-point contact method was introduced by Kelvin[11]. In this regime, one uses two different circuit for current sending and voltage measurement and they are independent with

one another. The current is sent in through two electrodes by a current source, thus ensuring that the current passing through the sample is exactly the same as the reading shows on the current source. The voltage is measured by voltmeter through another two electrodes. Because the inner resistance of the voltmeter is generally much larger than the resistance of the sample to be measured. The current passing through the voltmeter is negligible compared with the current passing through the sample. The reading on the voltmeter is almost the real voltage drop on the sample. Both the current and voltage reading are true value in the four-point contact method so that the resistance of the sample can be calculated by R=V/I. Also, the addition of another two electrodes enables the Hall signal measurement to be conducted.[10][11].

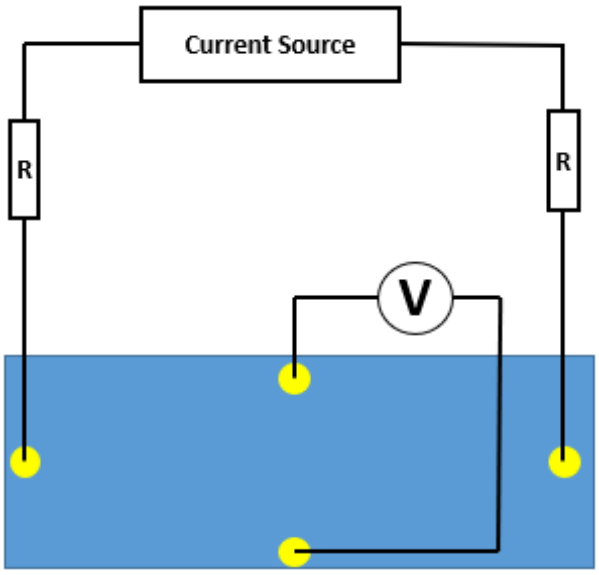

Figure 2.12: Illustration of the four-point contact method.

2.6 Probe Station

Another equipment in our lab which we use to do electrical transport measurement is the probe station. The probe station uses manipulators instead of wires to make physical contact with the sample. The manipulators are thin needle tips thus can make precise contact on the sample. It is convenient to use and can make fast contact with the sample. In the probe station, the magnetoresistance, I-V curve and Hall signal can be measured. The measurement is controlled by the Labview software.

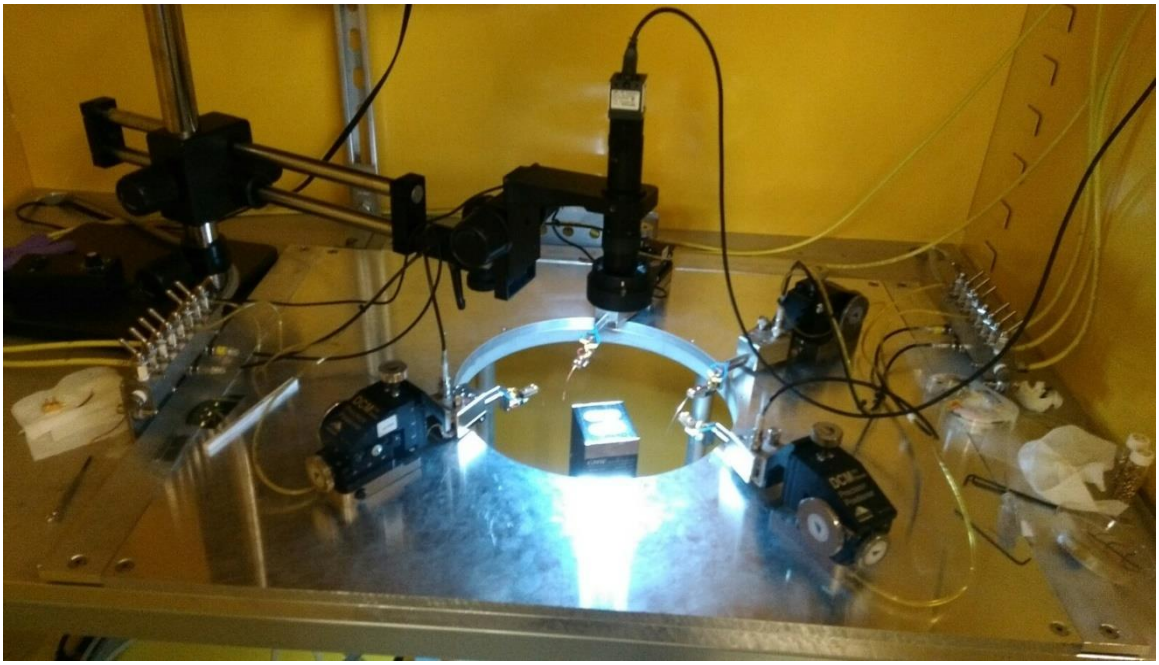

Figure 2.13: Photo of the probe station in our lab.

2.7 Andreev Reflection Spectroscopy Measurement

In this lab, we use the point contact method to measure the Andreev Reflection Spectroscopy(ARS). Because the ARS involves in the interaction between a superconductor and normal metal, low temperature must be achieved in order for the material to reach superconducting state. In my experiments, the superconductors are made into sharp tips to be contact with the materials to be measured so that the spin polarization of that material can be analyzed. The super conducting tips in my measurement are Pb and Fe-superconductor. They typically work well in Liquid He temperature of about 4.2K. During the measurement, liquid He is used to achieve the superconducting state. The entire experiment takes place inside a big tank which contains a 50 Liter liquid He reservoir. The liquid He has extreme low temperature of 4.2K and evaporates instantaneously when exposed to room temperature. In fact, Liquid He can explode when it is enclosed in a compartment and exposed to room temperature, this is very dangerous and several accidents have happened related to this. To prevent situation from happening and also save the liquid Helium, the liquid He reservoir is surrounded by three other layers of jacket structures. Immediate outside the Liquid He tank is a vacuum jacket, this jacket is pumped to high vacuum by a turbo pump. This vacuum layer will provide the first level of protection to the Liquid He from outside environment. Another layer next to the vacuum layer is a liquid N_2 tank. Liquid N_2 is pumped into this tank to further

insulate the inner core liquid He from contacting the room temperature. The most outside layer is another vacuum chamber. This chamber is also pumped to high vacuum by a turbo pump before the experiment to offer the last layer of protection to the liquid helium at the center. Because the liquid N_2 is only protected by the outmost vacuum chamber from the room temperature environment, it evaporates slowly during the experiment. The liquid N_2 chamber has to be refilled every 8 hours during the experiment.

The sample tube is immersed in the liquid He chamber. The vacuum jacket that contains the sample is inserted into the sample tube. The sample tube and the liquid He chamber is connected by an ultrafine needle valve. During the experiment, the needle valve is opened and the liquid He is let into the sample tube so that the sample can be cooled down. The sample tube is also connected to an oil pump through a pumping port so that sub liquid He temperature can be obtained by pumping the liquid He. The best low temperature obtained in this system is below 1.5K. The sample to be measured and the superconducting tip is mounted on the sample holder and the tip is made into contact with the sample through a differential screw. The screw can control the tip move into or away from the sample surface, multiple contacts can be made during the experiment. The tip only moves in a few μm with one turn in the differential screw so that the point contact between tip and the sample can be made. The contact size, Z tunneling factor and the contact resistance are all different with different contact. The contact must be

in the ballistic region for the ARS to take into action. The electrical setup of the measurement is also the four-point contact configuration. The current is sent in by a Keithley current source and the voltage is measured by a highly sensitive voltmeter. The differential conductance dI/dV is measured during the experiment. A lock-in amplifier is used to send in a high frequency weak signal to the connection to tell if the point contact is made and the contact resistance.

The sample holder is inserted into a small diameter vacuum tube which is further inserted into the sample tube during the experiment. The small diameter vacuum tube is pumped into high vacuum of 10^{-6} torr and then filled with high purity He gas before inserted into the sample tube. The vacuum tube must be filled with high purity He gas because generally sub liquid He temperature is maintained during the experiment and other gas component inside the tube will freeze which will damage the sample and the equipment.

Figure 2.14: Photo of the point contact ARS equipment.

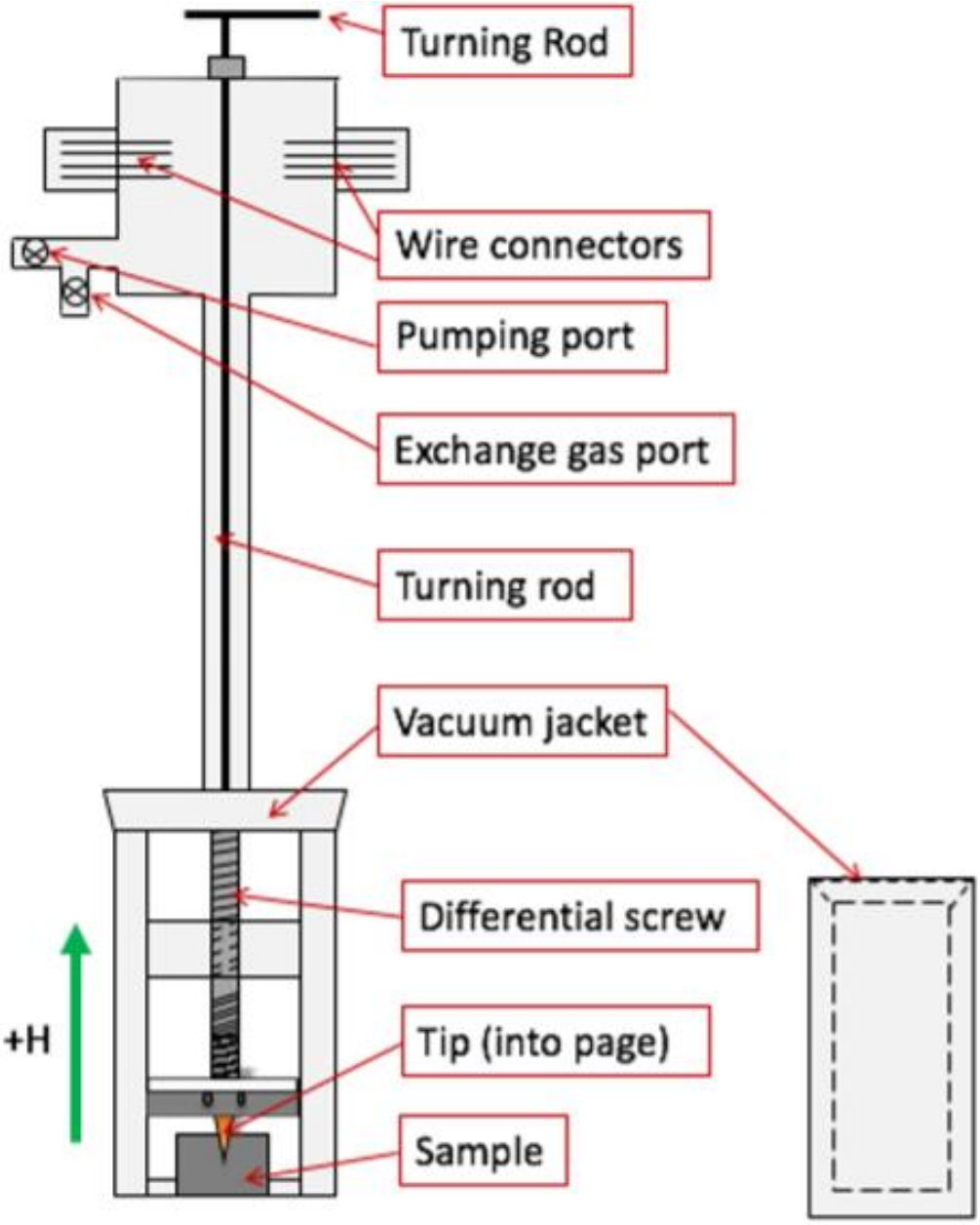

Figure 2.15: Schematic of the point contact measurement[12].

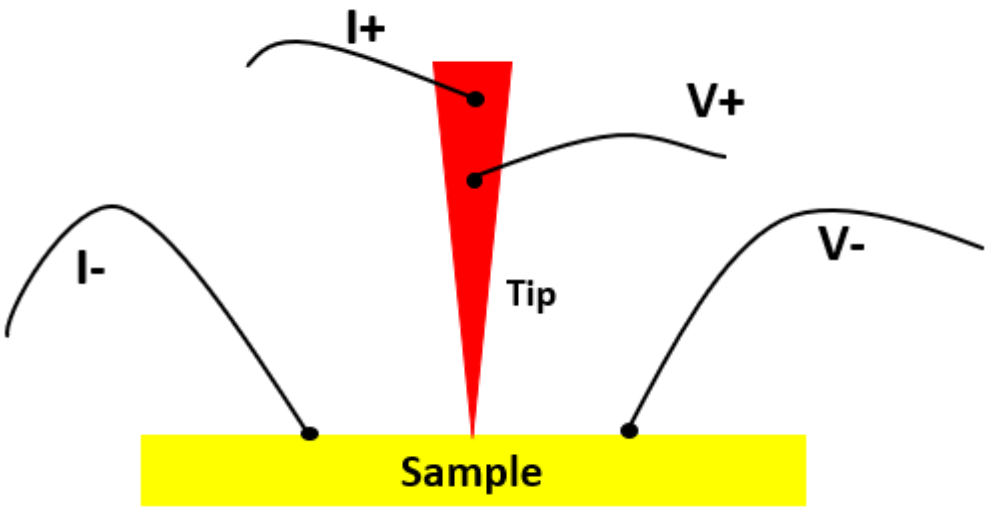

Figure 2.16: Four-point measurement in ARS point contact configuration.

REFERENCE

1. D. L. Smith, “Thin film deposition”, McGraw-Hill, Inc., New York (1995)
2. Donald M. Mattox, “Handbook of Physical Vapor Deposition (PVD) Processing”, William Andrew, (2010)
3. John F. O’Hanlon, “A User’s Guide to vacuum technology”, John Wiley & Sons, New York, (2003)
4. Oura, K. Lifshits, et al., “Surface Science: An Introduction.” Springer-Verlag. ISBN 3-540-00545-5 (2003).
5. Feldman, L.C, et al., “Materials Analysis by Ion Channeling.” Academic Press (1982).
6. Feldman, L.C. et al., “Fundamentals of Surface and Thin Film Analysis.” Prentice-Hall (1986).

7. Sarvesh Kumar et al., “Preparation of Gold Target through Electron Vapor Deposition and " Paras " the Rutherford Back Scattering Experimental setup.” Conference: NCIL 2015, Volume: 1
8. S. Foner, “Versatile and Sensitive Vibrating-Sample Magnetometer” Rev. Sci. Instrum. 30, 548 (1959).
9. “Lakeshore Model 7304 Vibrating Sample Magnetometer” Manual.
10. Chandra, H., et al. Open-Source Automated Mapping Four-Point Probe. Materials 2017, 10(2), 110.
11. Heaney, Michael B. “Electrical Conductivity and Resistivity.” Electrical Measurements, Signal Processing, and Displays. Ed. John G Webster. CRC Press, 2003. 7-1.
12. Gifford A. Jessica, “Andreev Reflection Spectroscopy: Theory and Experiment.”

Chapter 3

Tuning Anomalous Hall Effect in MgO/Permalloy/Heavy Metal Based Trilayer Structures

3.1 Abstract

Anomalous Hall effect(AHE) is a good characterizing technique to illustrate magnetic property in spintronics research. In this chapter, the anomalous Hall resistivity is conducted on the MgO/Py/Heavy metal(HM) based trilayer structures using the magnetic transport system. Sign change (negative to positive) in Hall resistivity is observed when Ta, Hf, Ru, Pt, Cu is used as the HM capping layer while increasing capping layer thickness. AHE signal attenuation with no sign change is observed in W capped trilayer structures. No sign change is observed when light metal Al is used as the capping layer. The MgO base layer is crucial for the sign change in AHE in Ta capped trilayer structure. The thickness of the Py interlayer does not affect the sign of the Hall resistivity. No sign change is observed when Py interlayer is replaced by CoFeB. The spin orbit coupling induced Berry curvature plays a crucial role in the sign of the anomalous Hall effect in magnetic structures. The surface and interface scattering might also be important in the sign of the AHE in magnetic thin film structures.

3.2 Introduction

The Anomalous Hall Effect was discovered by Edwin Hall in 1881, not long after he discovered the Ordinary Hall Effect. He observed that The Hall signal in ferromagnetic materials were 10 times larger than that in nonmagnetic metals. In Hall effect, if there is a charged current passing through the sample and a magnetic field applied perpendicular to the sample surface, there would be measurable voltage across the sample, perpendicular to the current direction. This transverse voltage is called Hall voltage and is found to be related to the external applied magnetic field and the magnetization of the sample (if the sample is a magnetic material). The equation of the Hall resistivity can be written as[1]:

$$\rho_H = R_0 H + 4\pi R_s M \tag{3.1}$$

Where the first term to the right of equal sigh is the Ordinal Hall effect contribution and the second term is due to the Anomalous Hall Effect which is proportional to the magnetization of the sample. In Ferromagnetic materials, the second term is much larger than the first term and the response of the magnetization to the external magnetic field shows hysteresis curve. Therefore, the response of the anomalous resistivity to the external magnetic field shows hysteresis loop. Unlike the Ordinary Hall effect which is due to the Lorentz fore deflection of the charge carriers, the mechanism of the Anomalous Hall effect is much more complicated and is still controversial in

some aspect up to now. The anomalous Hall effect is closely related to the quantum physics and cannot be explained by classical physics. There are mainly three mechanisms that cause the Anomalous Hall effect: The intrinsic mechanism which now is commonly believed to originate from Berry curvature in momentum space, skew scattering and side jumps. The other two is the extrinsic mechanism due to the spin dependent impurity and disorder scattering of charge carriers in the materials[1].

The intrinsic mechanism of anomalous Hall conductivity comes from the Berry curvature in momentum space of the crystal which is nonzero due to the broken time reversal symmetry by spin orbit coupling. As is already derived in chapter 1, the Berry curvature of a given crystal can be written as[25]:

$$\sigma_{xy} = \frac{e^2}{\hbar}\int \frac{d^3k}{(2\pi)^3}\sum_n f_{nk}\Omega_n^z(\boldsymbol{k}) \tag{3.2}$$

Where H is the Hamiltonian of the perfect periodic lattice. The intrinsic contribution is proportional to the integration over all Fermi sea of occupied band Berry curvature[1]. The intrinsic mechanism can be theoretically studied by doing band structure calculations and prominent in materials with strong spin orbit coupled band[1].

Besides the intrinsic mechanism which is the Berry curvature in momentum space, extrinsic mechanisms such as skew scattering and side jumps also contribute to the anomalous Hall effect in magnetic materials. These effects are due to the asymmetric scattering of electrons by ions or

impurities in the crystal and also contribute to anomalous Hall effect. In magnetic thin film structures, the surface and interfacial scattering is particularly important in the anomalous Hall effect.

The correlation between the Anomalous resistivity and the longitudinal resistivity is call the scaling law. By analyzing the scaling law, the contribution due to different mechanisms can be separated. The scaling law is described by:

$$\rho_s \propto \rho_{xx}^{\gamma} \tag{3.3}$$

Where the γ reveals the dominating mechanisms that contributes to AHE. The intrinsic contribution gives a scaling factor $\gamma \approx 2$. Skew scattering contribution to anomalous Hall resistivity gives a scaling factor $\gamma \approx 1$. Side jump contribution to anomalous Hall resistivity gives a scaling factor of $\gamma \approx 2$. For many materials, the scaling factor γ deviates far from the value of 2 indicating that scattering or other unexplained mechanism makes pronounced contribution to the measured anomalous Hall resistivity[1][2][3].

In recent years a sign change in anomalous Hall effect have been observed in some magnetic systems. A temperature dependence sign change in anomalous Hall effect was observed in Fe/Gd bilayers by Xu et al. Sign change is due to the different spin polarization and Curie temperatures of the Fe and Gd layers[26]. It was also found that by doping the CuCrSe spinel by diamagnetic Br element, a sign change was also observed and corroborated by Berry curvature calculation[25].

In the studies of Co/Pd bilayer or multilayers which exhibit a perpendicular magnetic anisotropy. In Co/Pd multilayers, scaling factor of $\gamma \approx 5.7$ has been observed which deviates from a value of 2. Surface and interface scattering between the Co layer and the Pd layer is proposed to play an important role in the measured AHE. There is also a change of polarity of polarity of the AHE signal when the number of repetition of the multilayer increased from 6 to 80. For multilayers with very few repetitions, the surface scattering makes important contribution to the AHE while for multilayers with high number of repetitions, the contribution from surface scattering is negligible. The sign of surface scattering AHE is opposite to the interface scattering AHE and bulk contribution. Also, in Co/Pd and Co/Pt multilayers the sign of the skew scattering related AHE is opposite to the AHE from side jump[2][11][12]. Another possible theoretical explanation for the polarity change in the AHE in Co/Pd multilayers is that the change in the position of 3d band in Co/Pd from lower half of the band to upper half of the band depending on the Pd thickness[5]. A polarity change in AHE is also observed in Co/Pt multilayers with an insertion of a thin FeMn antiferromagnetic layer[8]. The change of polarity in the structure has nothing to do with the exchange bias effect induced by the FeMn. It is argued that the FeMn layer exhibits a very short spin diffusion length of ~1.5nm, this changed the relaxation times of the majority and minority electrons in the Co/Pt layers and thus change the relative contributions of the spin carriers to the AHE.

This is the reason of the polarity change in Co/Pt systems with FeMn insertion[8]. It is also studied that the AHE in Co/Pt multilayers can be greatly enhanced by MgO or Ru sandwich layers. This is proposed to due to scattering effect at the MgO/Pt or Ru/MgO interface[9][10]. AHE is also studied in single layer graphene/YIG thin film structure. It was argued that the proximity induced ferromagnetic order in the graphene by the YIG film is responsible for the AHE signal and the contribution is mostly from extrinsic mechanism[14]. MgO/CoFeB/HM structure has been extensively studied based on its strong perpendicular magnetic anisotropy and applications to manufacture magnetic tunnel junction with high tunneling magnetoresistance ratio(TMR). According to studies, there are several contributions to this. Due to the spin orbit coupling, the 3d orbitals of the Fe and Co lift out of plane and also there is a hybridization of the dxz, dyz and dz^2 of the 3d orbitals. Also, there is a hybridization of the O 2p orbitals and Fe 3d orbitals due to formed Fe-O bonds[17-24]. These hybridizations modify the band structure and creates a strong out of plane crystal field.

In this chapter, MgO/Permalloy/HM structure is studied. The Permalloy(Py) is mostly a Ni/Fe alloy which consists of Ni/Fe/Mo/Mn. The ratio is 79%/16.7%/4%/0.3%. In this study, I will use AHE as a tool to study the magnetic property of the structure and we can see that the polarity of the AHE signal in this structure can be tuned by the HM capping layers.

3.3 Sign Switching of Anomalous Hall Effect in MgO/Py/Ta structures

3.3.1 Tuning the sign of Anomalous Hall Effect

In this section, I will show the AHE measurement in MgO/Py/Ta structures. The structure is deposited by magnetron sputtering on thermally oxidized Si substrate. The entire structure is thus: Si/SiO_2/MgO/Py/Ta, Ta is used as the capping layer for the entire structure also can induce the AHE polarity change.

The first data is MgO(2nm)/Py(1.6nm)/Ta(0-4nm), the MgO and Py thickness is fixed and the Ta layer thickness increased from 0-4nm. AHE is measured for each sample.

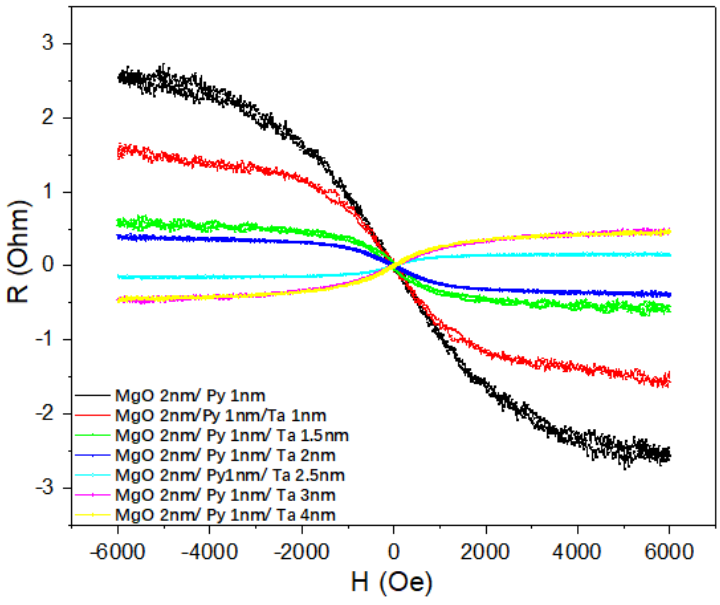

Figure 3.1: AHE for MgO(2nm)/Py(1.6nm)/Ta(0-4nm)

From the above figure, we can see that the polarity of the Hall signal gradually changed from negative to positive when the Ta thickness increases. The saturated Hall resistance gradually increased, changes sigh when Ta is about 2nm saturated when Ta thickness is beyond 4nm. The AHE curve beyond 2000 Oersted is saturated and the relationship between Hall resistance and magnetic field is linear in this region. In this region the magnetization is saturated so only ordinary Hall effect plays a role therefore it is not horizontal but also shows some slope. We can see that the slope in the saturated region also changes from negative to positive as Ta thickness increases.

The next structure is the Si/SiO2/Ta(3nm)/MgO(2nm)/Py(1.6nm)/Ta(0-4nm). I added another 4nm of Ta beneath the MgO layer. The data is as follows.

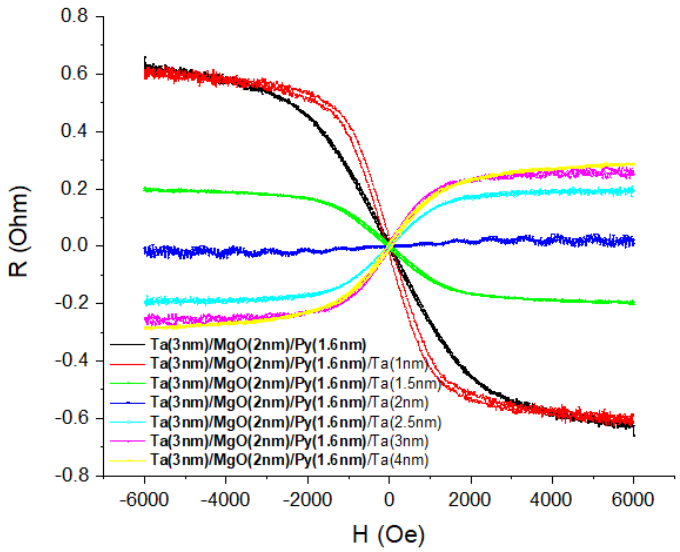

Figure 3.2: AHE for Ta(3nm)/MgO(2nm)/Py(1.6nm)/Ta(0-4nm)

As can be seen from the graph, putting another 3nm of Ta beneath the MgO 2nm layer does not change the property of the samples. There is also a polarity change as Ta thickness increases. One can see that when the Ta thickness is about 2nm, the Hall curve is almost parallel to the x axis, demonstrating the transition occurs at this point. One can also see that the linear part which corresponds to the Ordinary Hall effect also changes sign which might indicates the charge carrier type change in the structure.

I also measured the angular dependence of the AHE for the structure Si/SiO2/Ta(3nm)/MgO(2nm)/Py(1.6nm)/Ta(4nm).

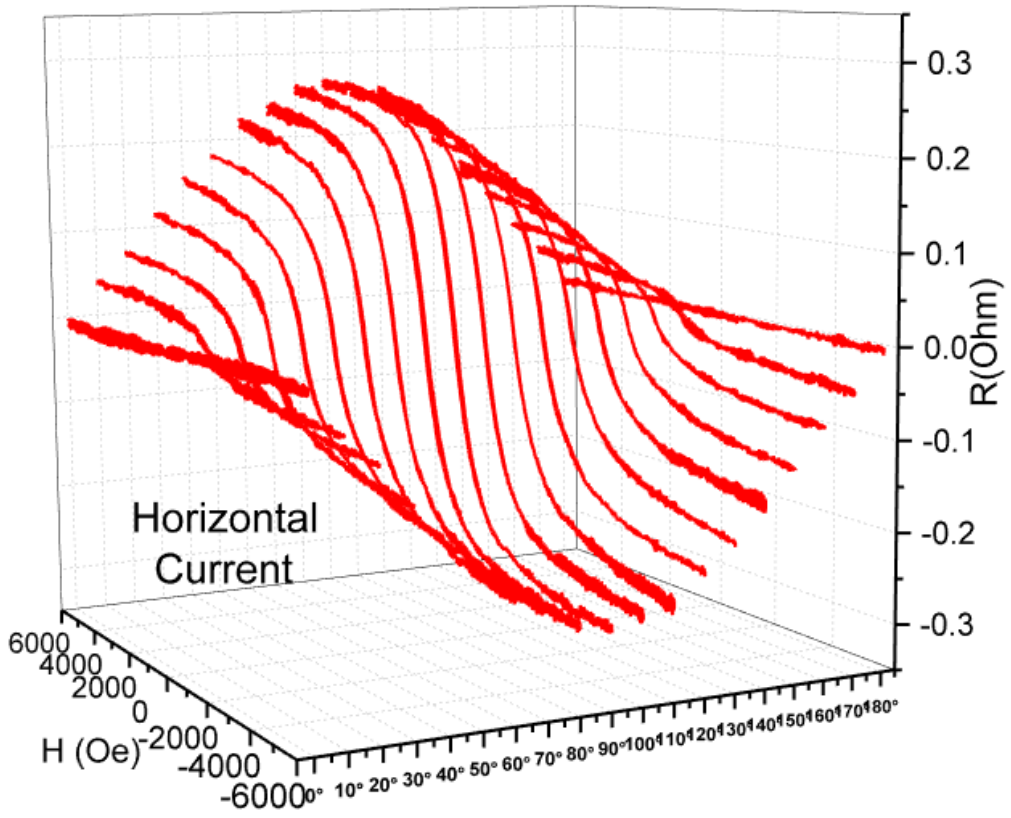

Figure 3.3: Angular dependence of AHE when current is applied horizontally. The sample face front, 90° means field is out of sample plane.

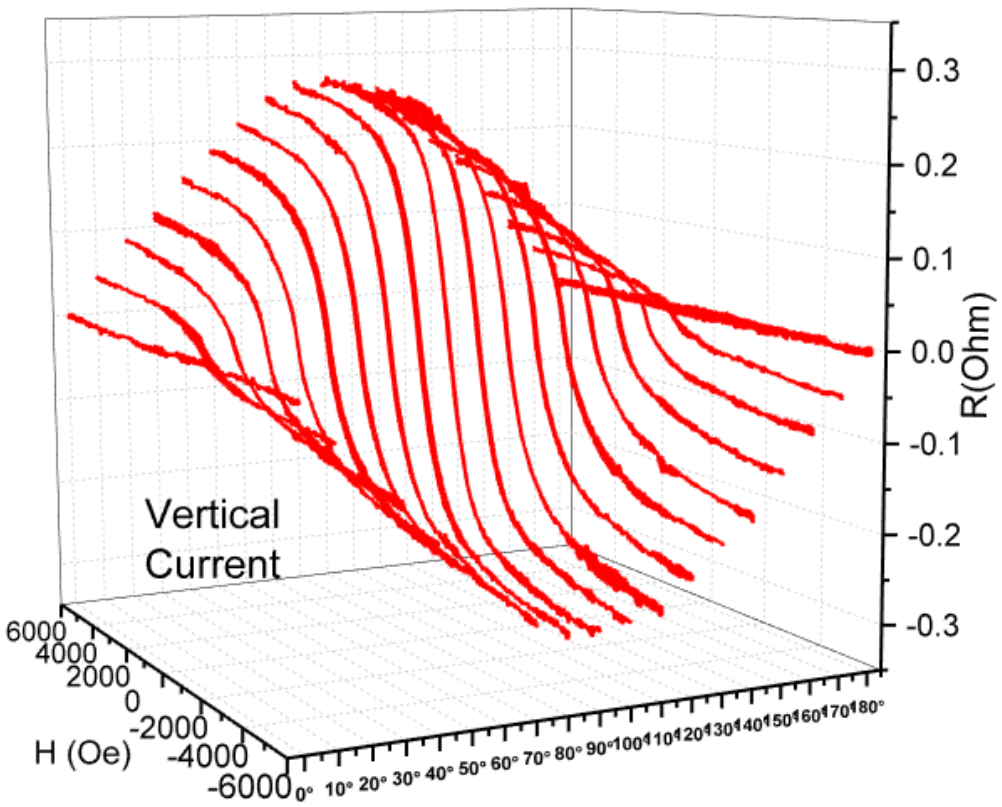

Figure 3.4: Angular dependence of AHE when current is applied vertically. The sample face front, 0° means field is out of sample plane.

The above is the angular dependence of the AHE curve for current applied horizontally and vertically respectively. Please note that the external magnetic field is applied horizontally and the surface of the sample faces front which means that when the angle is 90°, the magnetic field is applied out of the plane and the signal measured is the AHE. When angle is 0° the magnetic field is applied in plane.

From the above angular dependent measurements, we can see that the when angle is 90°, the AHE signal is maximum and the shape follows good hysteresis shape which corresponds the magnetic property of the material.

When the angle is 0°, the signal is minimized and is almost zero parallel to the x axis.

3.3.2 Effect of Py/Ta bilayer, not due to oxidation

To find out about the reason of the polarity change in the structures, I removed the MgO layer so the structure now is Si/SiO2/Py(1.6nm)/Ta(0-8nm).

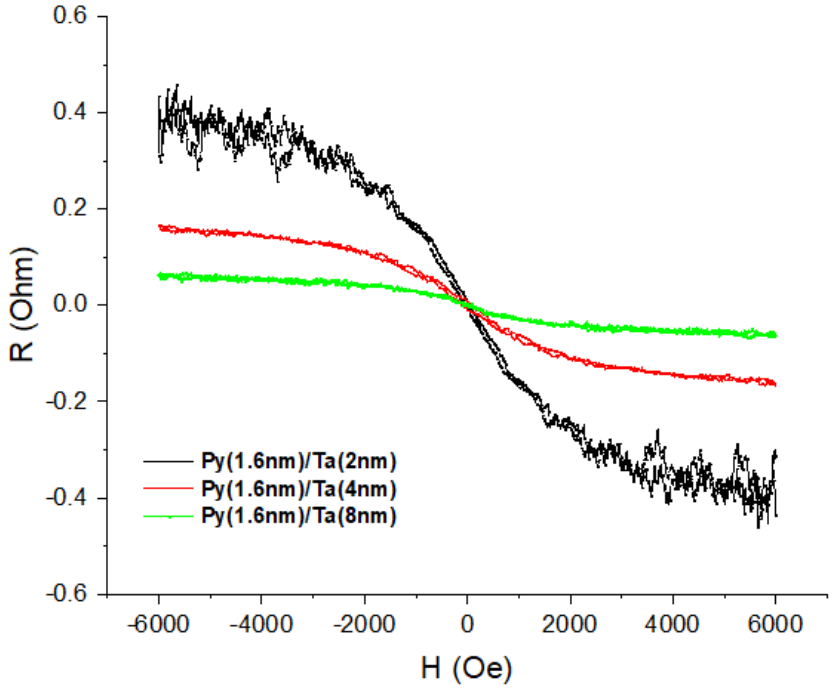

Figure 3.5: AHE for Py(1.6nm)/Ta(0-8nm) structures.

From the data, we can see that without MgO layer beneath the Py layer, the polarity change in the AHE is not observed even if the Ta thickness is increased to 8nm. The magnitude of the AHE simple decreases with increasing Ta thickness which is as expected because magnetic property of Py is diluted by the Ta layer. From this result, we can see that the sign change in AHE cannot simply be explained by the carrier charge type difference in

Py/Ta and the Py surface oxidation. There must be deeper reasons behind the sign change.

3.3.3 MgO base layer dependence

We have seen that the MgO plays a crucial role in the polarity change in the structure studied, in the following data, I changed the MgO thickness from 0-4nm while keep the Py and Ta thickness fixed at 1.6nm and 4nm respectively.

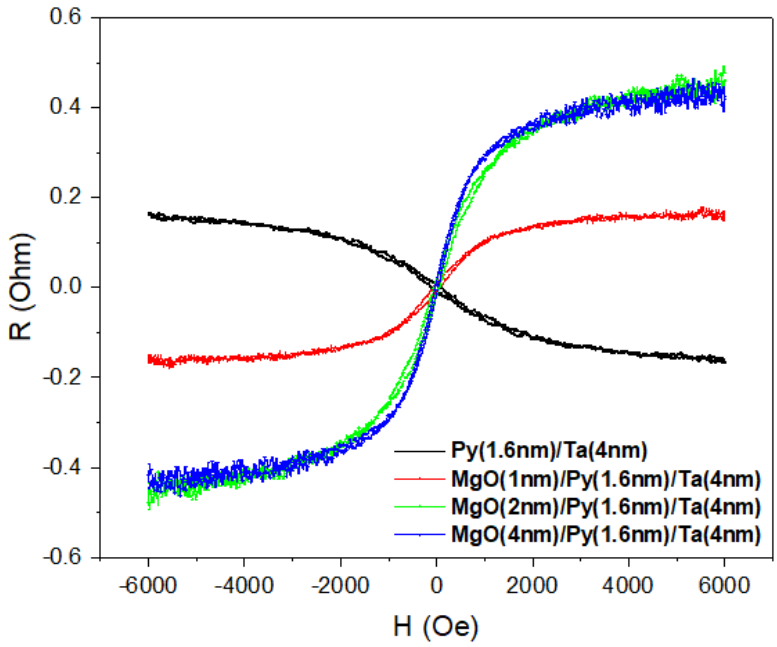

Figure 3.6: AHE for MgO(0-4nm)/Py(1.6nm)/Ta(4nm).

From the data, we can see that the MgO layer under the Py layer does play an important part in the polarity change of the AHE signal. The polarity is negative without MgO layer and changed to positive with even very thin layer of MgO. The magnitude of the positive AHE increases with increasing thickness of the MgO and saturated when the MgO thickness is beyond 2nm.

We can also see that the absolute magnitude of the AHE signal is even stronger with MgO underlayer than without.

3.3.4 Permalloy thickness dependence

In the next step, I changed the Py thickness and we can see that the samples with different Py thickness show different strength in the magnetic anisotropy. When the thickness of Py is about 1.6nm, the inplane anisotropy is weakest and the sample almost shows an out of plane anisotropy.

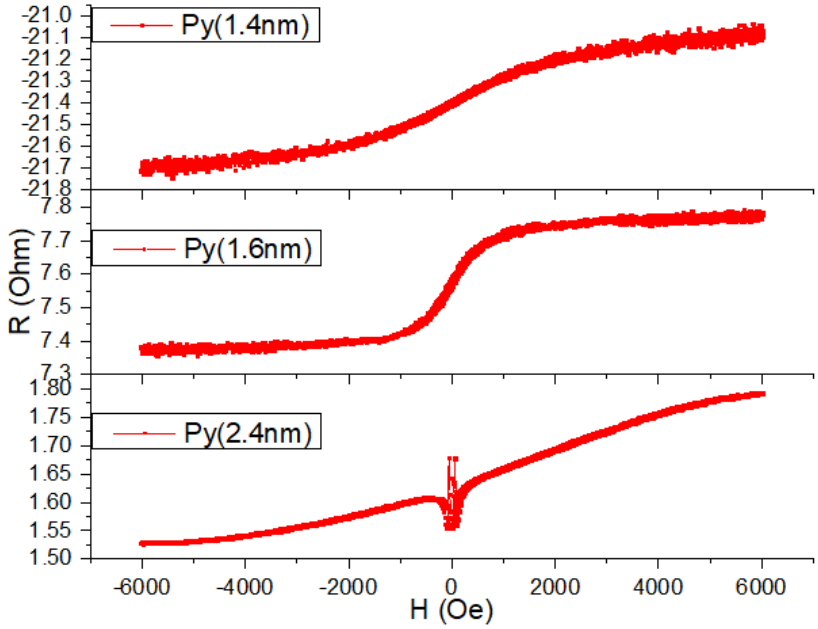

Figure 3.7: AHE data for Ta(3nm)/MgO(2nm)/Py(1.4, 1.6, 2.4nm)/Ta(4nm)

From the data above, we can see that the magnetic anisotropy of the samples almost points out of plane when Py is about 1.6nm. With Py thickness increases, the AHE signal shows sharp peaks in the middle and the curve is not totally antisymmetric about the y axis anymore as the AHE

signal should be. This is because when doing the measurement, the external magnetic field cannot be perfectly perpendicular to the plane of the sample and there is always a small in plane component of the magnetic field. Also, indium leads are placed across the sample to measure the Hall voltage and we didn't have the lithography equipment to make Hall bars. There is always a small misalignment of the leads that causes the longitudinal resistance of the sample to be included in the Hall signal measurement. The longitudinal resistance can be positive and negative depending on direction of the misalignment of the leads across the sample as can be seen from the data above. The dependence of the longitudinal resistance of the sample versus the magnetic field is the Anisotropic Magnetoresistance(AMR) and is symmetric about the y axis. Because of the small in plane component of the field, there is a sharp peak at the center of the sample. This means that the sample shows strong in plane magnetic anisotropy when the Py thickness is increased. To get the True AHE signal, we have to get rid of the symmetric part of the signal while the antisymmetric part is the true AHE signal. The following is the analyzed AHE signal for Si/SiO2/Ta(3nm)/MgO(2nm)/Py(vary thickness)/Ta(1 or 4nm) samples.

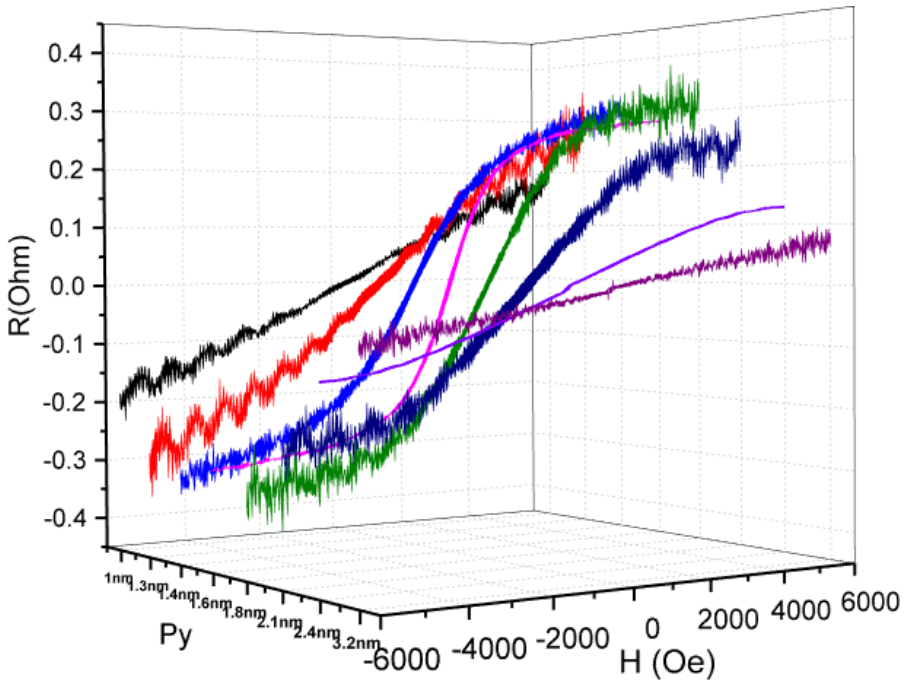

Figure 3.8: AHE signals for the Ta(3nm)/MgO(2nm)/Py(vary thickness)/Ta(4nm)

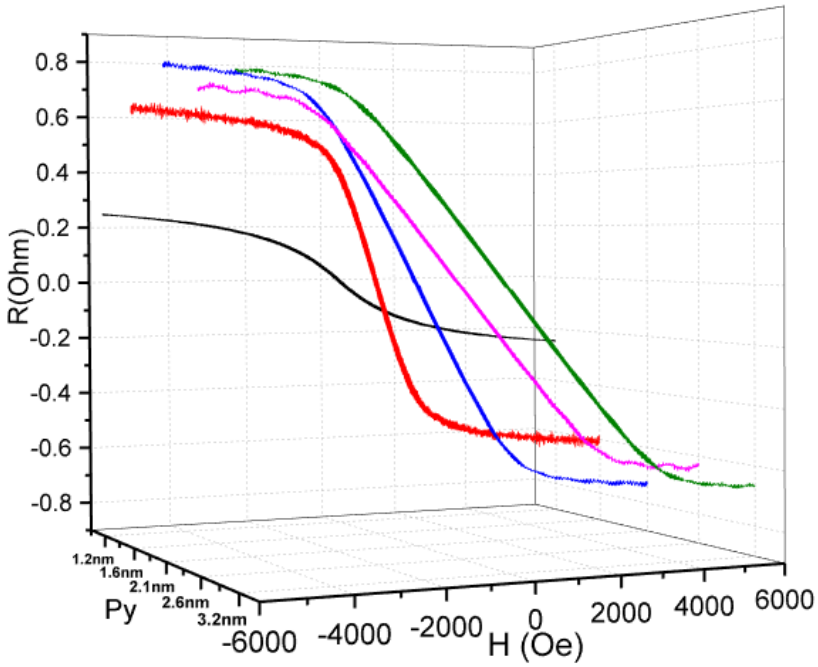

Figure 3.9: AHE signals for the Ta(3nm)/MgO(2nm)/Py(vary thickness)/Ta(1nm)

We can see from the above data that the in plane anisotropy of the sample is stronger for both very thin and thickner Py. When Py is close to 1.6nm, the in plane anisotropy is weakest and it tends to show out of plane anisotropy. Also, regardless of the Py thickness, the samples always show a negative AHE polarity when the Ta thickness is 1nm and positive polarity when the Ta thickness is 4nm. This indicates that the Py thickness does not affect the polarity of the AHE of the structure.

3.3.5 Effect of Ta base layer

Lastly, I studied the structure of Ta(3nm)/Py(1.6nm)/Ta(0-5nm). We have already seen that without MgO and Ta base layer, there is no polarity change. Now, I remove the MgO layer only and keep the 3nm Ta base layer, we can see that the polarity changes in these set of samples but it needs a much thicker Ta capping layer to fully switch the polarity. When Ta thickness is 4nm, although the ordinary Hall effect signal is already positive, the inner signal which is due to the AHE is still negative.

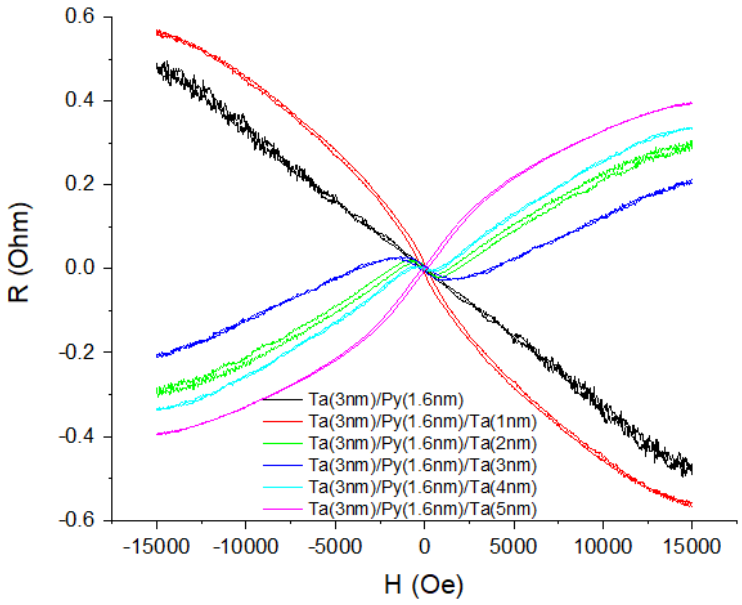

Figure 3.10: AHE signal for Si/SiO2/Ta(3nm)/MgO/Py(1.6nm)/Ta(0-5nm) sample.

I also annealed the sample Si/SiO2/MgO(2nm)/Py(1.6nm)/Ta(4nm) in 200 C for 40 min. For the Si/SiO2/Ta(3nm)MgO(2nm)/Py(1.6nm)/Ta(4nm) sample, I measured the Hall resistance again 5 months after the sample is fabricated.

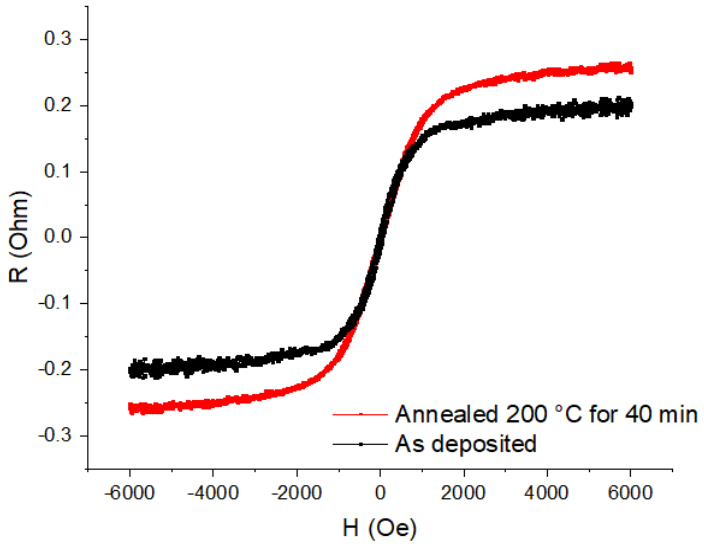

Figure 3.11: Annealed Si/SiO2/ MgO(2nm)/Py(1.6nm)/Ta(4nm) vs as deposited.

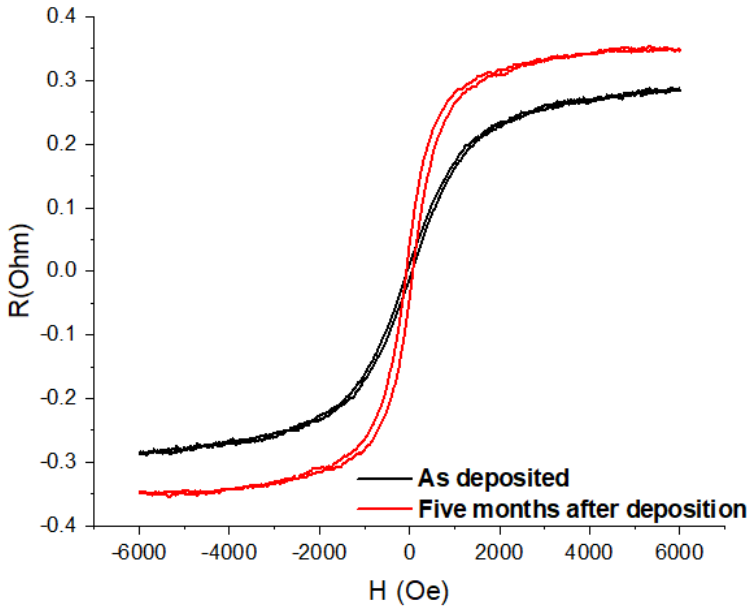

Figure 3.12: AHE for as deposited Si/SiO2/Ta(3nm)/ MgO(2nm)/Py(1.6nm)/Ta(4nm) and 5 months later after deposition

From the above graph, we can see that the both annealing and prolonged ambient environment exposure will increase the magnitude of the Hall resistivity. The polarity of both are not changed by the treatment. We can also see that the sample tends to point more to out of plane after long time ambient environment exposure. I assume that the annealing and the prolonged exposure will change the interfacial morphology of the samples. Therefore, the interface effect makes great contribution to the measured sign change in AHE.

3.3.6 Spin Polarization of MgO/Py/Ta measured by ARS

Using the low temperature transport system, I also measured the ARS spectra of the Si/SiO2/Ta(3nm)/MgO(2nm)/Py(1.6nm)/Ta(4nm) sample and compared it to that of the Si/SiO2/Py(4.2nm) sample.

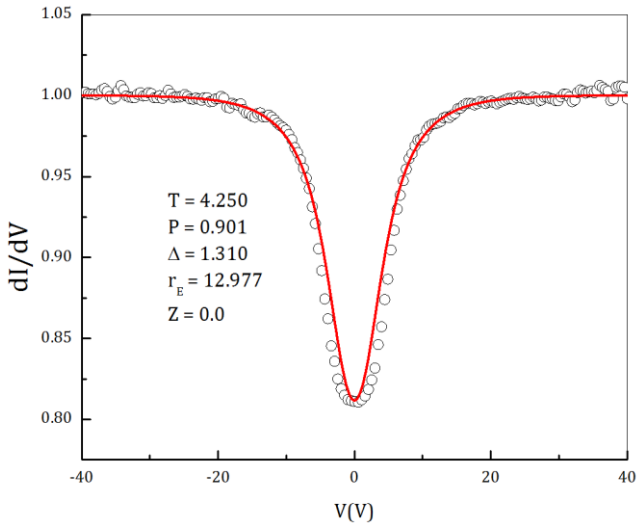

Figure 3.13: ARS curve for Si/SiO2/Ta(3nm)/MgO(2nm)/Py(1.6nm)/Ta(4nm) sample.

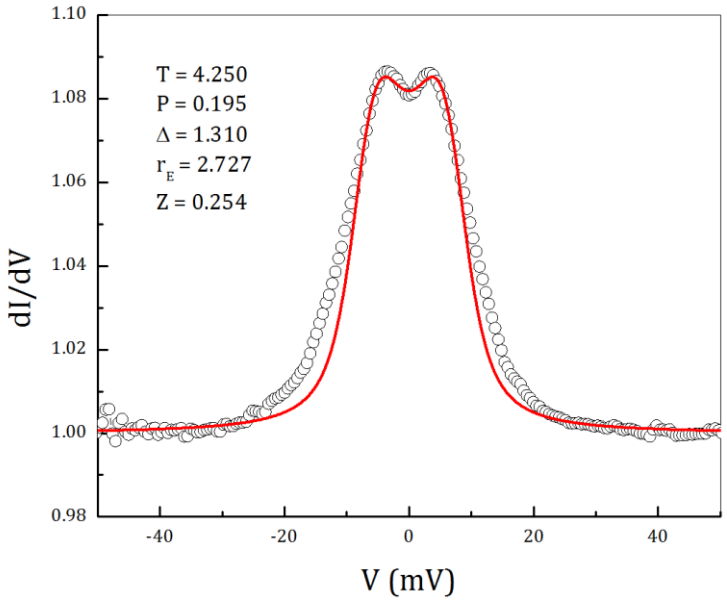

Figure 3.14: ARS curve for Si/SiO2/Py(4.1nm) sample.

From the above curve, we can see that the spin polarization of the Si/SiO2/Ta(3nm)/MgO(2nm)/Py(1.6nm)/Ta(4nm) P=0.9 is much higher than that in the pure Py sample which has a spin polarization of about 0.3. In our measurement, the spin polarization of 4.1nm Py on SiO2 is about 0.195. The P=0.9 is even higher than that in the half metal LSMO which has an intrinsic spin polarization of about 0.812. As has been discussed, the spin polarization is the difference of the spin up electrons and spin down electrons near the Fermi level in a material. This indicates that there is a substantial band structure difference between the MgO/Py/Ta trilayer and the Py layer. In the trilayer structure, there are hybridizations of the Fe, Ni 3d orbitals and the Ta 5d orbitals. There are also hybridization of the 3d orbitals of the Fe and the 2p orbitals of the O due to Fe-O bond formation. These are strong spin orbital interactions which lift the degeneracy in the bands and there can be large difference in the electronic configurations near the Fermi level. In the intrinsic contribution to the anomalous Hall effect scenario, the change in band structure due to spin orbit coupled band hybridization will change the Berry curvature in momentum space. By integrating the Berry curvature in the occupied bands up to the Fermi level, the total Berry curvature might change substantially or even change sign.

3.4 The Effect of Other Heavy Metals as Capping Layers

In this section, I study the AHE of the structure Si/SiO2/MgO/Py/Hf. This is essentially replaced the Ta capping layer by the Hf capping layer.

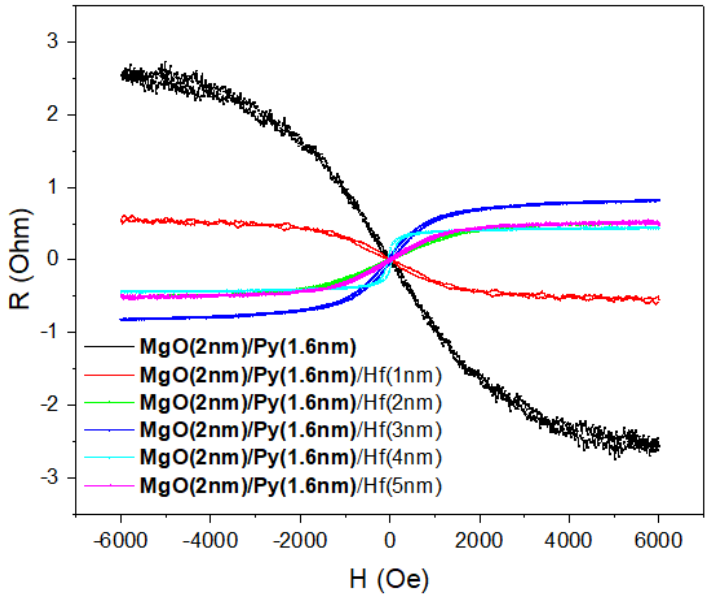

3.15: AHE signal for Si/SiO2/MgO(2nm)/Py(1.6nm)/Hf(0-5nm) structure.

From the above data, we can see that there is also a polarity change in the AHE signal with increasing Hf thickness while keeping the thickness of the other layer fixed. For this time, the positive AHE signal is highest when Hf is about 3nm and decreases a little bit when Hf thickness is further increased. This is contrary to the saturation behavior when Ta is used as capping layer. Also, when Hf is about 4nm, the sample almost shows higher perpendicular magnetic anisotropy than Ta capped samples.

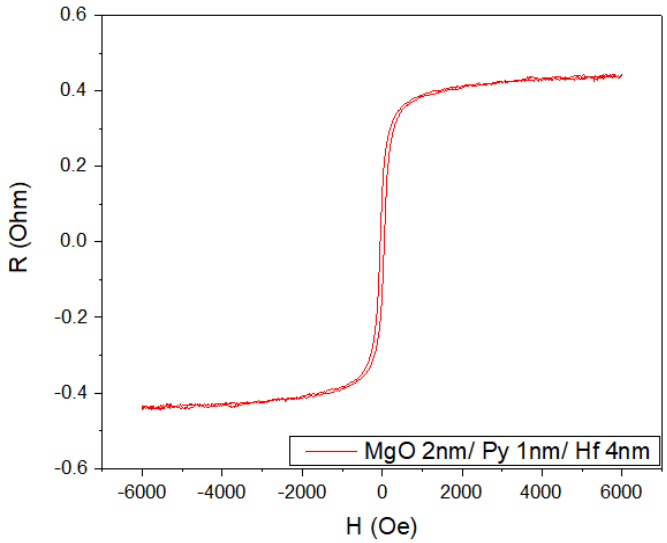

3.16: AHE signal for Si/SiO2/MgO(2nm)/Py(1.6nm)/Hf(4nm) structure.

I also measured the magnetoresistance of the sample for 1.6nm Py, the magnetic field is applied in plane parallel to current, in plane perpendicular to current and out of plane respectively.

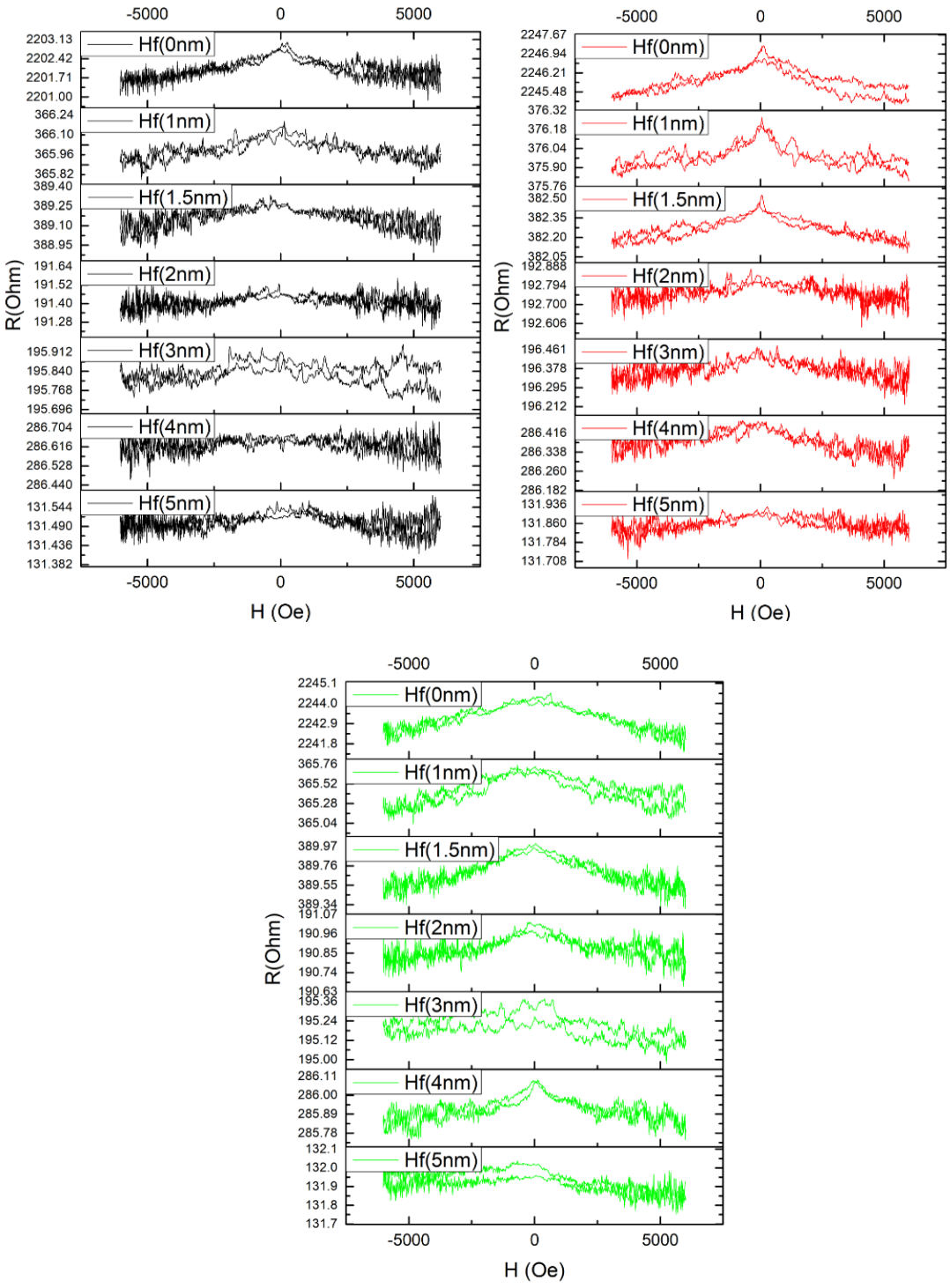

Figure 3.17: Magnetoresistance for the structure Si/SiO2/MgO(2nm)/Py(1.6nm)/Hf(0-5nm), the first column(black) is in plane field parallel to current, the second column(red) is in plane field perpendicular to current, the third column(green) is out of plane field.

From the magnetoresistance curves, we can see that the structure doesn't show strong in plane anisotropy or out of plane anisotropy. There is no profound difference in the in plane and out of plane magnetoresistance.

The angular dependence of the structure is also measured, I measured the sample with Hf thickness of 1nm, 2nm, 4nm which corresponds to the negative polarity, transition region and positive polarity respectively.

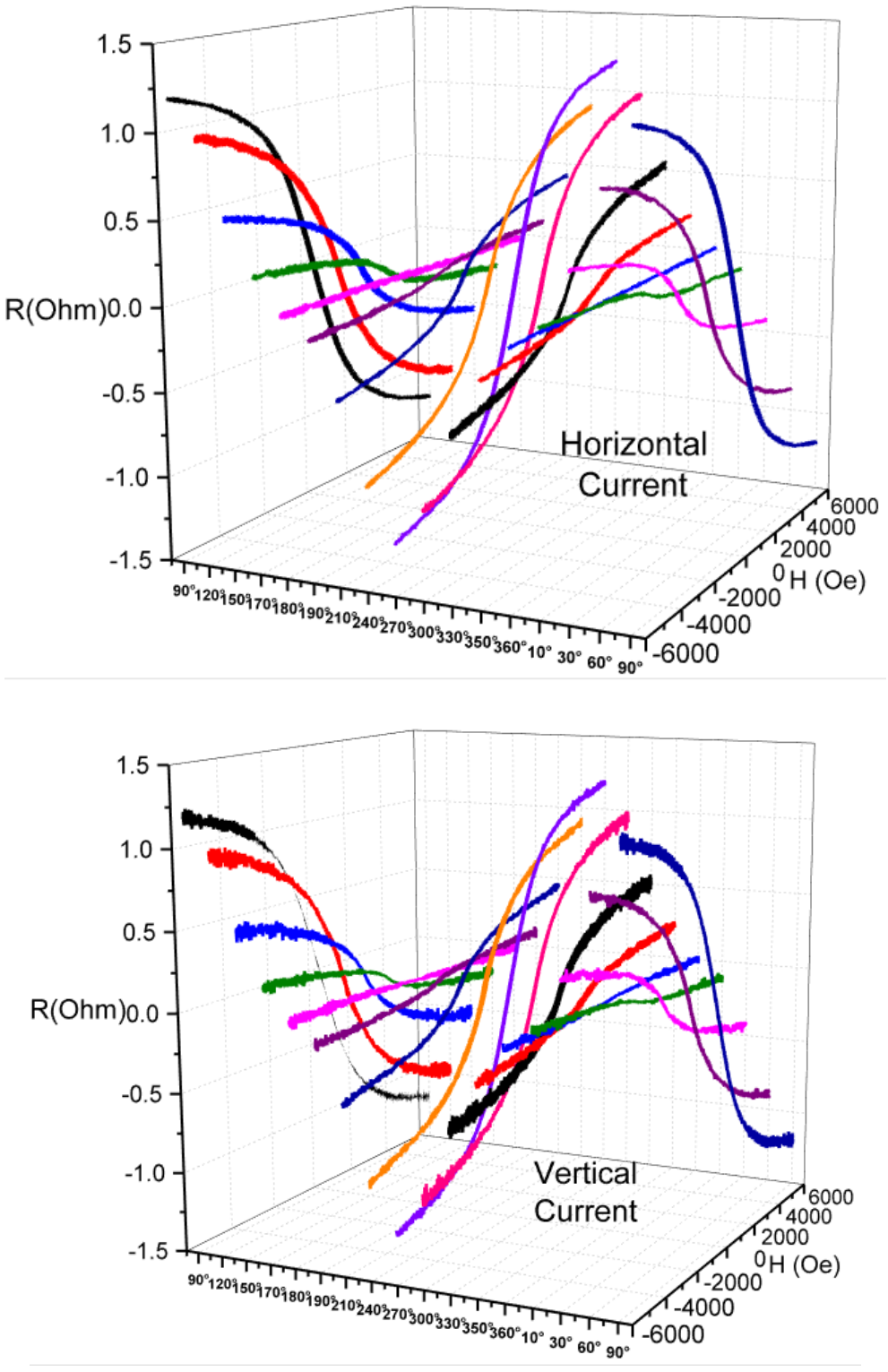

Figure 3.18: Angular dependence of the AHE for Si/SiO2/MgO(2nm)/Py(1.6nm)/Hf(1nm), left is the case when the current is applied horizontally and right figure is when current is applied vertically.

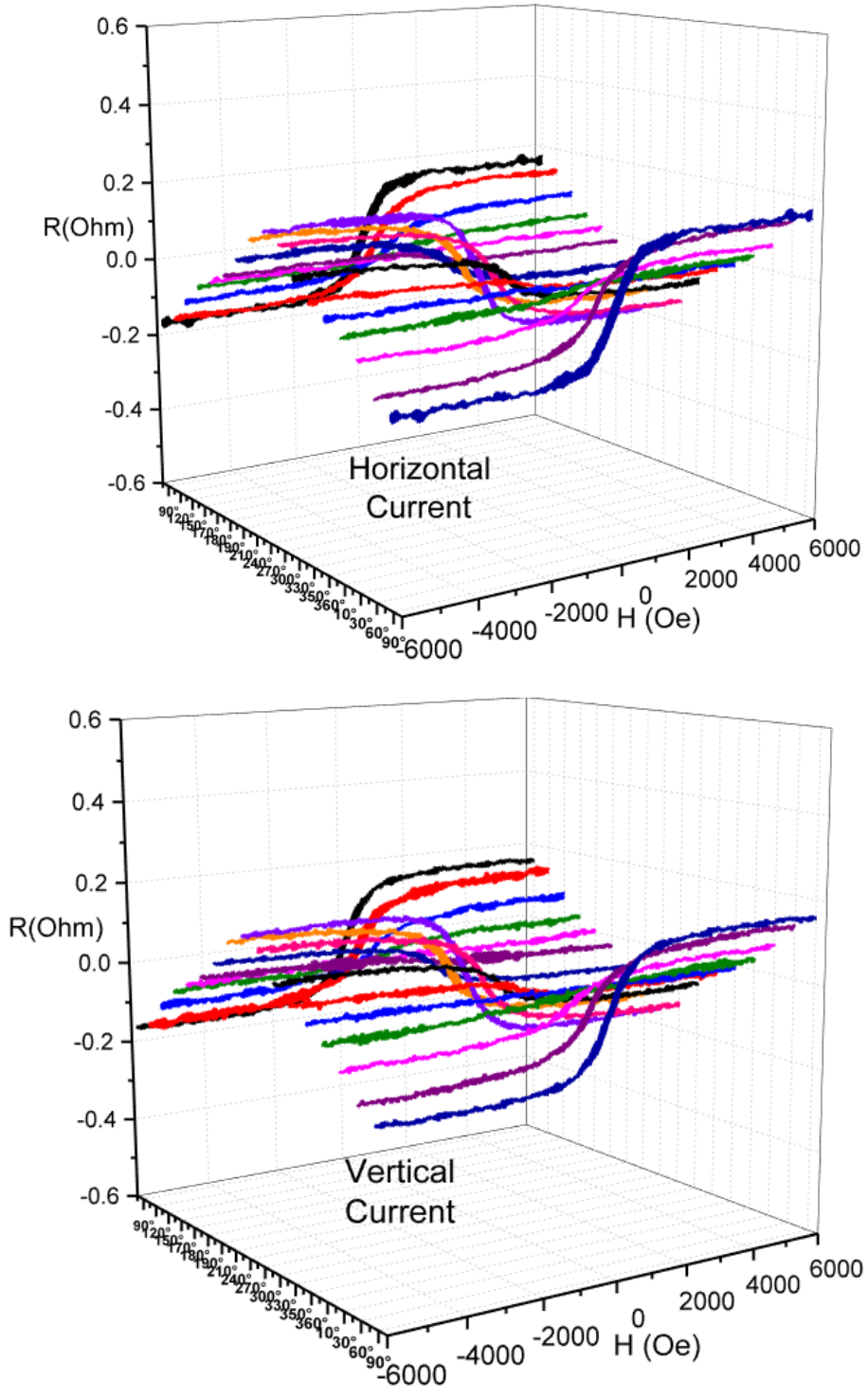

Figure 3.19: Angular dependence of the AHE for Si/SiO2/MgO(2nm)/Py(1.6nm)/Hf(2nm), left is the case when the current is applied horizontally and right figure is when current is applied vertically.

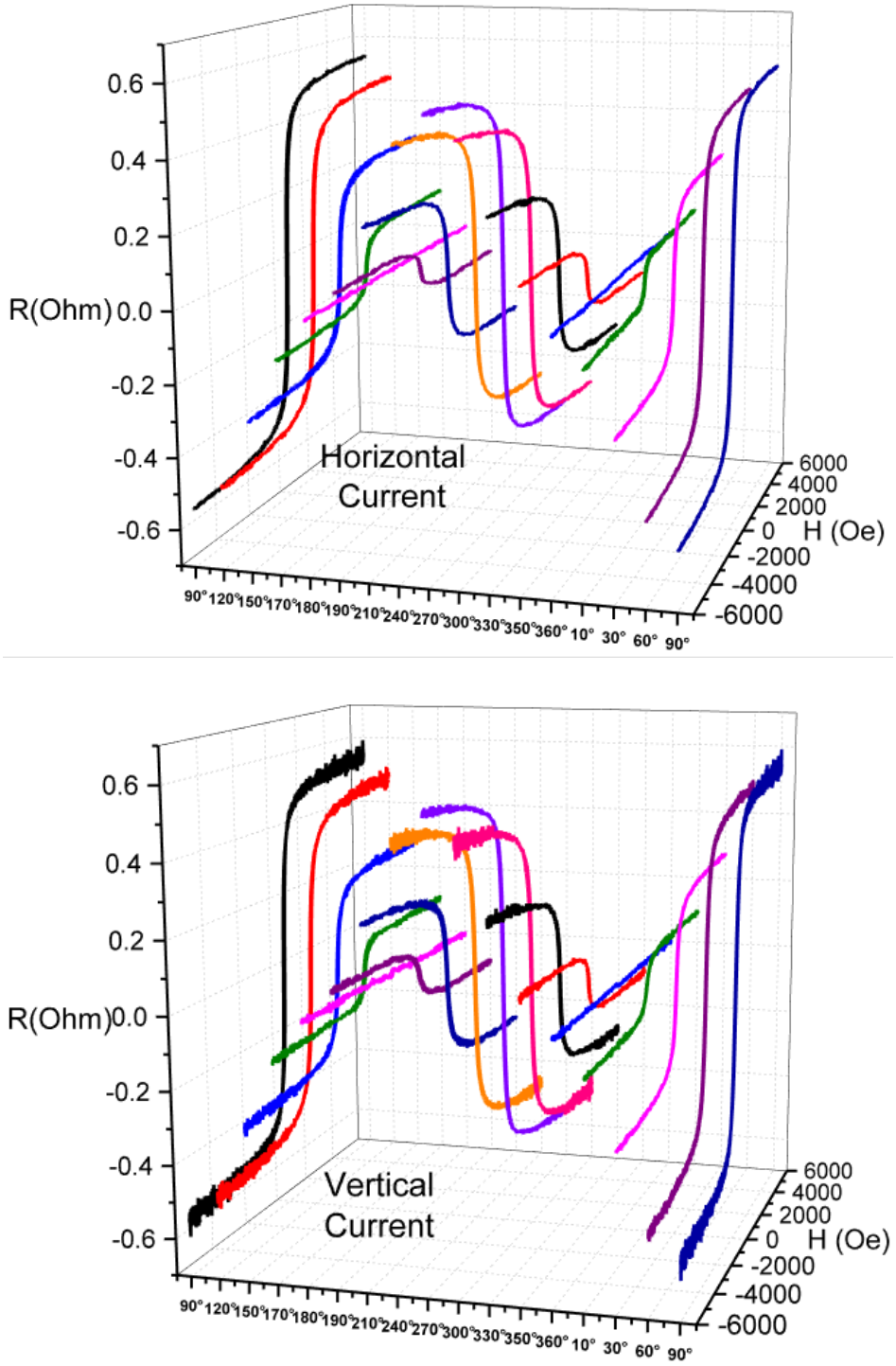

Figure 3.20: Angular dependence of the AHE for Si/SiO2/MgO(2nm)/Py(1.6nm)/Hf(4nm), left is the case when the current is applied horizontally and right figure is when current is applied vertically.

I also increased the thickness of the Py layer in this structure, so the Py thickness is now 2.3nm. The dependence of the AHE signal on Hf capping layer thickness is as follows:

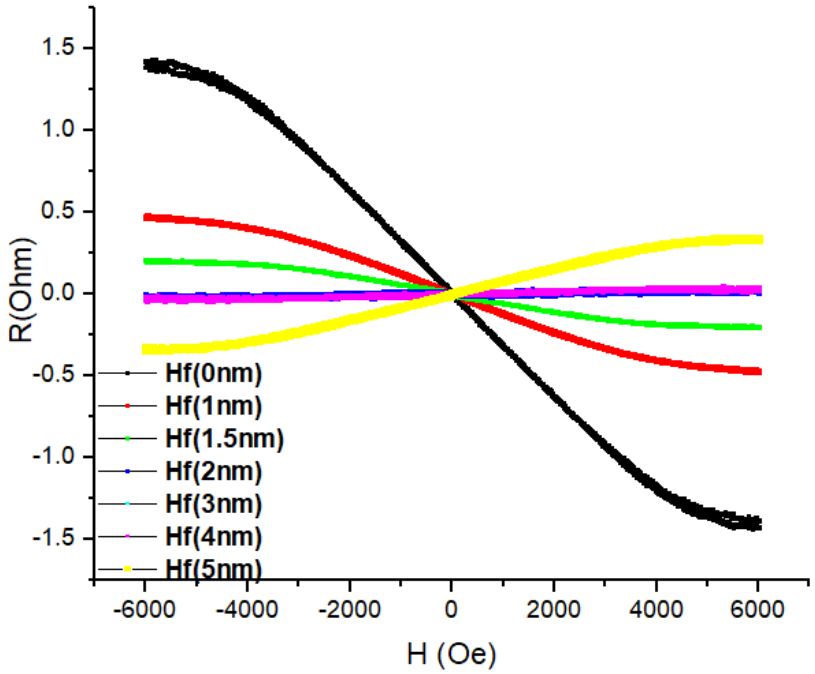

Figure 3.21: AHE signal for structure Si/SiO2/MgO(2nm)/Py(2.3nm)/Hf(0-5nm).

We can see that the polarity of the AHE also change sign from negative to positive as Hf thickness increases and the structure with 2.3nm Py has more tendency to point in plane than out of plane as compared with 1.6nm Py samples. This means that the thickness of the Py plays a critical role in the magnetic anisotropy of the structure.

The magnetoresistance of the of the Si/SiO2/MgO(2nm)/Py(2.3nm)/Hf(0-5nm) sample is also measured.

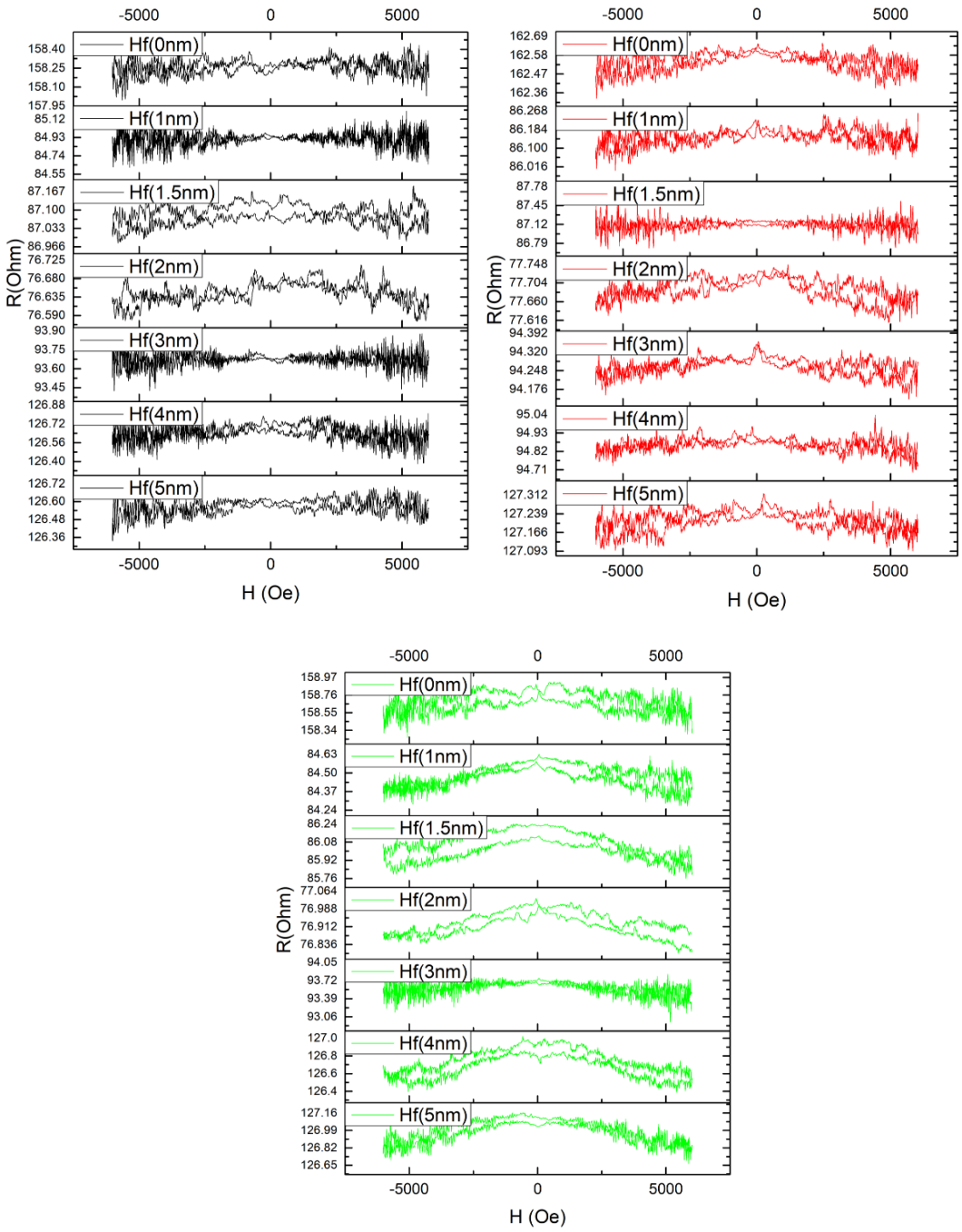

Figure 3.22: Magnetoresistance for the structure Si/SiO2/MgO(2nm)/Py(2.3nm)/Hf(0-5nm), the first column(black) is in plane field parallel to current, the second column(red) is in plane field perpendicular to current, the third column(green) is out of plane field.

In this section, I replaced the capping layer by Pt. The structure now is Si/SiO2/MgO(2nm)/Py(1.6nm)/Pt(0-4nm). We can see that the Pt layer will also induce the polarity change in the AHE signal of the structure.

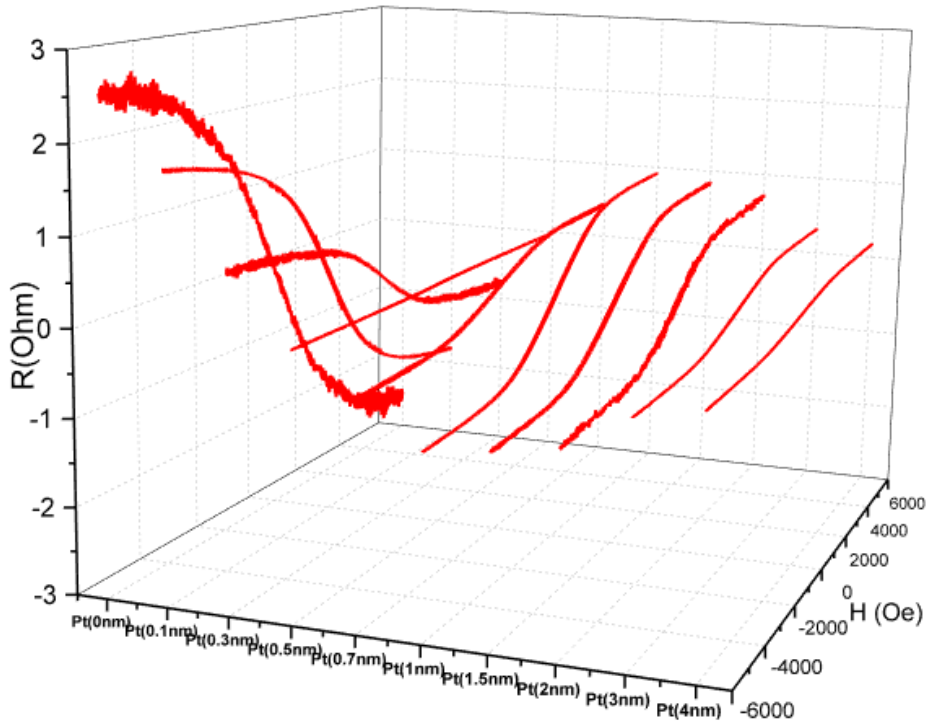

Figure 3.23: AHE signal for the structure Si/SiO2/MgO(2nm)/Py(1.6nm)/Pt(0-4nm).

The transition in the polarity change happens when the Pt thickness is about 0.5nm. As the Pt thickness is higher than 1.5nm, the positive strength of the AHE signal stopped increasing and decreases as Pt thickness increases. The magnetoresistance of the same structure is also measured. This time, the magnetic field is only applied out of plane.

The atomic force microscopy(AFM) image is also measured for MgO(2nm)/Py(1.6nm)/Pt(0.1nm, 0.5nm, 3nm) samples.

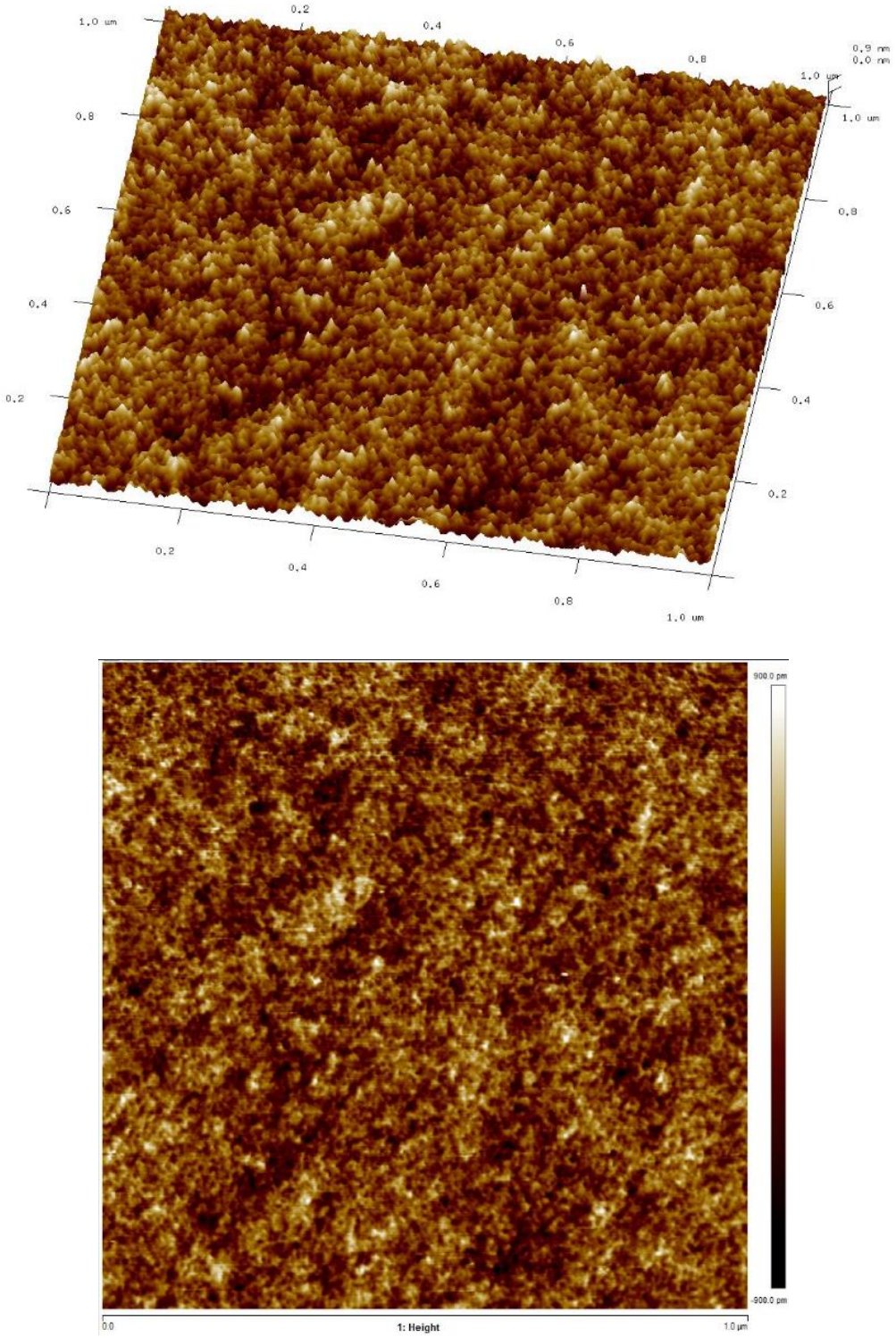

Figure 3.24: AFM images for MgO(2nm)/Py(1.6nm)/Pt(0.1nm). RMS roughness R_q=0.234nm; Average Roughness R_a=0.186nm; Maximum roughness R_{max}=2.41nm.

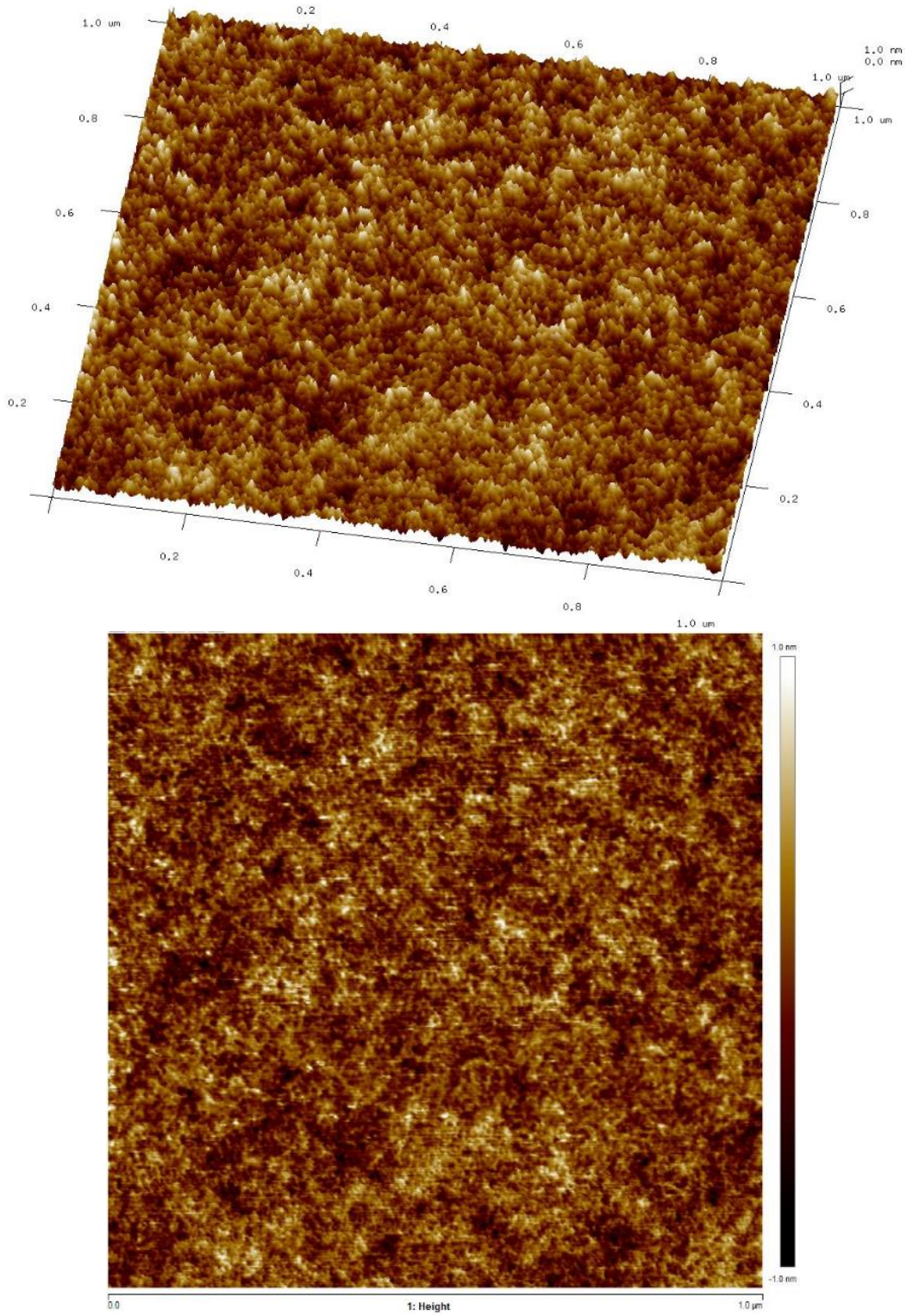

Figure 3.25: AFM images for MgO(2nm)/Py(1.6nm)/Pt(0.5nm). RMS roughness R_q=0.251nm; Average Roughness R_a=0.199nm; Maximum roughness R_{max}=2.76nm.

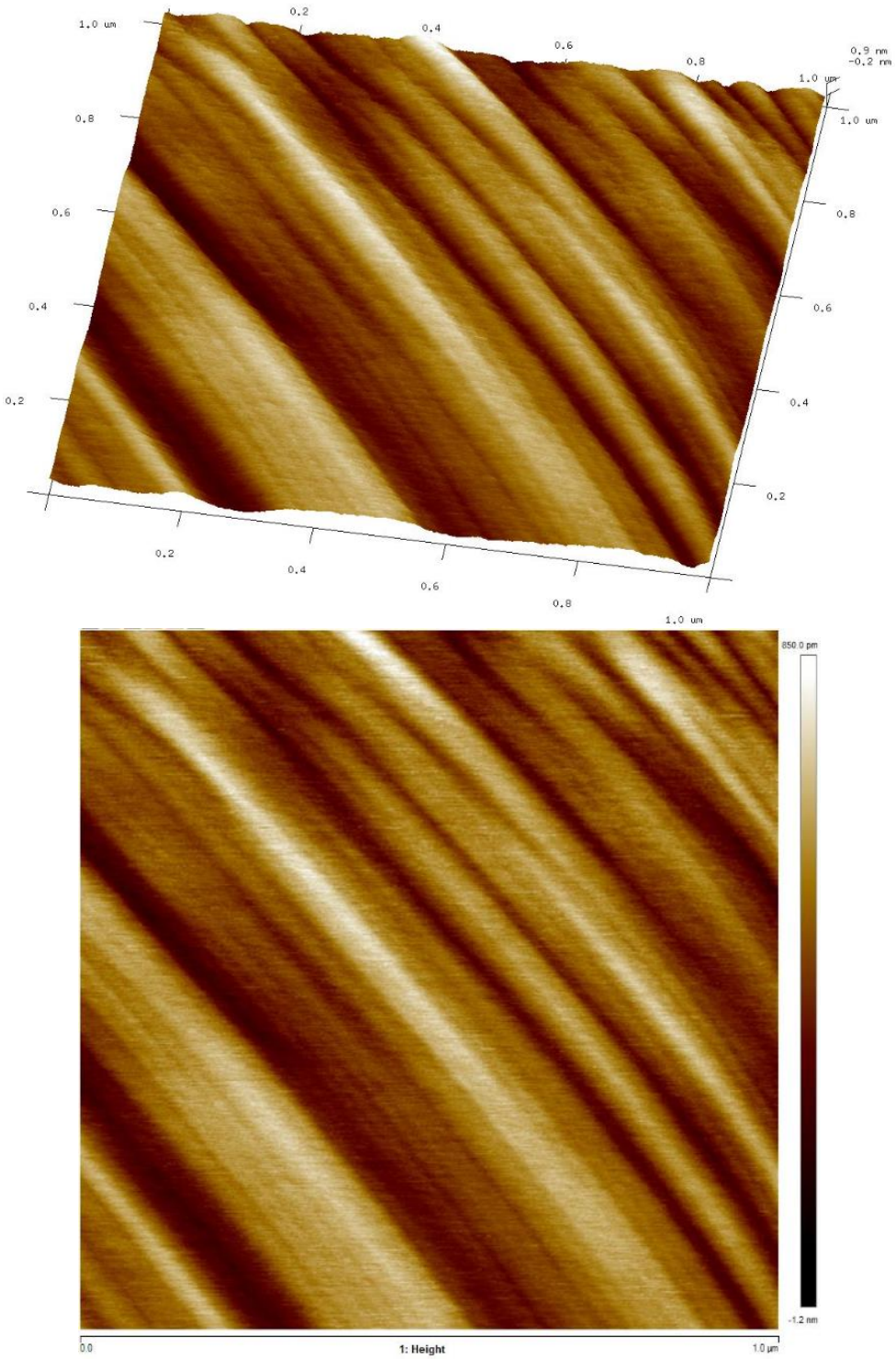

Figure 3.26: AFM images for MgO(2nm)/Py(1.6nm)/Pt(1nm). RMS roughness R_q=0.271nm; Average Roughness R_a=0.224nm; Maximum roughness R_{max}=1.65nm.

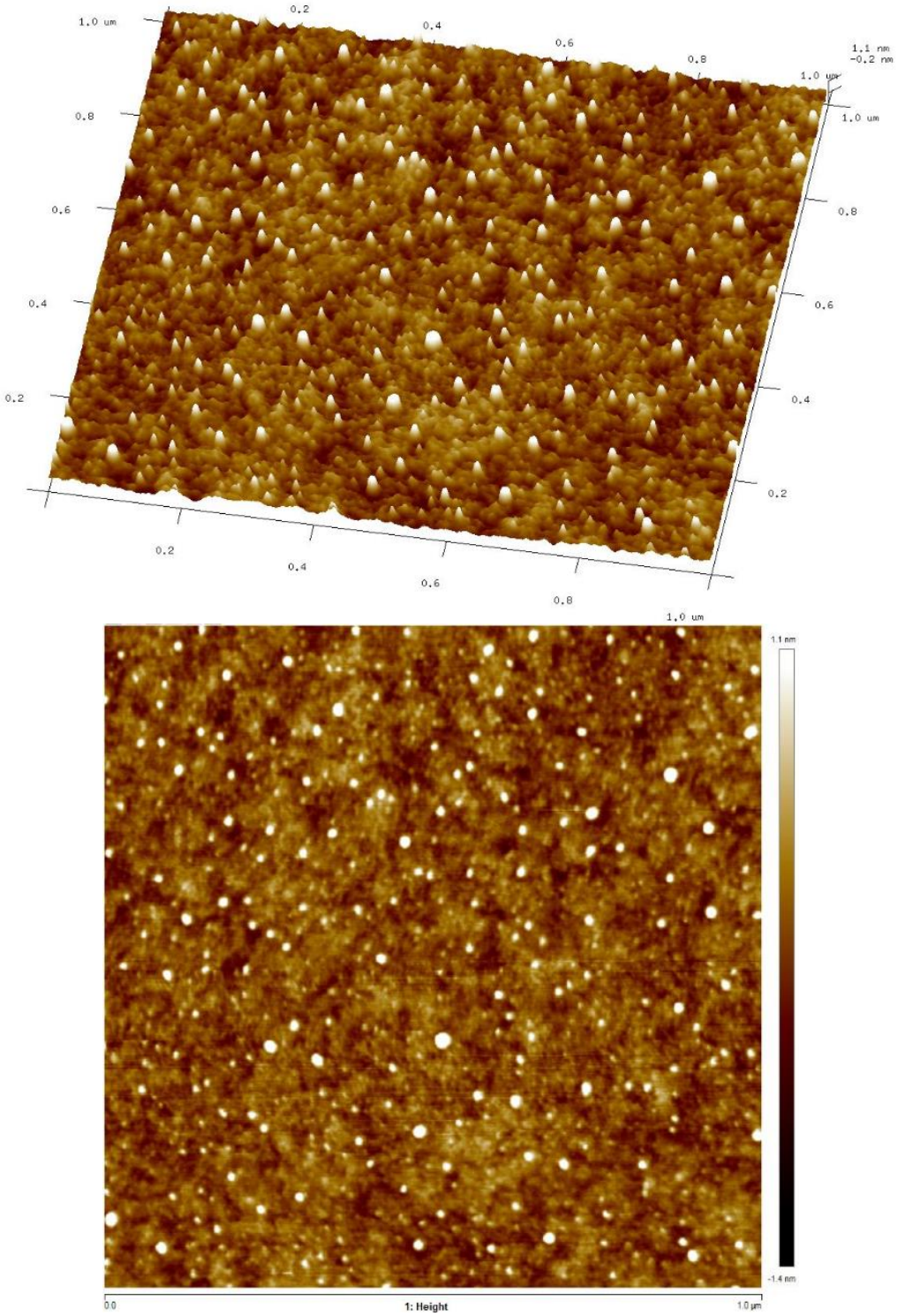

Figure 3.27: AFM images for MgO(2nm)/Py(1.6nm)/Pt(3nm). RMS roughness R_q=0.274nm; Average Roughness R_a=0.183nm; Maximum roughness R_{max}=4.52nm.

The above figures show the AFM images for the Pt capped trilayer samples for different Pt thickness. We can see that the RMS roughness is around 0.2nm for all the samples showing that the surface of the sample is quite smooth. The small dots on the surface of the sample might indicate the islands formation during the Pt deposition.

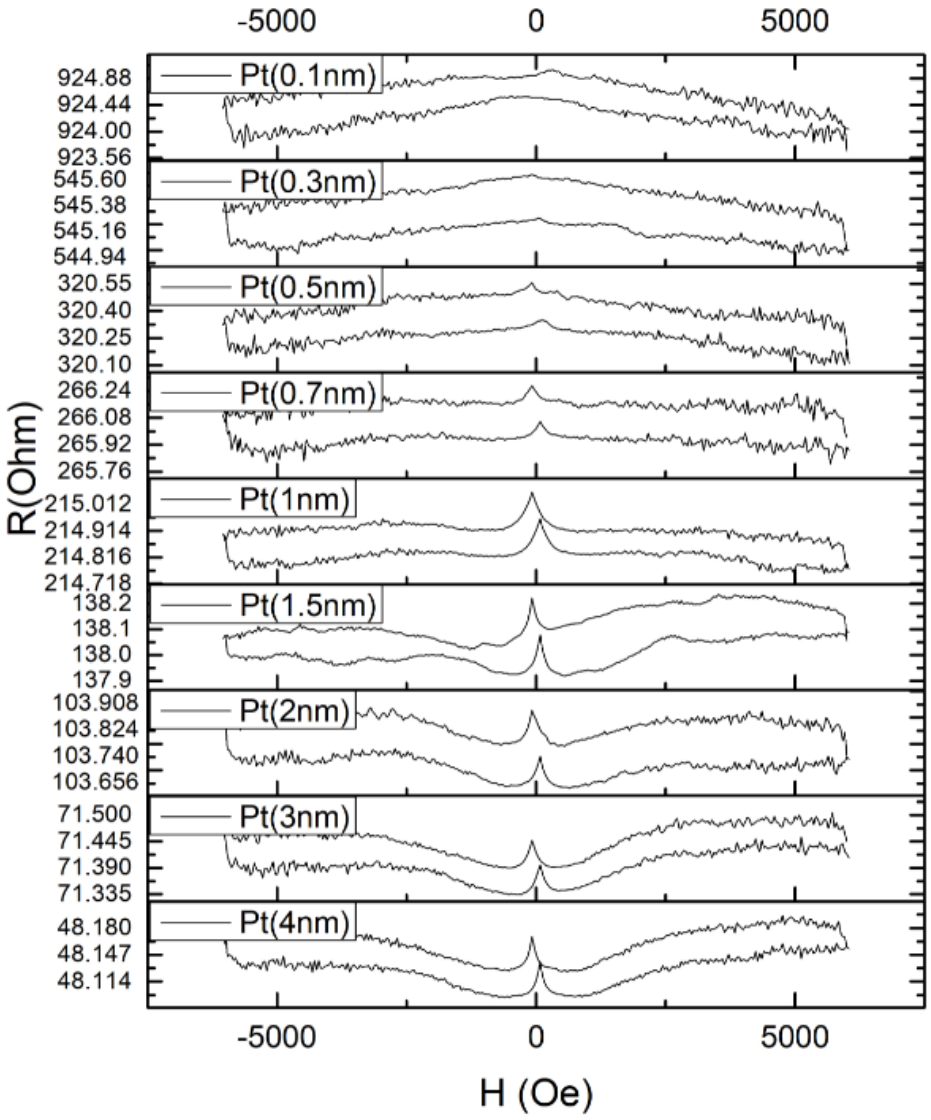

Figure 3.28: Magnetoresistance for out of plane field for the structure Si/SiO2/MgO(2nm)/Py(1.6nm)/Pt(0-4nm).

We can see that there are some systematic changes in the magnetoresistance curve as Py thickness increases. The huge step on two sides of the curve is due to the switching of the magnetic field and is not the intrinsic property of the material. Because the magnetic field points out of plane and the sample should have in plane magnetic anisotropy, the sharp peak at the center might not be due to magnetoresistance. We suspect that the center sharp peak is due to the small in plane component of the magnetic field which induces a planar Hall signal in the sample.

We have seen previously that the Py thickness has a great impact on the magnetic anisotropy of the samples so I increased the thickness of the Py layer. The AHE signal for Si/SiO2/MgO(2nm)/Py(2.3nm)/Pt(0-4nm) structure is measured. The Py thickness is 2.3nm instead of 1.6nm.

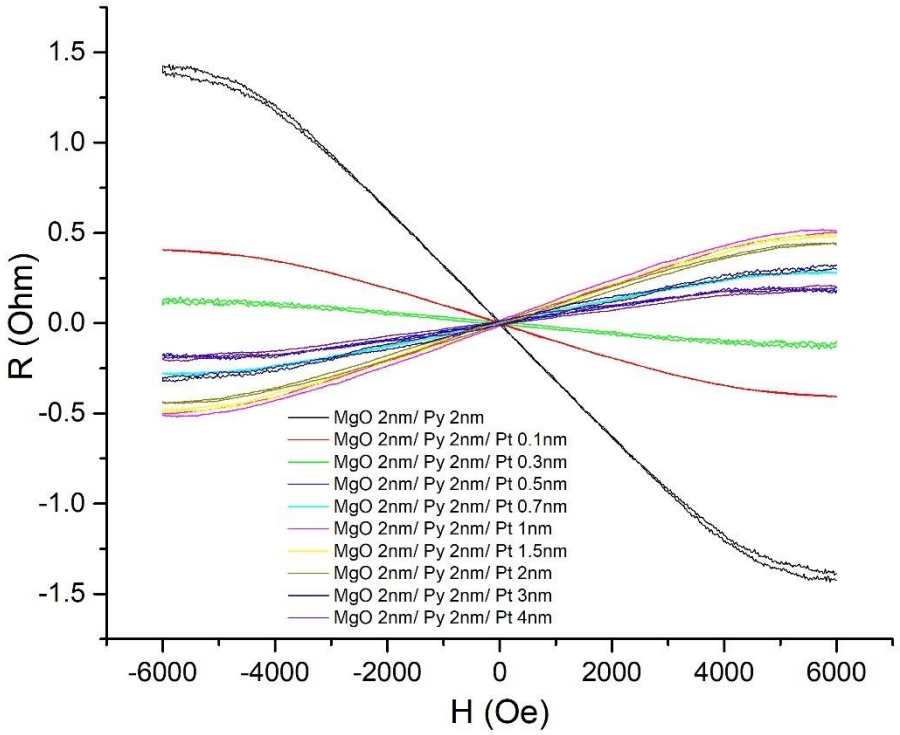

Figure 3.29: AHE curve for the structure Si/SiO2/MgO(2nm)/Py(2.3nm)/Pt(0-4nm).

We can see that there is also a polarity change in the samples and the magnetic anisotropy tends to point in plane in the 2.3nm Py sample more than the 1.6nm sample.

I also measured the AHE signal for the Py/Pt based structure without the MgO underlayer. We have seen that in the MgO/Py/Ta based system, the MgO underlayer is very important for the polarity change. There is no polarity change in the Py/Ta structure without MgO underlayer. The data is as follows.

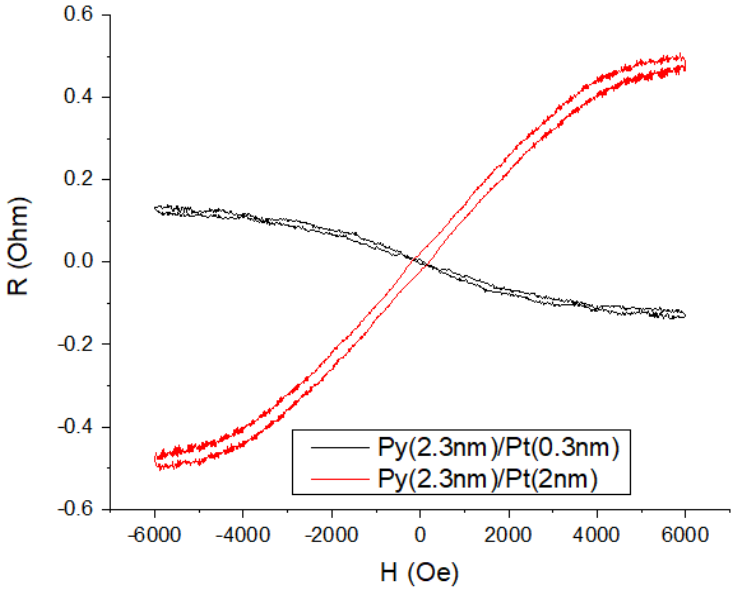

Figure 3.30: AHE curve for the structure Si/SiO2/MgO(2nm)/Py(2.3nm)/Pt(0.3 and 2nm).

I also reversed the sequence of the thin film layers, namely the structure now is Si/SiO2/Pt(0-4nm)/Py(1.6nm)/MgO(2nm). As can be sen from the graph, there is also a polarity change in the AHE signal of the structure.

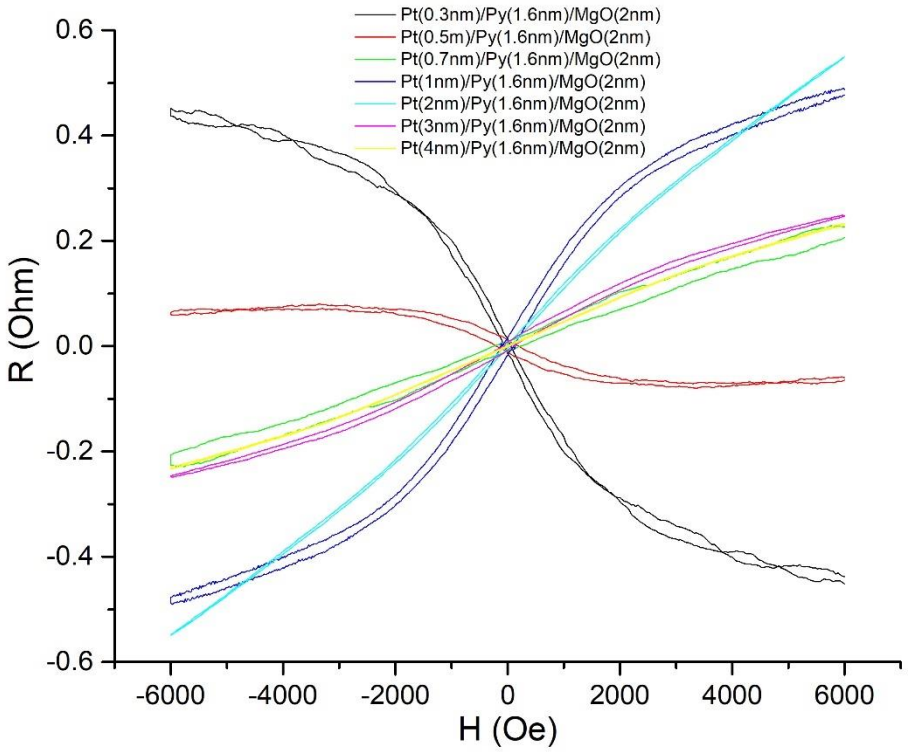

Figure 3.31: AHE curve for the structure Si/SiO2/Pt(0-4nm)/Py(1.6nm)/MgO(2nm)

We can see that the positive polarity of the structure stopped increase but start to decrease when the Pt thickness is beyond 1nm and when the Pt layer is thicker than 1nm the scuve is quite linear and does not show the hysteresis shaped curve.

In conclusion, in the MgO/Py/Pt based structure, there is also a polarity change in the structure with increasing Pt thickness. Unlike in the MgO/Py/Ta based structure, Py/Pt structure also shows a polarity change without the MgO underlayer. When the sequence of the layer is reversed, the polarity change can also be observed with different Pt thickness. This

indicates that the polarity change in MgO/Py/Pt structure is different from that in the MgO/Py/Ta structure. The type of charge carrier in Pt might be different from that in the Py layer, this will induce the charge carrier to deflect to opposite direction in respect of the presence of the MgO underlayer.

In this section, the capping layer is replaced by Ru, the result is as follows.

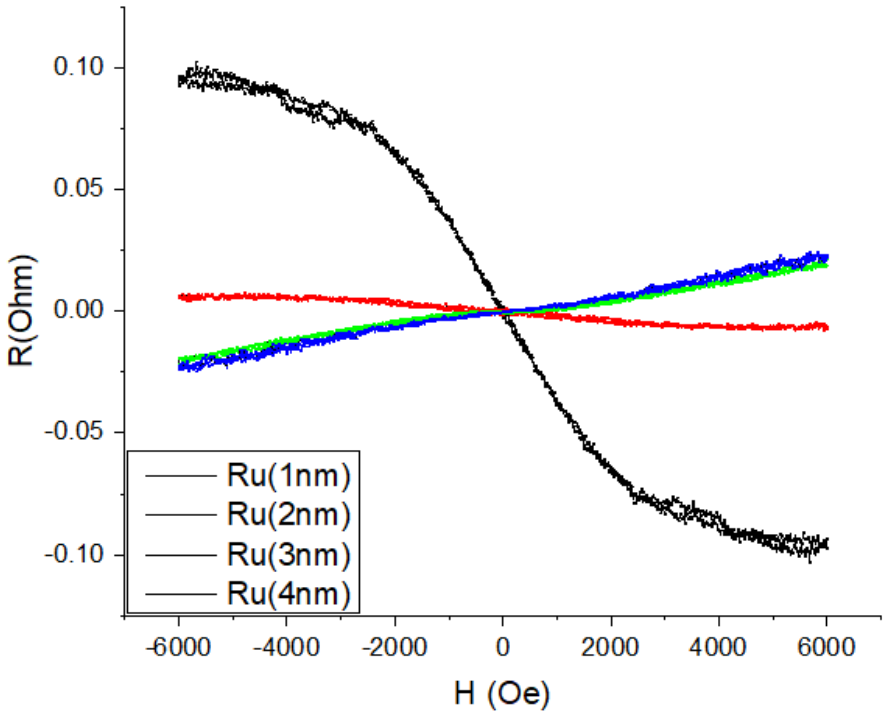

Figure 3.32: AHE curve for the structure Si/SiO2/MgO(2nm)/Py(1.6nm)/Ru(0-4nm).

We can see that the polarity also changed from negative to positive in this kind of structure. However, the magnitude of the AHE value is much smaller than that in the MgO/Py/Ta and MgO/Py/Hf structures. Also, the magnetic anisotropy tends to point in plane as compared with the previous samples.

The structure Si/SiO2/MgO(2nm)/Py(1.6nm)/Cu(0-5nm) is studied in this section, we can see that the Cu capping layer induces some peculiar property to the AHE signal of the structure.

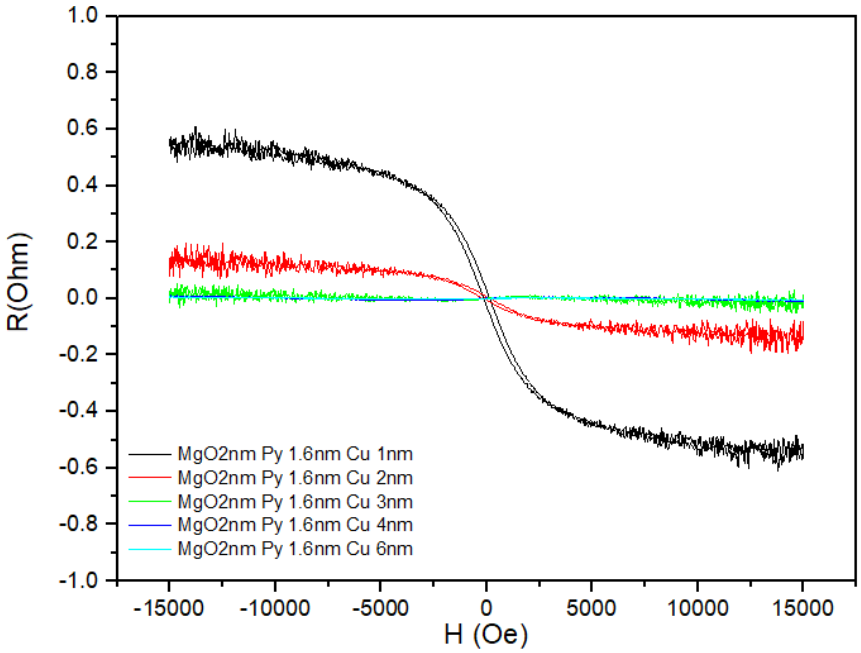

Figure 3.33: AHE curve for the structure Si/SiO2/MgO(2nm)/Py(1.6nm)/Cu(0-6nm).

Instead of polarity change as is observed in Ta, Hf and Ta based structure, there is no polarity change in Cu based structures. The AHE signal rapidly vanishes to zero from negative polarity as the thickness of the Cu increases and does not switch to positive. However, if we enlarge the picture and look carefully enough, the center part which corresponds to the AHE actually switched to positive polarity although the magnitude of the signal is very small.

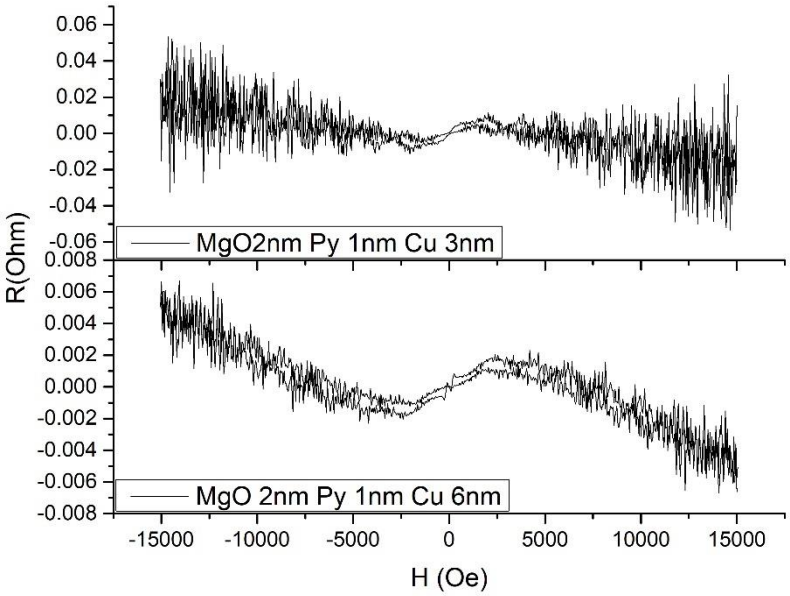

Figure 3.34: AHE curve for the structure Si/SiO2/MgO(2nm)/Py(1.6nm)/Cu(3 and 6nm).

We can see that there is actually a polarity change in the signal as Cu thickness increases but the total magnitude of the signal vanishes rapidly as Cu thickness increases and the curve looks like a perfect line if it is plotted together with thin Cu samples. We can also see that the linear part which corresponds to the ordinary Hall effect does not switch to positive as compared with the Ta, Hf, and Pt based samples. This indicates that the type of charge carrier does not change in the Cu based structure and the polarity change in the AHE signal in this structure has nothing to do with the carrier type change.

In this section, I study the last Py based structure which is capped by W layers.

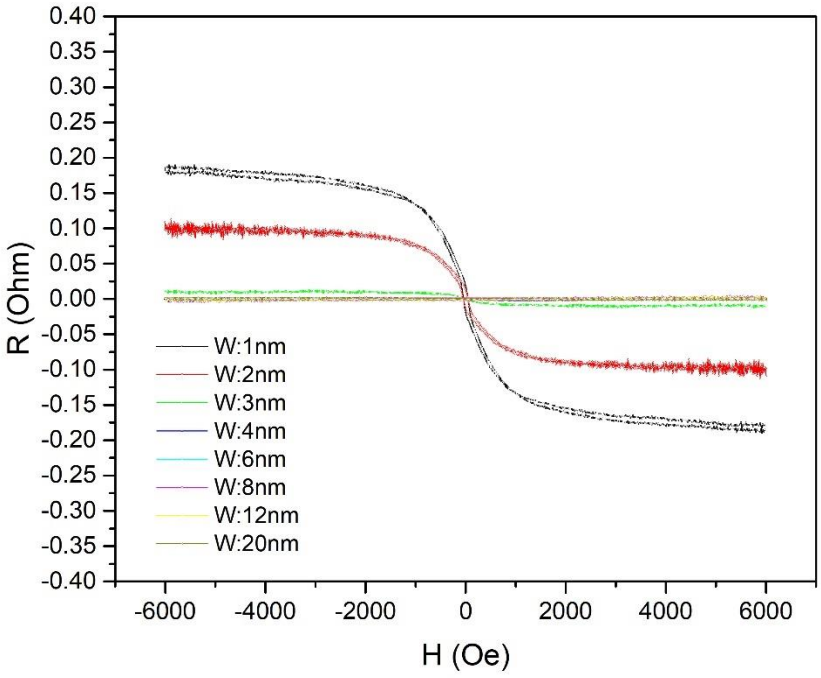

Figure 3.35: AHE curve for the structure Si/SiO2/MgO(2nm)/Py(1.6nm)/W(0-20nm).

From the data, we can see that the W capping layer thickness is increased up to 20nm and the magnitude of the AHE curve dropped rapidly as W thickness increases. To find out the detailed structure of the AHE curves for thick W capped samples, I enlarged the data of some sample with thick W capping layer.

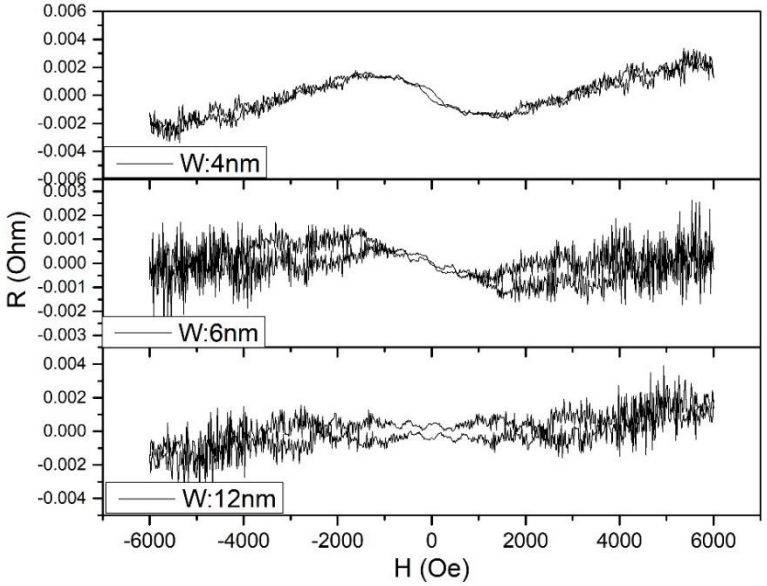

Figure 3.36: AHE curve for the structure Si/SiO2/MgO(2nm)/Py(1.6nm)/W(4, 6 and 12nm).

As can be seen from the data, there is no switching in the center part of the data which corresponds to the AHE. The linear part which is due to the ordinary Hall effect changed from negative to positive as W thickness increases. This is totally in contrary to the Cu capped samples and also different from the Ta, Hf, Pt and Ru capped samples.

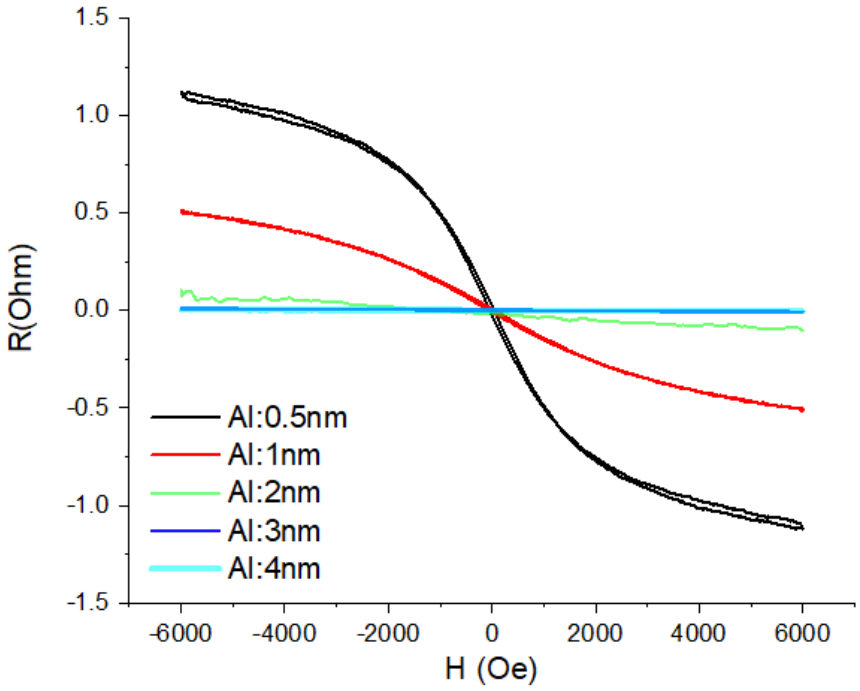

Figure 3.37: AHE curve for the structure Si/SiO2/MgO(2nm)/Py(1.6nm)/Al(0.5-4nm)

In the last part, the MgO(2nm)/Py(1.6nm)/Al(0.5-4nm) sample is fabricated and measured for Hall resistivity. From the above figure, we can see that there is also no sign change in the Al capped trilayer structures like in the case of W capped structures. The Al is special as is compared with the previous HM capping materials because it is a light metal which does not possess strong spin orbit coupling. No sign change in this structure indicates that the strong spin orbit couplings in the HM might be a strong contributor to the sign change in the MgO/Py/HM trilayer structures.

3.5 The Effect of CoFeB as the Magnetic Interlayer

In the last experiment of this chapter, I studied the MgO/CoFeB/Ta based structure using AHE measurement. As is well known, this structure is extensively studied due to strong perpendicular magnetic anisotropy(PMA) and good tunneling magnetoresistance. This has great applications in the spintronic devices. The structure I studied is Si/SiO2/MgO(2nm)/CoFeB(1nm)/Ta(0-4nm) and the reversed structure Si/SiO2/Ta(0-6nm)/CoFeB(1nm)/MgO(2nm).

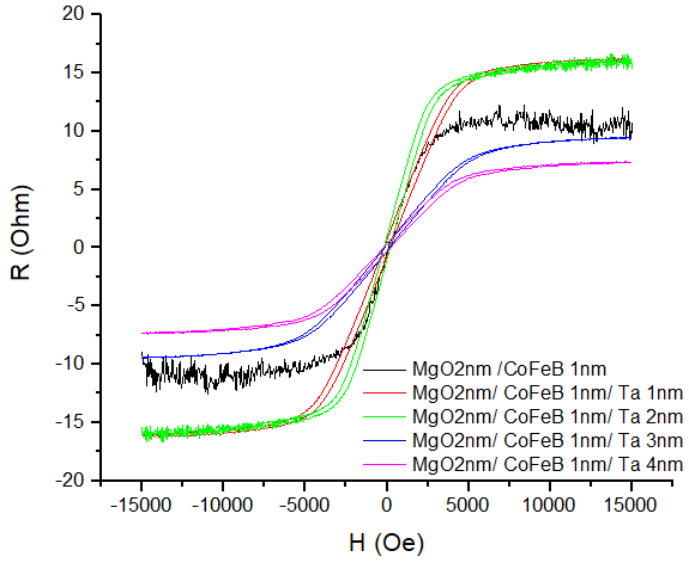

Figure 3.38: AHE curve for the structure Si/SiO2/MgO(2nm)/CoFeB(1nm)/Ta(0-4nm).

From the above data, we can see that the perpendicular anisotropy(PMA) is not obtained in the structure Si/SiO2/MgO(2nm)/CoFeB(1nm)/Ta(0-4nm) by varying the Ta capping layer thickness. The AHE signal always shows a positive polarity in contrary to the negative polarity in the Py based structure when Ta capping layer is thin. We ca also see that the magnitude of the AHE

signal first increases with increasing Ta thickness but decreases after the Ta thickness goes beyond 2nm. The magnitude of the AHE signal in CoFeB based structure is also much stronger than in the Py based structure with anomalous Hall resistance of more than 10 Ohm compared to the less than 1 Ohm anomalous Hall resistance in the Py based samples.

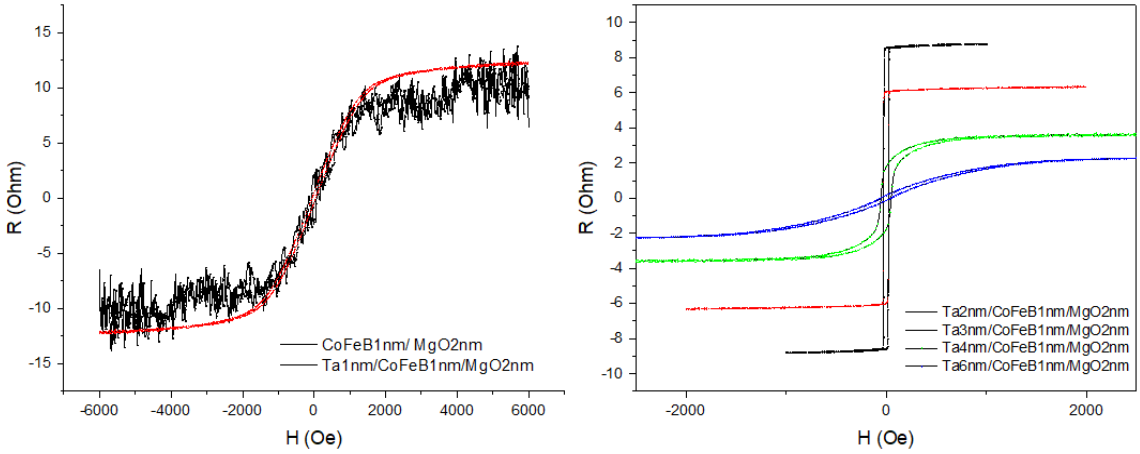

Figure 3.39: AHE curve for the structure Si/SiO2/Ta(0-6nm)/CoFeB(1nm)/MgO(2nm).

The above data is the reversed structure Si/SiO2/Ta(0-6nm)/CoFeB(1nm)/MgO(2nm). This structure has been extensively studied. We can see that perfect perpendicular magnetic anisotropy can be obtained in this structure when the thickness of the tantalum base layer is in the 2-3nm range. The perpendicular anisotropy of the structure does depend on the thickness of the Ta layer so the it plays a crucial role in the magnetic property of the structure in addition to the MgO layer. The magnitude of the AHE signal is also in the 10 Ohm range which is much larger than the Py based structure. The polarity of the AHE signal is always positive in respect

of the Ta layer thickness so the change of polarity is not observed in this structure.

3.6 Conclusion and Discussion

In this chapter, I studied the MgO/Py/HM based structure where the heavy metal can be Ta, Hf, Ru, Pt, W, Cu. I also studied the MgO/CoFeB/Ta based structure. In the MgO/Py/HM based structure, a change in polarity of the AHE is observed when the HM is Ta, Hf, Ru, Cu and Pt and the HM capping layer is increased. When the W is used as the capping layer, no change in polarity is observed. There is also no sign change when Al is used as the capping layer. In the MgO/CoFeB/Ta structure when the permalloy layer is replaced by the CoFeB layer, no change in polarity is observed in the AHE signal. The AHE is said to originate from the intrinsic mechanism which is Berry curvature in the Bloch wave functions of the charge carrier in perfect lattice and the extrinsic mechanism which is skew scattering and side jumps. In thin film samples, interface scattering in multilayers and surface scattering makes contribution to the measured AHE resistance.

Different heavy metals also have different spin-Hall angle. Fer 5-d electron metals such as Pt, Au, Ta, W, the spin-Hall angle can be positive or negative depending on the filling of the 5d electron band. If the 5d band is less than half filled as is the case for Ta and W, the spin Hall angle is negative while if

5d band is more than half filled, the spin Hall angle is positive as is the case for Au and Pt. This is because the sign of the spin orbit coupling term depends on the filling of the 5d bands[28]. The spin Hall angle of the Ta and W have the same sign while is opposite Pt. However, the polarity of the AHE changes in the Ta and Pt capped structures and does not change in W capped structure. Therefore, the spin Hall angle cannot explain the polarity change of the AHE in the structures studied. We have also seen both AHE and ordinary Hall signal change sign in Ta, Hf, Pt and Ru capped structures but in Cu capped structure, only AHE changes sign. The sign of ordinary Hall effect does not change in Cu capped structure. This suggests that there is charge carrier type change in the Ta, Hf, Ru and Pt capped structures and the band structure at the Fermi level changed.

Intrinsic mechanism which is Berry curvature is one way to explain the phenomena. Based on the band structure and integrated Berry curvature calculation, the Berry curvature can change sign abruptly with small perturbation in Fermi level or band structure shift and contributes to the sign change in AHE. The spin polarization of the MgO/Py/Ta(4nm)(P~0.9) is much higher than the spin polarization of a single Py layer, suggesting a profound difference of energy band structure at the interface. This further demonstrates the intrinsic contribution to sign change in anomalous Hall resistivity.

REFERENCE

1. Natao Nagaosa et al., “Anomalous Hall Effect”, Rev. Mod. Phys. 82, 1539 (2010).
2. Z. B. Guo et al., “Effects of surface and interface scattering on anomalous Hall effect in Co/Pd multilayers”, Phys. Rev. B 86, 104433 (2012).
3. Xilin Kou et al., “Magnetic anisotropy and anomalous Hall effect of ultrathin Co/Pd bilayers”, Journal of Applied Physics 112, 093915 (2012).
4. O. Shaya et al., “Extraordinary Hall effect in Co-Pd bilayers”, Journal of Applied Physics 102, 043910 (2007).
5. Sangrok Kim et al., “Magnetic properties of Pd/Co multilayer films studied by Hall effect”, Journal of Applied Physics 73, 6344 (1998).
6. D. Rossenblatt et al., “Reversal of the extraordinary Hall effect polarity in thin Co/Pd multilayers”, Appl. Phys. Lett. 96, 022512 (2010).
7. V. Keskin et al., “Temperature and Co thickness dependent sign change of the anomalous Hall effect in Co/Pd multilayers: An experimental and theoretical study”, Appl. Phys. Lett. 102, 022416 (2013).
8. C. Christides et al., “Polarity of anomalous Hall effect hysteresis loops in $[Pt/Co]_{15}$/AF/$[Co/Pt]_{15}$ (AF=FeMn, NiO) multilayers with perpendicular anisotropy”, Journal of Applied Physics 97, 013901 (2004).

9. J. Zhao et al., “Large extraordinary Hall effect in $[Pt/Co]_5$ /Ru/$[Co/Pt]_5$ multilayers”, Physical Review B 81, 172402 (2010).
10. S. L. Zhang et al., “Large enhancement of the anomalous Hall effect in Co/Pt multilayers sandwiched by MgO layers”, Appl. Phys. Lett. 97, 222504 (2010).
11. C. L. Canedy et al., “Large magnetic moment enhancement and extraordinary Hall effect in Co/Pt superlattices”, Phys. Rev. B 62, 508 (2000).
12. C. L. Canedy et al., “Extraordinary Hall effect in (111) and (100)-orientated Co/Pt superlattices”, Journal of Applied Physics 81, 5367 (1998).
13. J. Caulet et al., “Influence of spin polarized Pt on the extraordinary Hall effect in sputtered Pt/Au/Co/Pt sandwiches”, Journal of Magnetism and Magnetic Materials, Volume 198, Issue 1-3, p. 318-320 (1999).
14. Zhiyong Wang et al., “Proximity-Induced Ferromagnetism in Graphene Revealed by the Anomalous Hall Effect”, PRL 114, 016603 (2015).
15. Sibylle Meyer et al., “Anomalous Hall effect in YIG/Pt bilayers”, Applied Physics Letters 106, 132402 (2015).
16. Xiao Liang et al., “Magnetic Proximity Effect and Anomalous Hall Effect in Pt/$Y_3Fe_{5-x}Al_xO_{12}$ Heterostructures”, PHYSICAL REVIEW APPLIED 10, 024051 (2018).

17. S. Monso et al., “Crossover from in-plane to perpendicular anisotropy in Pt/CoFe/AlOx sandwiches as a function of Al oxidation: A very accurate control of the oxidation of tunnel barriers”, s, Appl. Phys. Lett. 80 (2002) 4157.
18. B. Rodmacq et al., “Crossovers from in-plane to perpendicular anisotropy in magnetic tunnel junctions as a function of the barrier degree of oxidation”, J. Appl. Phys. 93 (2003) 7513.
19. A. Monchon et al., “Analysis of oxygen induced anisotropy crossover in Pt/Co/MOx trilayers”, J. Appl. Phys. 104 (2008) 043914.
20. B. Rodmacq et al., “Influence of thermal annealing on the perpendicular magnetic anisotropy of Pt/Co/AlO_x trilayers”,Phys. Rev. B 79 (2009) 024423.
21. L. E. Nistor et al., “Correlation between perpendicular anisotropy and magnetoresistance in magnetic tunnel junctions”, IEEE Trans. Magn. 46 (2010) 1412
22. S. Ikeda et al., “A perpendicular-anisotropy CoFeB–MgO magnetic tunnel junction”,Nature Mater. 9 (2010) 721.
23. A. Manchon et al., “X-ray analysis of oxygen-induced perpendicular magnetic anisotropy in Pt/Co/AlOx trilayers”, s, J. Magn. Magn. Mater. 320 (2008) 1889.

24. H. X. Yang et al., “Switching characteristics of submicrometer magnetic tunnel junction devices with perpendicular anisotropy”, y, J. Appl. Phys. 97 (2005) 10C919.
25. Yugui Yao et al., “Theoretical Evidence for the Berry-Phase Mechanism of Anomalous Hall Transport: First-principles Studies on $CuCr_2Se_{4-x}Br_x$”, Phys. Rev. B 75, 020401(R) (2007)
26. W. J. Xu et al., “Anomalous Hall Effect in Fe/Gd Bilayers,” EPL (Europhysics Letters), Volume 90, Number 2 (2010)
27. Huei-Ru Fuh et al., “Intrinsic anomalous Hall effect in nickel: A GGA + U study”, PHYSICAL REVIEW B 84, 144427 (2011).
28. H. L. Wang et al., “Scaling of Spin Hall Angle in 3d, 4d, and 5d Metals from $Y_3Fe_5O_{12}$/Metal Spin Pumping”, PRL 112, 197201 (2014).
29. Di Xiao et al., “Berry phase effects on electronic properties”, Reviews of Modern Physics, volume 82, July–September 2010
30. F. D. M. Haldane, “Berry Curvature on the Fermi Surface: Anomalous Hall Effect as a Topological Fermi-Liquid Property”, Phys. Rev. Lett. 93, 206602 (2004)
31. Yugui Yao, et. al., “First principles calculation of anomalous Hall conductivity in ferromagnetic bcc Fe”, Phys. Rev. Lett. 92, 037204 (2004).
32. David J. Griffiths, “Introduction to Quantum Mechanics”, Prentice Hall (1995).

33. Qi Wang et al., “Large intrinsic anomalous Hall effect in half-metallic ferromagnet $Co_3Sn_2S_2$ with magnetic Weyl fermions”, Nature Communications volume 9, Article number: 3681 (2018)
34. Wei-li Lee et al., “Dissipationless Anomalous Hall Current in the Ferromagnetic Spinel $CuCr_2Se_{4-x}Br_x$”, Science. 2004 Mar 12;303(5664):1647-9.
35. A. Fert et al., “Left-Right Asymmetry in the Scattering of Electrons by Magnetic Impurities, and a Hall Effect”, Phys. Rev. Lett. 28, 303 (1972)
36. T. Jungwirth et al., “Anomalous Hall effect in ferromagnetic semiconductors”, Phys Rev Lett. 2002 May 20;88(20):207208.
37. N. P. ONG et al., “Geometry and the Anomalous Hall Effect in Ferromagnets”.
38. Xinjie Wang et al., “Fermi-surface calculation of the anomalous Hall conductivity”, Phys. Rev. B 76, 195109 (2007)
39. Zhong Fang et al., “The Anomalous Hall Effect and Magnetic Monopoles in Momentum Space”, *Science* Vol. 302, Issue 5642, pp. 92-95 03 Oct 2003.

Chapter 4

Spin Polarized Current in Pt/YIG bilayers

4.1 Abstract

In this chapter, spin polarization is measured in Pt/Yttrium iron garnet(YIG) structures. The spin polarization is measured by the point contact Andreev reflection technique. Pt is nonmagnetic heavy metal which intrinsically has no spin polarization as is confirmed in my measurement in the SiO_2/Pt structure. Nonzero spin polarization is observed in YIG/Pt. Spin polarization can still be observed in Pt when a 1.2nm Cu is inserted between Pt and YIG. The induced spin polarization in Pt comes from the proximity effect at the interface and spin current pumping from YIG. Inserting 1.2nm NiO layer between Pt and YIG effectively blocks the spin polarization in Pt while 0.6 NiO insertion layer enhanced the spin polarization in Pt. The experiments demonstrated that the spin pumping plays a crucial role in the induced spin polarization in Pt. This spin pumping is further enhanced in the NiO layer through the magnons and spin fluctuations. This is further demonstrated by temperature dependent spin polarization measurements.

4.2 Introduction

Yttrium iron garnet(YIG) is a ferrimagnetic insulator which has magnetic type respond to external magnetic field but is not conducting. Study has

shown that by depositing a Pt layer next YIG, anomalous Hall effect kind signal can be detected in the Pt layer[1]. This signal is sensitive to the temperature and Pt thickness but cannot come directly from the YIG layer because of the insulating property of YIG. Th AHE even changes sign as temperature changes and this effect is suggested to be due to the spin mixing conductance at the interface between the two layers[1]. Another study has suggested that the magnetic property obtained by the Pt layer when made contact with the YIG layer is due to proximity effect[2]. There is a measurable magnetic moment induced in the Pt layer when grown on YIG and the proximity effect caused the modification of the electronic structure in the Pt layer[2]. There is no ferromagnetic character measurable in the Pt layer when it is grown on GGG substrate[2]. Study also argues that Pt being a nonmagnetic metal with very strong spin orbit coupling shows even greater magnetic proximity effect than Py when grown on YIG layer. The strength of the magnetic property induced on Pt decreases as increasing Pt thickness because of the spin diffusion in the Pt layer[3]. Study also suggests that the magnetic property of Pt on YIG comes not only from magnetic proximity effect but also from the spin current across the Pt/YIG interfaces. By inserting a thin Au layer between Pt and YIG, the contribution from the above two factors can be distinguished[4]. Study also found that single layer graphene grown on YIG has measurable anomalous Hall effect signal up to room temperature and the proximity effect between the YIG and graphene

layer enhanced the otherwise weak spin-orbit coupling of the graphene layer[7].

The above researches all show that the Pt being is a nonmagnetic metal, shows magnetic property when it is grown on YIG. In generally this acquired magnetic property comes from the ferrimagnetic YIG and is due to the magnetic proximity effect and the spin current injection. Intrinsically, Pt should have zero spin polarization, this raises the question: is the current in the Pt spin polarized when it is grown on YIG because of the proximity effect? Using our Andreev Reflection Spectroscopy equipment, we can measure the spin polarization of a nonsuperconductor effectively. In this chapter, I will study the spin polarization of the Pt/YIG related structure using ARS.

4.3 Experiment

The experiment is done in low temperature 4.2K when the superconducting Pb tip and Fe superconductor tip is in contact with the Pt thin film. The entire experiment process is the Andreev reflection spectroscopy as is described earlier.

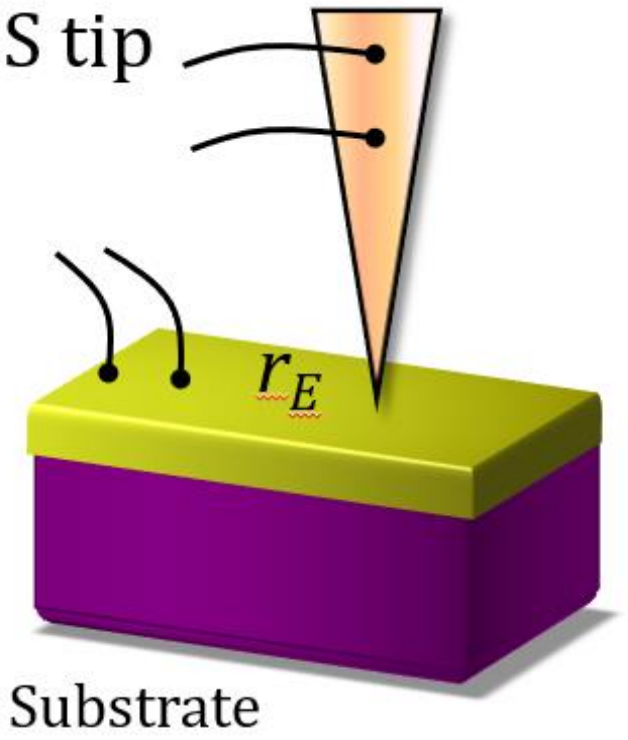

Figure 4.1: Schematic for the experiment.

4.3.1 Spin Polarization of Pt grown on YIG

The first structure measured is the 3nm of Pt layer directly grown on SiO_2 substrate. In this structure, we should expect a zero spin polarization because this is the intrinsic property of the Pt material.

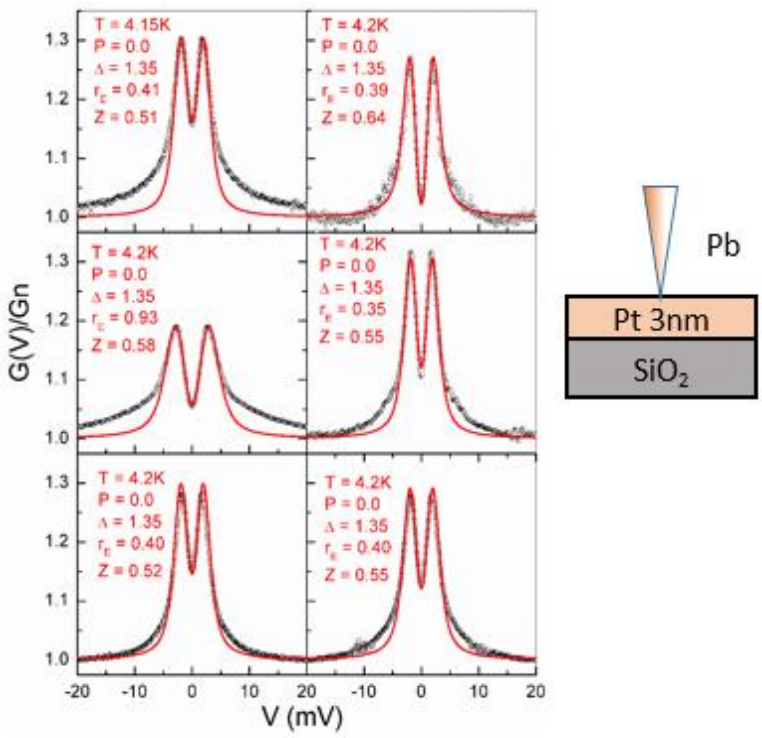

Figure 4.2: ARS curve for Si/SiO2/Pt(3nm).

There are several figures in the above graph, each corresponds to a different contact which has different Z factor. The Z factor is the proposed potential barrier at the interface between Pt and YIG and is simulated as a delta function. From the experimental result, we can see that the spin polarization of the of the 3nm Pt on SiO2 is always zero with multiple point contact. This demonstrates the assumption that the intrinsic spin polarization of a pure Pt layer is zero and also shows that our Pt sputtering target is clean and good. The later nonzero spin polarization measurement on the Pt surface is not the intrinsic property of the Pt layer.

The second experiment is about 3nm Pt grown on 50nm YIG film. The 50 nm YIG film is grown epitaxially on GGG substrate using Pulsed Laser

Deposition by Dr. Mingzhong Wu in Colorado State University. 3nm Pt is sputtered on YIG film in our lab using the magnetron sputtering method.

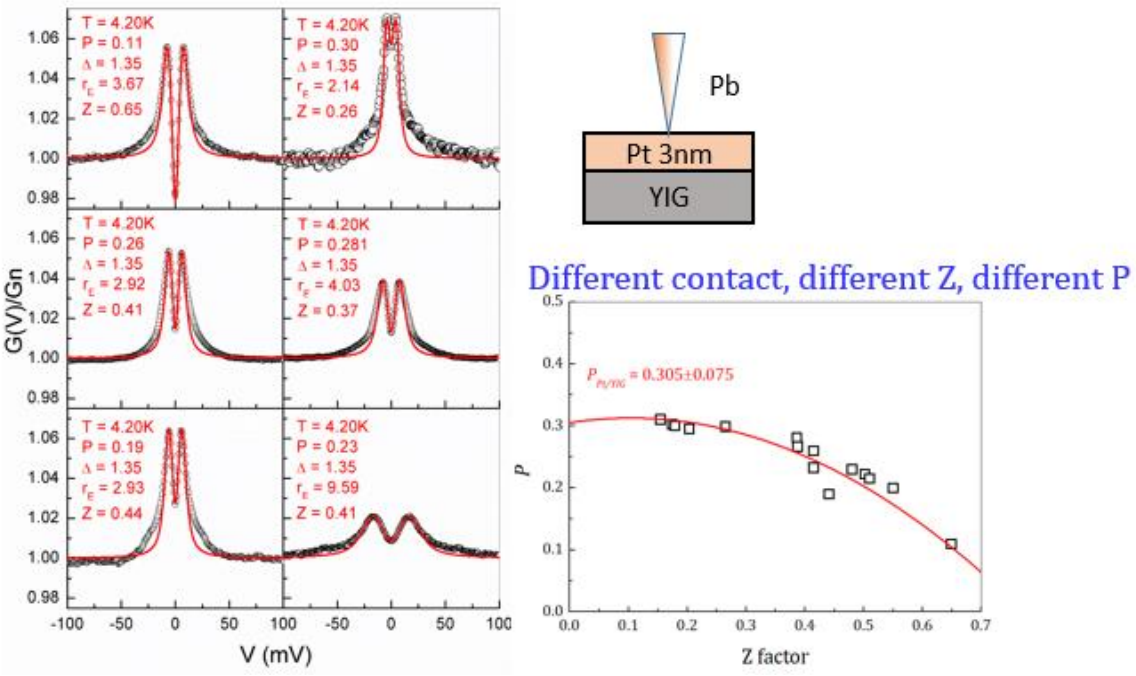

Figure 4.3: ARS curve for GGG/YIG(50nm)/Pt(3nm).

From the above data, we can see that the spin polarization P of the Pt film on YIG substrate is no longer zero. Different contact shows different spin polarization which corresponds to different Z factor, these are not the intrinsic spin polarization of the Pt on YIG. The different Z factor comes from the different tunneling barrier of different point contact. The spin polarization is plotted as a function of Z factor and by extrapolating the Z factor to zero, the intrinsic spin polarization is determined to be P=0.3. This nontrivial spin polarization is in contrast with the zero spin polarization of the Pt layer sputtered on SiO_2 alone. Studies have shown that the Pt layer shows magnetic property when it is grown on YIG due to the magnetic

proximity effect at the interface and the spin current pumping from YIG into Pt layer. Our result of the nonzero spin polarization P further demonstrates the assumptions from these studies.

Next, we studied the spin polarization of the Pt/YIG structure with different Pt thickness. We changed the Pt thickness from 3nm to 10nm.

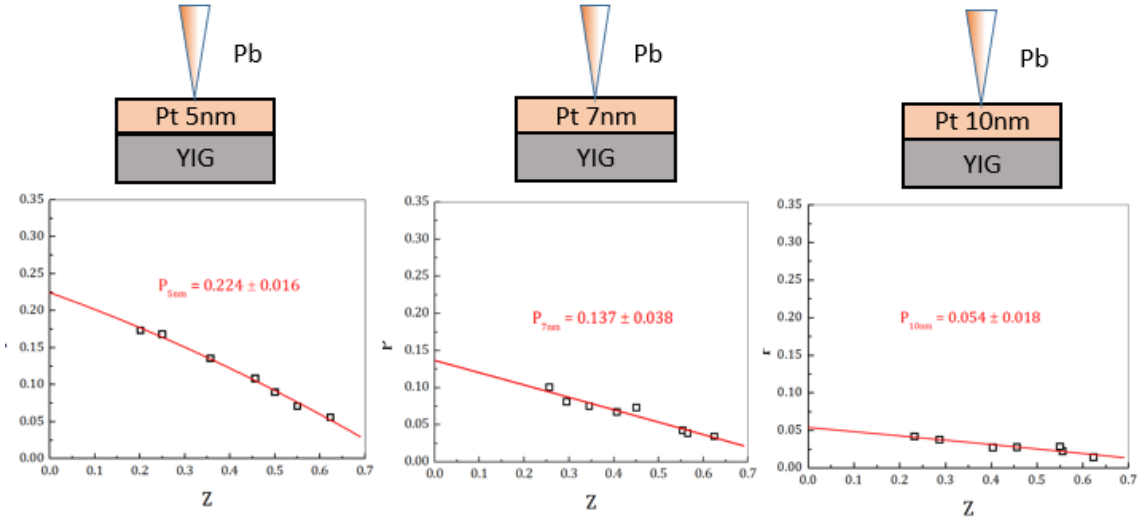

Figure 4.4: ARS curve for GGG/YIG(50nm)/Pt(5, 7, 10nm).

We can see from the above data that the spin polarization decreases with increasing Pt thickness. The spin polarization in the Pt layer is not uniform but is different depending on how far apart from the YIG/Pt interface. This result is the same as the other studies which show that the spin diffusion in the Pt layer will decrease the spin polarization as measured on the top surface of the Pt layer.

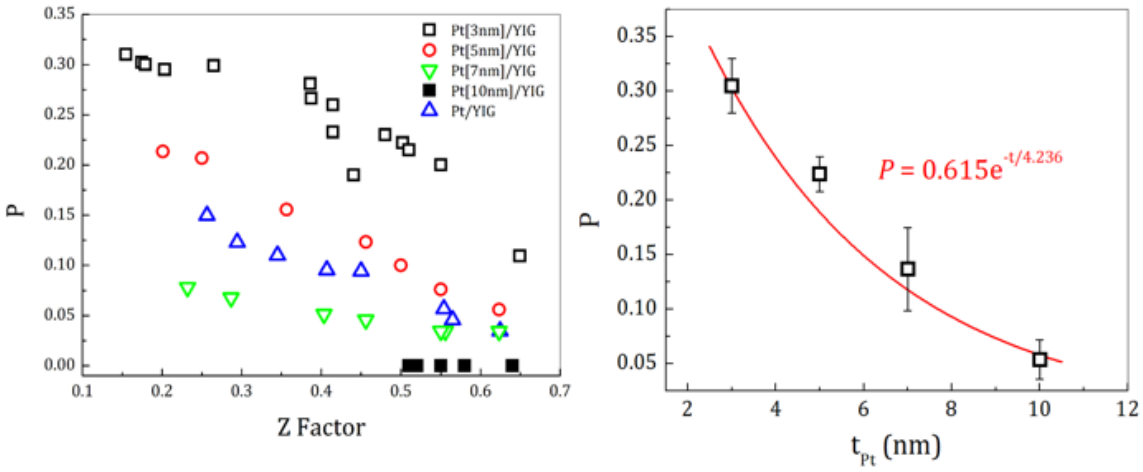

Figure 4.5: Spin polarization P vs Pt thickness curve.

The spin polarization P can be plotted as a function of the Pt thickness t. As can be seen from the graph, P decreases exponentially as Pt thickness increases which is as expected in the spin diffusion theory. By fitting the curve with exponential function, the spin diffusion length in the Pt layer can be determined as 4.236nm. All the measurements take place at 4.2K.

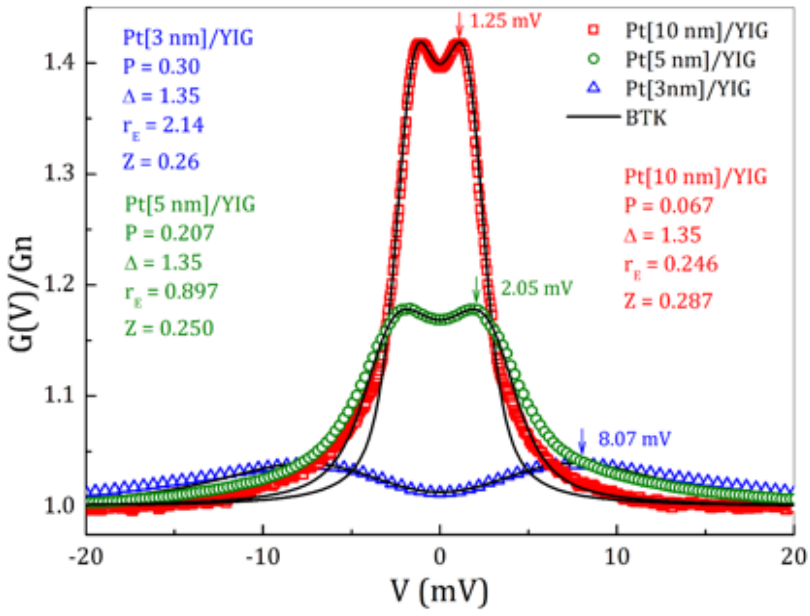

Figure 4.6: The effect of the large extra resistance in the Pt film on ARS curve.

In the ARS measurements, we made point contact on the Pt thin film. Thin film samples have large extra resistance as compared with bulk samples, this extra resistance is in series with the point contact ARS resistance and has the effect of broadening the ARS curve. During the curve fitting, this extra resistance must be taken into consider of. From the above data, we can see that with decreasing Pt thickness, the ARS curve becomes wider and the extra resistance is larger as can be extracted from the curve fitting.

4.3.2 Effect of Cu or NiO insertion layer between YIG and Pt

In the next series of experiments, I study the spin polarization of the Pt sample by inserting a thin Cu or NiO layer between the Pt and YIG layer.

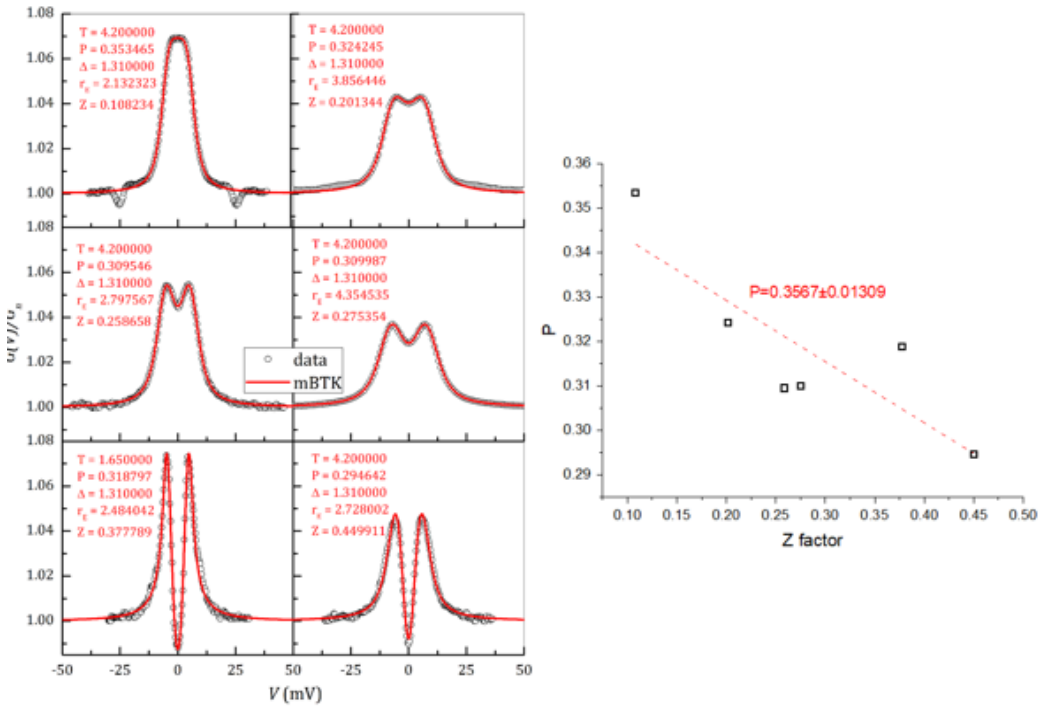

Figure 4.7: ARS curve for GGG/YIG(50nm)/Cu(1.2nm)/Pt(3nm).

The above graph is the spin polarization of the Pt layer when a 1.2nm Cu insertion layer is deposited between Pt layer and YIG layer. Cu is a diamagnetic metal with weak spin orbit coupling. From the data we can see that the intrinsic spin polarization of the Pt in this structure is 0.35 which is even higher than that in Pt directly grown on YIG. When there is a Cu layer between Pt and YIG, the Pt layer is not in direct contact with the YIG thus the proximity effect between YIG and Pt is effectively blocked. The even higher spin polarization in the Pt layer must originates from some other effect other than proximity effect. This acquired spin polarization must come from the spin current pumping. We can see that the spin current from YIG layer can transmit through the 1.2nm Cu insertion layer into the Pt layer. Spin current pumping from YIG into Pt layer can thus be studied by inserting different layers with various thickness between YIG and Pt.

In the next step, thin NiO layer is inserted between 3nm Pt layer and the YIG layer. NiO is a antiferromagnetic insulator with a Neel temperature above room temperature[8]. This NiO is antiferromagnetic during the experiment which is conducted in liquid helium temperature.

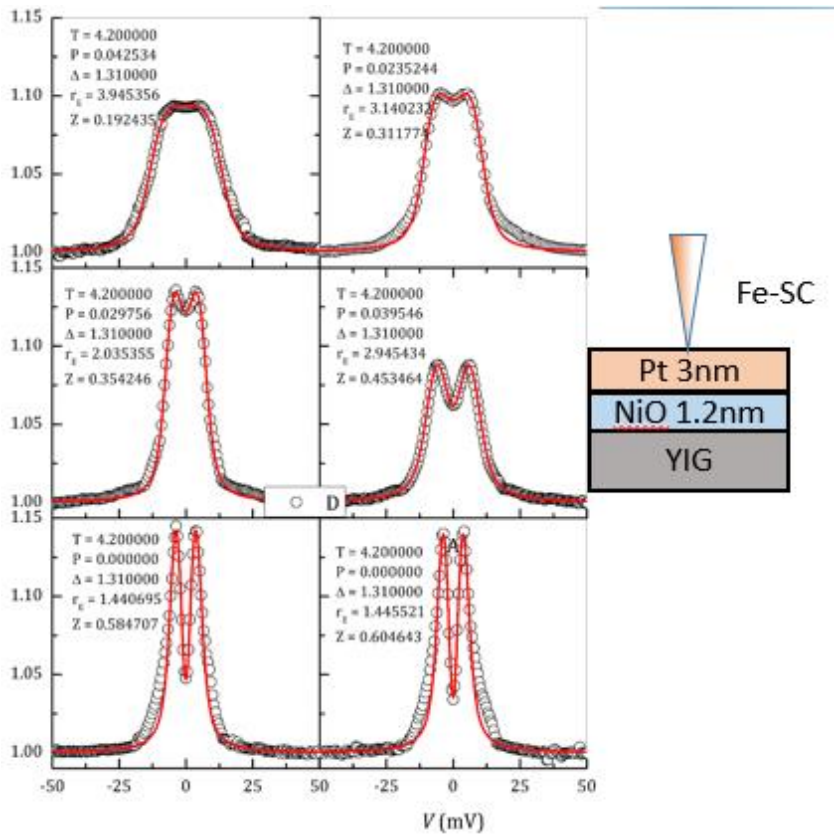

Figure 4.8: ARS curve for GGG/YIG(50nm)/NiO(1.2nm)/Pt(3nm).

The above data is the 3nm Pt and YIG inserted by 1.2nm of NiO layer. We can see that from inserting 1.2nm of NiO between the Pt and YIG, spin polarization measurement is zero with multiple contacts of different Z factor. This means that the Pt layer is well insulated from the YIG layer by the NiO inserting layer. The Pt layer returns its intrinsic nonmagnetic character and does not show magnetic property any longer. From our assumption, the proximity effect as well as the spin current are effectively blocked by the 1.2nm NiO layer.

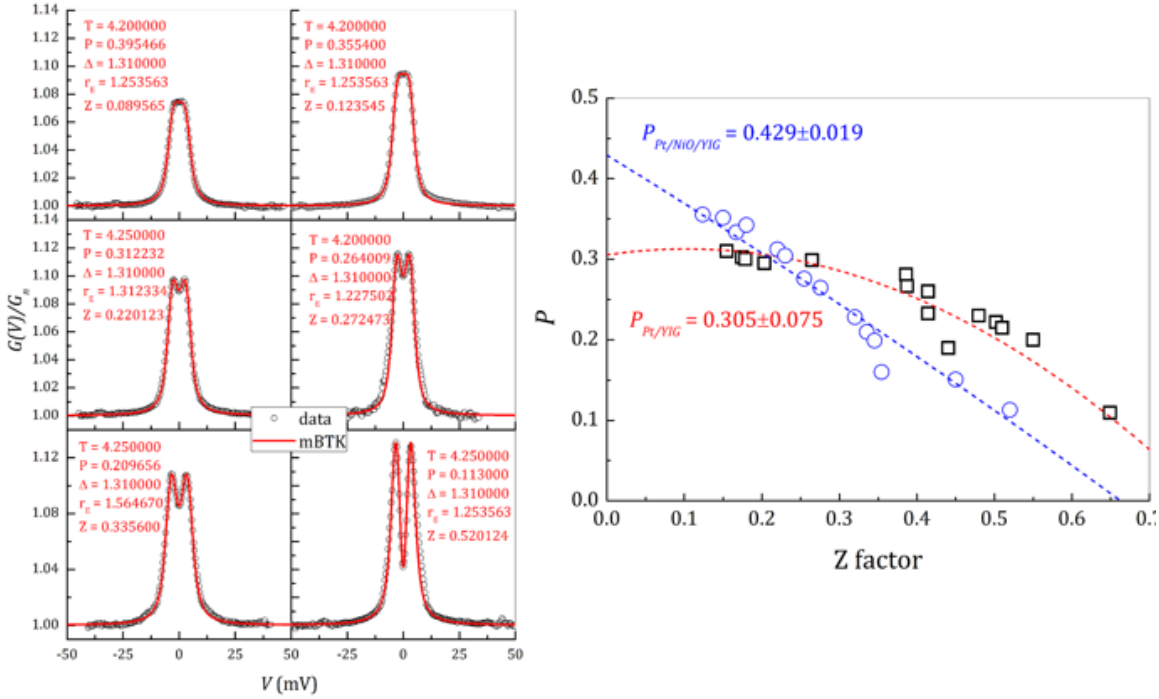

Figure 4.9: ARS curve for GGG/YIG(50nm)/NiO(0.6nm)/Pt(3nm).

The above data is the spin polarization of the 3nm Pt and YIG layer separated by a 0.6nm NiO layer. The reducing of the NiO layer thickness from 1.2nm to 0.6nm greatly impacts the spin polarization of the Pt layer. As can be seen from the graph, not only this structure shows spin polarization, the spin polarization is even higher than the 3nm Pt grown directly on YIG. The dependence of the spin polarization on Z factor shows a linear relationship which is different from the nonlinear relationship in the 3nm Pt grown directly on YIG structure. Because there is an ultrathin 0.6nm NiO layer between Pt and YIG, the spin polarization induced in the Pt layer should not be explained by the proximity effect. There are researches done on NiO insertion layer between Pt and YIG which claim that the spin current

is injected from YIG to Pt layer and the spin current injection can be greatly enhanced by the thin NiO inserted layer[10][11]. Although the antiferromagnetic NiO is insulating and does not show magnetic character macroscopically, the antiparallel spins in NiO is still ordered microscopically and can be excited as magnons and transmit spin wave. This spin current enhancement is due to the magnons and spin fluctuations in the ultrathin NiO antiferromagnetic layer[10]. Because the enhancement is magnon and spin fluctuation based, the strength of the enhancement depends on temperature and is maximized near the Neel temperature of the NiO layer when the most magnons are excited in the layer[10]. This effect is corroborated by theoretical calculations[12]. This magnon excitation and fluctuation in antiferromagnetic insulators is not only observed in NiO but also in Ni_2NbBO_6 which shows pronounced spin-phonon interactions and phonon excitations below and slightly above the Neel temperature and is strongly temperature dependent[13].

We have seen from the previous study that the ultrathin NiO layer might enhance the spin current from the YIG layer and induce strong magnetic property in the Pt layer. This might explain the larger spin polarization in the Pt layer of the YIG/NiO(0.6nm)/Pt structure. We have also seen there is strong temperature dependence in this effect[10]. In the last experiment, I replaced the Pb superconducting tip by the Fe superconducting tip which

remains in the superconducting state up to 50K. In this way, we can measure the temperature dependence of the spin polarization of the sample.

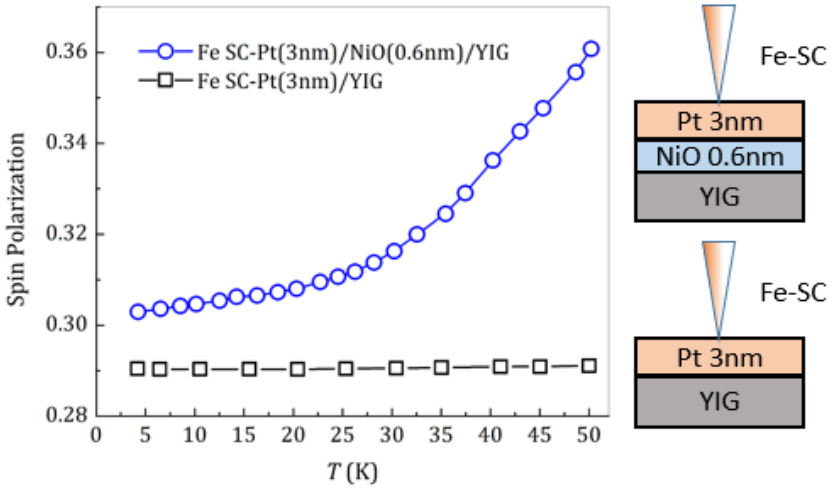

Figure 4.10: Temperature dependence of the spin polarization in YIG/NiO(0.6nm)/Pt(3nm) and YIG/Pt(3nm).

As can be seen from the data, the spin polarization of the YIG/NiO(0.6nm)/Pt(3nm) sample increases with increasing temperature while the spin polarization of the YIG/Pt(3nm) sample remains the same. Previous studies have claimed that the strong temperature dependence of the magnon and spin excitation in the antiferromagnetic layer and claim that it is strongest near the Neel temperature[10]. The higher the magnon excitation in the NiO insertion layer, the higher the spin current transmission. The increased spin polarization indicates increased spin current transmission into the Pt layer. Our measurement temperature is well below the Neel temperature of the NiO so the increase of the spin

polarization with increasing temperature is as expected which is in agreement with the previous study.

4.4 Conclusion

In conclusion, we have observed induced nontrivial spin polarization in the Pt layer when it is grown next a ferrimagnetic insulator YIG film. The induced spin polarization comes from the magnetic proximity effect at the interface between the Pt layer and the YIG layer and can also due to the spin current flow from the YIG layer into the Pt layer. By inserting a Cu or NiO layer between the Pt and YIG, we effectively prevented the proximity effect from contributing to the spin polarization in the Pt sample. For sample with Cu insertion and ultrathin NiO(0.6nm) insertion, the spin polarization in the Pt layer is even stronger than the sample directly grown on YIG, this result might indicate that the spin current injection plays a crucial role in the magnetic property induced in the Pt layer. The spin current injection is even enhanced by the ultrathin NiO layer due to magnon and spin fluctuation in the NiO layer and this enhancement is highly temperature dependent which is maximized near the Neel temperature of the antiferromagnet.

REFERENCE

1. Sibylle. Meyer et al., “Anomalous Hall effect in YIG | Pt bilayers”, Appl. Phys. Lett. 106, 132402 (2015).

2. Y. M. Lu et al., “Pt Magnetic Polarization on $Y_3Fe_5O_{12}$ and Magnetotransport Characteristics”, PRL 110, 147207 (2013).
3. S. Y. Huang et al., “Transport Magnetic Proximity Effects in Platinum”, PRL 109, 107204 (2012).
4. B. F. Miao et al., “Physical Origins of the New Magnetoresistance in Pt/YIG”, PRL 112, 236601 (2014).
5. H. Nakayama et al., “Spin Hall Magnetoresistance Induced by a Nonequilibrium Proximity Effect”, PRL 110, 206601 (2013).
6. B. Heinrich et al., “Spin Pumping at the Magnetic Insulator (YIG)/Normal Metal (Au) Interfaces”, PRL 107, 066604 (2011).
7. Zhiyong Wang et al., “Proximity-Induced Ferromagnetism in Graphene Revealed by the Anomalous Hall Effect”, PRL 114, 016603 (2015).
8. Natalia Rinaldi-Montes et al., “Size effects on the Néel temperature of antiferromagnetic NiO nanoparticles”, AIP Advances 6, 056104 (2016).
9. Yu Wang et al., “Voltage-Controlled Sensitivity of the Spin Seebeck Effect in $Pt/Y_3Fe_5O_{12}/MgO/(PbMg_{1/3}Nb_{2/3}O_3)_{0.7}(PbTiO_3)_{0.3}$ Multiferroic Heterostructures”, PHYSICAL REVIEW APPLIED 10, 014004 (2018).
10. Weiwei Lin et al., “Enhancement of Thermally Injected Spin Current through an Antiferromagnetic Insulator”, PRL 116, 186601 (2016).
11. Weiwei Lin et al., “Electrical Detection of Spin Backflow from an Antiferromagnetic Insulator/$Y_3Fe_5O_{12}$ Interface”, PRL 118, 067202 (2017).

12. Kai Chen et al., “Temperature dependence of angular momentum transport across interfaces”, PHYSICAL REVIEW B 94, 054413 (2016).
13. M. A. Prosnikov et al., “Magnetic dynamics and spin-phonon coupling in the antiferromagnet Ni_2NbBO_6”, PHYSICAL REVIEW B 98, 104404 (2018).
14. L. Wang et al., “Co1-xFexS2: A Tunable Source of Highly Spin-Polarized Electrons”, PRL 94, 056602 (2005).
15. T. Y. Chen et al., “Enhanced Curie temperature and spin polarization in Mn4FeGe3”, Appl. Phys. Lett. 91, 142505 (2007).
16. S. X. Huang et al., “Spin polarization of amorphous CoFeB determined by point-contact Andreev reflection”, Appl. Phys. Lett. 92, 242509 (2008).
17. T. Y. Chen et al., “Determination of superconducting gap of $SmFeAsF_xO_{1-x}$ superconductors by Andreev reflection spectroscopy”, Physica C: Superconductivity, Volume 469, Issues 9–12 (2009).
18. T. Y. Chen et al., “Pronounced effects of additional resistance in Andreev reflection spectroscopy”, Phys. Rev. B 81, 214444 (2010).
19. Shashi K. Upadhyay et al., “Probing Ferromagnets with Andreev Reflection”, Phys. Rev. Lett. 81, 3247 (1998)

Chapter 5

Perpendicular Anisotropy in Ru/Co/Ru Trilayer

5.1 Abstract

In this chapter, the perpendicular magnetic anisotropy(PMA) in Ru/Co/Ru based trilayer structure is studied by anomalous Hall effect. The PMA depends sensitively on the thickness of the Co layer as well as the Ru base and capping layers. The PMA is retained in the Ru/[Co/Ru]×n multilayers with n up to 6. The Andreev reflection spectroscopy(ARS) can sensitively measure the spin orbit field in the ferromagnetic-superconductor junction. In this research, the ARS is used as a means to study the origin of the PMA in the Ru/Co/Ru structures. PMA in magnetic multilayers can originate from the spin orbit coupling at the interface as well as the strain due to lattice mismatch. If the PMA is due to spin orbit coupling, a giant magnetoanisotropy in ARS conductance should be observed when changing the magnetic field orientation from in plane to out of plane. In my measurement, no pronounced change in ARS is observed suggesting that the PMA in the Ru/Co/Ru structure originates from the lattice strain.

5.2 Introduction

5.2.1 Magnetic Domains

Ferromagnetism originates from the exchange energy between the magnetic moments inside the material. The exchange energy favors parallel orientation of the magnetic moments and becomes minimum when the moments are aligned parallel with one another. However, if all the magnetic moments align parallel inside the magnetic material, there will be a large amount of north and south poles accumulate on the opposite sides of the material a large amount of magnetic stray field will come out of one side of the material and go back to the other side. This will create a huge amount of magnetic static energy. In fact, the magnetic moment inside a material always align such that the total magnetic static energy is minimized, therefore magnetic domains form inside the material.

The magnetic moments inside a material typically break down into domains. Each domain typically is of micron size and the magnetic moments align perfectly parallel inside each domain. The magnetization between different domains are not parallel with each other therefore domain walls will form between the border of neighboring domains. The domain wall formation will increase the domain energy because there is magnetization switching in the domain wall region and the domain wall energy comes from the exchange energy of antiparallel magnetic moments. Because the increase

in the energy due to domain wall formation is less than the decrease in magnetic stray field energy therefore the domains will generally form inside the magnetic materials.

Because of the domain wall formation and motion, the magnetization of magnetic materials responses to external field is hysteresis curve. When the external magnetic field is strong enough, all magnetic moments in the materials is pulled toward the external field direction and no domain forms inside the material in this situation. This is called saturation magnetization. The saturation magnetization is the intrinsic property of a particular material because theoretically it can be calculated based on how much magnetism is in one atom and how many atoms are in a unit cell and the lattice structure. When there is no external magnetic field, domains form inside the material to lower the overall magnetic energy of the system. Because not all domains magnetize in the same direction, the overall magnetization is smaller than the saturation magnetization and is called remnant magnetization. The magnetic field required to achieve the zero magnetization of the material is call the coercivity. The remnant magnetization and the coercivity depends critically on the size and shape of the material and is closely related to the anisotropy of the particular sample. They are not intrinsic property of the material.

5.2.2 Magnetic Anisotropy

The magnetic Anisotropy is the tendency of a magnetic material to magnetize in a particular orientation. There are certain mechanisms that contributes to magnetic anisotropy namely magnetocrystalline anisotropy, shape anisotropy and magnetoelastic anisotropy. One can define the the magnetic anisotropy constant K which is the energy required to pull the magnetic moment away from the preferred orientation[1-3].

The magnetocrystalline anisotropy is due to the crystal structure of the material. Different materials can have different crystalline structure which lead to different magnetic anisotropy. Let's take for example Fe, Ni and Co. The Iron single crystal has bcc cubic structure and Ni has fcc cubic structure. The easy magnetization axis of the Fe is in the [100] directions which means that the magnetic moments of Fe tend to align along the edges of the cubic. The easy axis in the Ni is along the [100] direction which means that the easy axis prefers the diagonal direction of the cubic structure. The Co single crystal has hexagonal structure and the magnetic easy axis is along the c-axis of the hexagonal structure. According to crystal symmetry, the [100] has 6 equivalent directions and [111] has 8 equivalent directions which the c-axis in the hexagonal structure has only 2 equivalent directions. Therefore the domains in the Fe single crystal can point to 6 directions and that in Ni can point to 8 directions while the domains in single crystal Co can only point to 2 directions[1-3].

The anisotropy energy can be written as a function of magnetization directions. For cubic structure such as Fe and Ni, the anisotropy energy can be written as:

$$u_a = K_0 + K_1(\alpha_1^2\alpha_2^2 + \alpha_2^2\alpha_3^2 + \alpha_3^2\alpha_1^2) + K_2(\alpha_1^2\alpha_2^2\alpha_3^2) + \cdots \quad [4.1]$$

The term α_i is the cosine of the angle between the particular axis and the direction of the magnetization where i can be x, y or z. The term K_1 can actually determine the magnetic anisotropy direction in cubic lattice structure. For Fe, the term K_1>0, u_a is minimized when magnetization is in the [100] direction which means that the Fe crystal has [100] anisotropy. For Ni, the term K_1<0, u_a is minimized when magnetization is in [111] direction thus comes the [111] anisotropy for the Ni crystal.

For hexagonal structure, the anisotropy energy as a function of the magnetization direction can be written as:

$$u_a(\theta) = K_{u0} + K_{u1}sin^2(\theta) + K_{u2}sin^4(\theta) \quad [4.2]$$

The term K_{u1} actually determines the magnetic anisotropy in hexagonal structure. If K_{u1}>0 as is the case for Co, c-axis is the easy axis and it is called uniaxial anisotropy. If K_{u1}<0, c-axis is the hard axis.

The physical mechanisms behind crystalline anisotropy is the spin orbit coupling between the magnetic moments and the crystal bonding of the lattices. As a result, the magnetization of the material shows the same symmetry as the crystal lattice of the material[1-3].

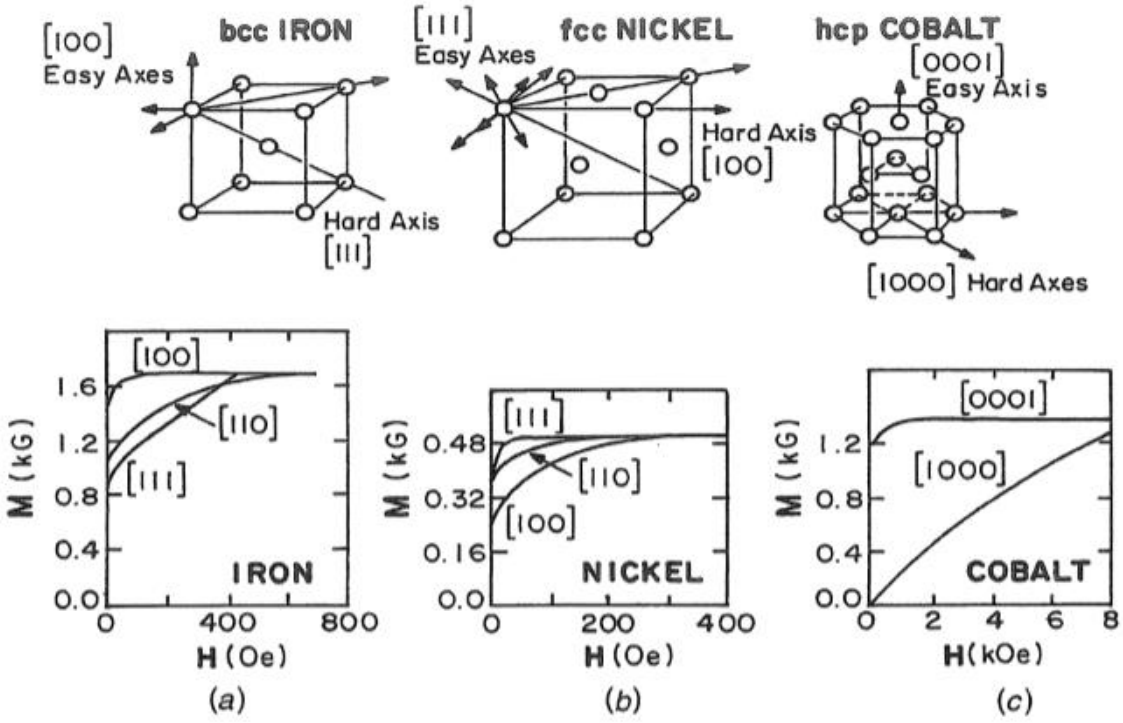

Figure 5.1: The crystalline anisotropy of (a)Fe, (b)Ni and (c)Co[1].

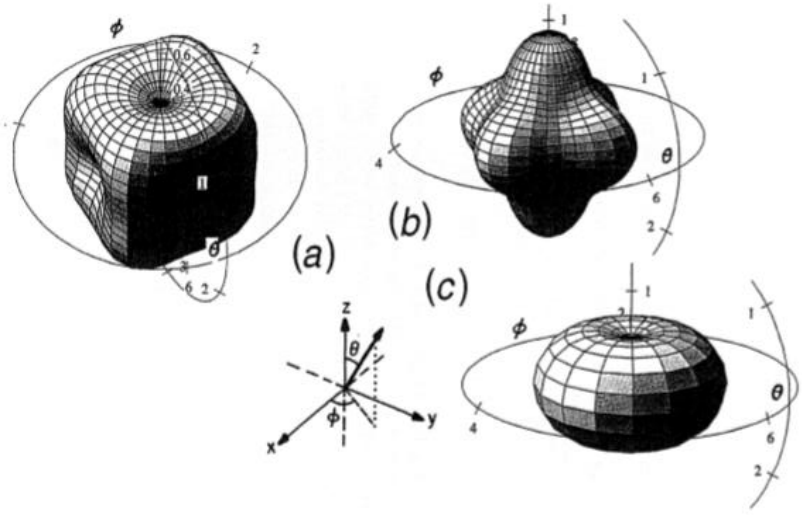

Figure 5.2: First order magnetic anisotropy energy surface for (a)Fe, (b)Ni and (c)Co[1].

The shape anisotropy is the preferred magnetization direction based on the shape of the material, this is also because of the minimization of the overall magnetic static energy the material produces. The basic rule is that elongated material tends to magnetize along the long axis to minimize the energy of the stray field produced by the material. For the thin film sample, the out of plane dimension is so much smaller than the in plane dimension so that in plane anisotropy is always observed. Perpendicular magnetic anisotropy(PMA) of thin film samples are always caused by special mechanism[1].

5.3 Experiment and Conclusion

In this chapter, I show the result of experiments about the Perpendicular anisotropy in the Ru/Co/Ru trilayer structures. Co based perpendicular anisotropy has been extensively studied in Co/Ni, Co/Pd and Co/Pt multilayers etc. [5-15].

The PMA in Co/Pt and Co/Pd multilayers is said to originate from the hybridation of the 3d Co orbitals and 5d Pt and 4d Pd orbitals and together with the strong spin orbit coupling in the Pt layer[5]. This creates a spitting in the in plane and out of plane orbitals in the Co layer and the out of plane orbital is favored because of the lower energy[6][20].

For the PMA in Co/Ru layers, there are researches conducted suggest that the PMA originates from the lattice strain due to the lattice mismatch between the Co and Ru layer[7].

5.2.1 PMA in Ru/Co/Ru Structure

In this section, we will study the Ru/Co/Ru structure which has the PMA.

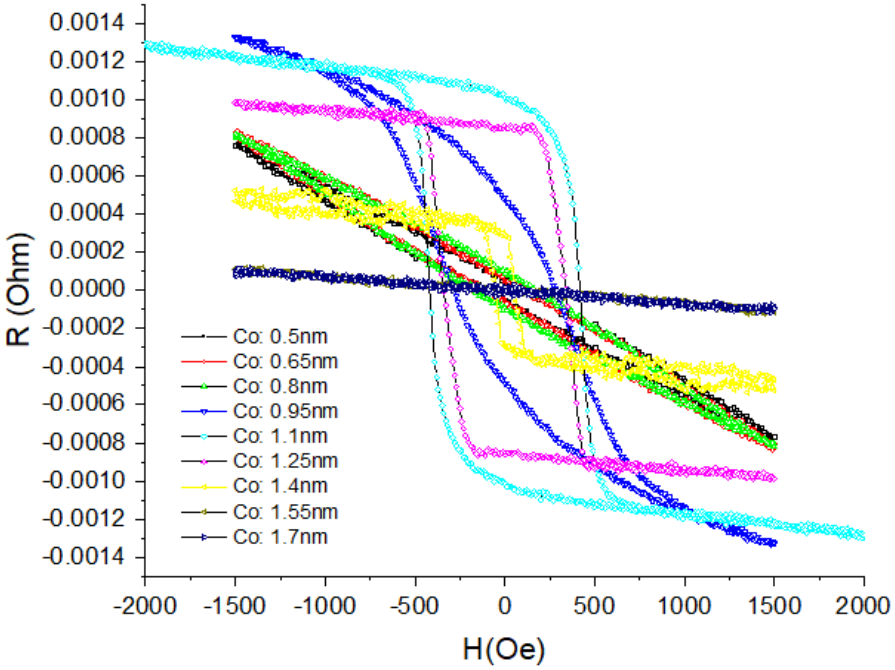

Figure 5.3: AHE signal of Si/SiO2/Ru(15nm)/Co(0.5-1.7nm)/Ru(3nm) trilayer structure as measured by probe station.

The above graph is the AHE signal of the Si/SiO2/Ru(15nm)/Co(0.5-1.7nm)/Ru(3nm) trilayer structure as measured by probe station. As can be seen from the graph, the PMA of the structure gradually appear and disappear as Co thickness increases. The PMA only appear in sample with a

Co thickness of 1.25nm and is very sensitive on the thickness of the Co layer. We can also see that the magnitude of the AHE signal in this structure is in the milliohm level which is much smaller than in the MgO/Py/HM based structures. The magnitude of the AHE signal first increases and decreases as Co thickness increases and is maximized at around 1.2nm, this is also when PMA is observed in the sample.

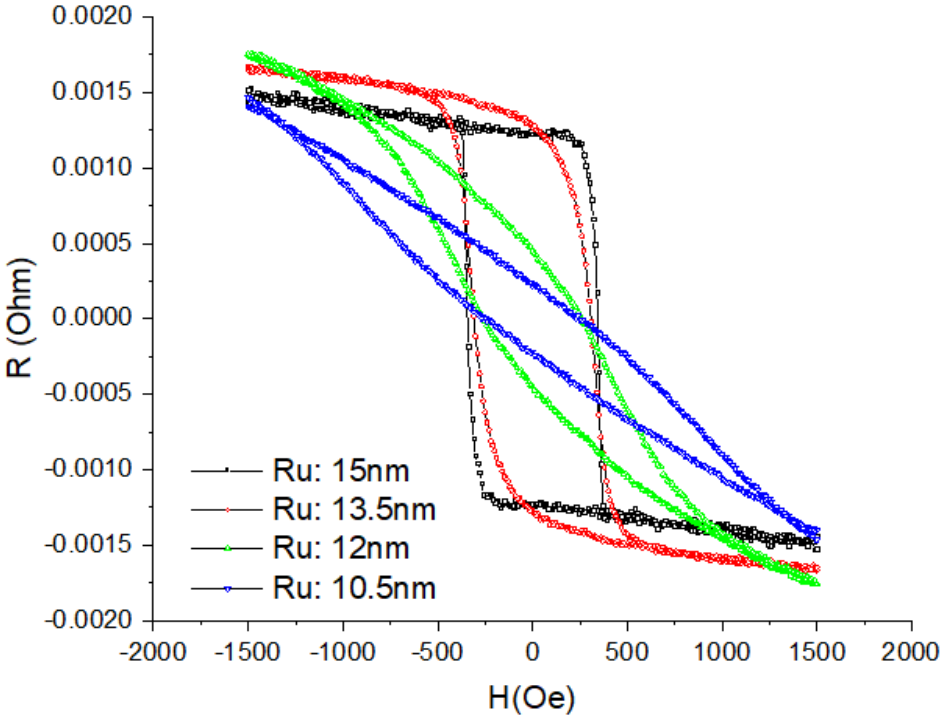

Figure 5.4: AHE signal of Si/SiO2/Ru(10-15nm)/Co(1.25nm)/Ru(3nm) trilayer structure as measured by probe station.

The above graph is the Ru base layer thickness dependence of the PMA property of the sample as measured by probe station. As can be seen from the graph, base layer plays a crucial role in the magnetic anisotropy of the

sample. The PMA is only observed in 15nm based Ru samples and PMA disappears when the Ru base layer is reduced.

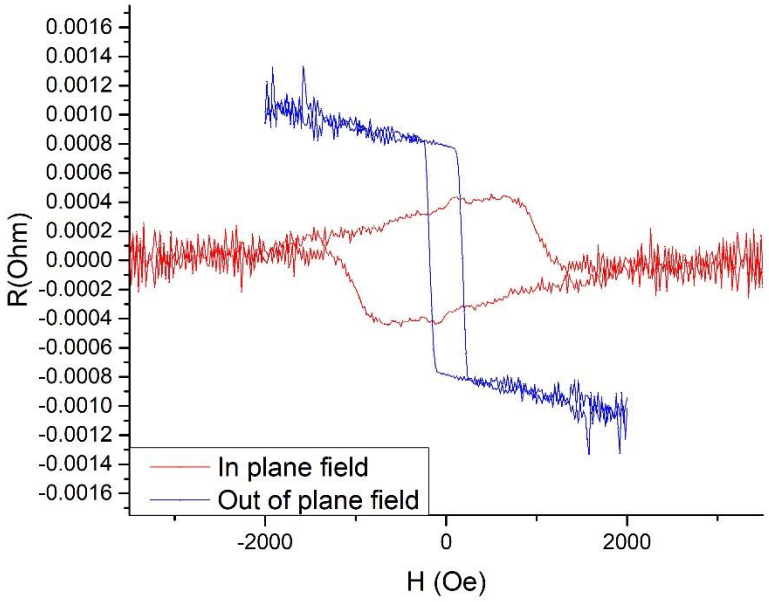

Figure 5.5: Angular dependence of the AHE signal of Si/SiO2/Ru(15nm)/Co(1.25nm)/Ru(3nm) structure.

The angular dependence of the AHE signal is also measured in the sample which shows the best PMA. In the measurement, the current is applied horizontally in the sample and the magnetic field is rotated horizontally to get the angular dependence. We can see that when the field is applied perpendicular to the sample the AHE shows sharp transition which corresponds to the sharp magnetic switching. When the field is applied in plane, the curve is more rounded broadened which shows that the anisotropy is indeed out of the plane of the sample.

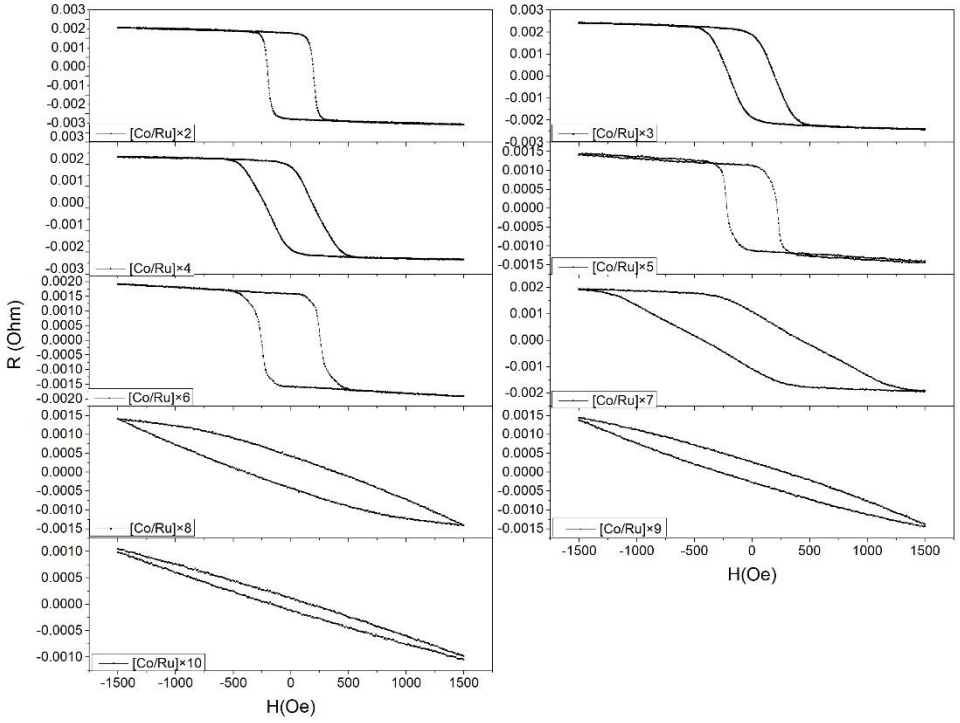

Figure 5.6: AHE signal of the multilayer

Si/SiO2/Ru(15nm)/[Co(1.25nm)/Ru(3nm)]n n=2-10.

The above graph is the AHE signal for the Si/SiO2/Ru(15nm)/[Co(1.25nm)/Ru(3nm)]n n=2-10 structure. We can see that with increasing number of repetition layers, the PMA gradually disappears. The maximum number of repetition in which we can still have PMA is n=6. Also, the structure shows of oscillating behavior in the PMA. The PMA in the n=6 sample seems to be higher than that in n=2, 3 sample.

5.2.2 Magnetic Field Angular dependence of Spin Polarization

We also measured the ARS curve for the Si/SiO2/Ru(15nm)/Co(1.25nm)/Ru(3nm) structure. We can see that the spin polarization is about 0.491 so the sample is spin polarized. The spin polarization in the sample should originate from the Co magnetic layer.

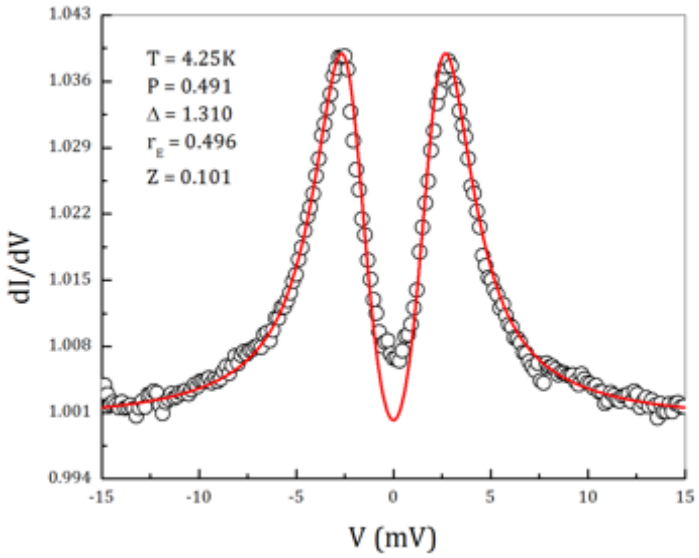

Figure 5.7: ARS curve for the Si/SiO2/Ru(15nm)/Co(1.25nm)/Ru(3nm) structure.

Because the Andreev reflection spectroscopy can be used to sensitively determine the spin-orbit field in a ferromagnetic-superconductor junction[18] which exhibits giant magnetoanisotropic change in conductance curve with different magnetic field orientation. I also measured the angular dependence of the external magnetic field on the Andreev Reflection Spectroscopy curve. There are two superconducting magnets in the Andreev Reflection Spectroscopy chamber, one can produce magnetic field in the horizontal direction and another in the vertical direction. During the measurement, the

magnetic field produced by the horizontal magnet and vertical magnet are controlled such that the total magnetic field equals 2000Oe and sweeps a circle in a vertical plane. The sample is mounted such that the surface of the sample is perpendicular to the field of the horizontal magnet. From Figure 5.8 we can see that the differential conductance curve does not change with different magnetic field direction which means that the perpendicular magnetic anisotropy in the Ru/Co/Ru trilayer structure originates from the strain due to lattice mismatch and not from the spin orbit coupling.

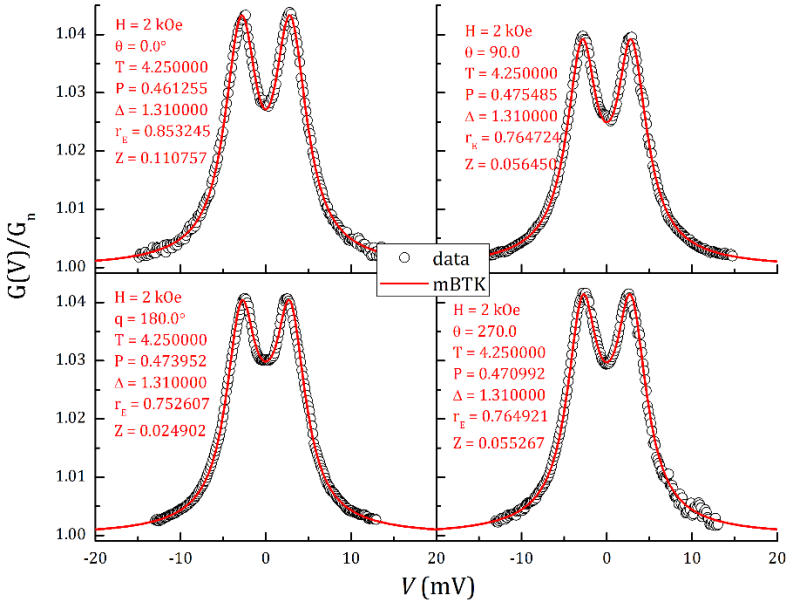

Figure 5.8: Angular magnetic field dependence of the ARS measurement.

5.4 Conclusion

In this chapter, the perpendicular magnetic anisotropy(PMA) of the Ru/Co/Ru trilayer structure is studied. I found that PMA can be obtained in the Ru/Co/Ru structure and the PMA property depends sensitively on the

thickness of the Co layer as well as the Ru base and capping layer. The PMA is observed in only a small range of the Co thickness of about 1.25nm, thinner or thicker Co layer will both make the PMA property disappear. The Ru base layer thickness of 15nm and a Ru capping layer is also required for the structure to possess PMA. I also found that the PMA in the Ru/Co/Ru structure is not as strong as that in the Co/Pt multilayers and MgO/CoFeB/Ta structure because the PMA gradually disappears after the sample is left in the lab months after deposition.

There are several mechanisms for a thin film structure to possess PMA such as the interfacial spin orbit coupling and the strain induced by lattice mismatch. In order to find out the possible reason for the PMA observed, I measured the sample using Andreev Reflection Spectroscopy(ARS). The ARS can be utilized to sensitively probe the spin orbit field in a superconductor ferromagnetic metal junction by changing the magnetization direction of the ferromagnetic and measuring ARS[18]. The ARS curve and spin polarization would change by varying magnetization direction of the sample. In my measurement, no change of ARS curve and spin polarization is observed in the magnetic field dependent measurement thus indicating that the PMA in the Ru/Co/Ru structure is due to the strain from lattice mismatch not from interfacial spin orbit coupling.

REFERENCE

1. Robert C. O'handley, "Modern Magnetic Materials: Principles and Applications."
2. David Jiles, "Introduction to Magnetism and Magnetic Materials".
3. B. D. Cullity et al., "Introduction to Magnetic Materials".
4. Soshin Chikazumi, "Physics of Ferromagnetism".
5. N. Nakajima et al., "Perpendicular Magnetic Anisotropy Caused by Interfacial Hybridization via Enhanced Orbital Moment in Co/Pt Multilayers: Magnetic Circular X-Ray Dichroism Study", Phys. Rev. Lett. 81, 5229 (1998).
6. D. Weller et al., "Orbital magnetic moments of Co in multilayers with perpendicular magnetic anisotropy", Phys. Rev. B 49, 12888 (1994).
7. Alexander G Kolesnikov et al., "Enhancement of perpendicular magnetic anisotropy and coercivity in ultrathin Ru/Co/Ru films through the buffer layer engineering", J. Phys. D: Appl. Phys. 49 (2016).
8. K. Ounadjela et al., "Perpendicular anisotropy and antiferromagnetic coupling in Co/Ru strained superlattices", Phys. Rev. B 45, 7768 (1992).
9. Z. Zhang et al., "Angular dependence of ferromagnetic resonance in exchange-coupled Co/Ru/Co trilayer structures", Phys. Rev. B 50, 6094 (1994).

10. P. J. H. Bloemen et al., “Oscillatory interlayer exchange coupling in Co/Ru multilayers and bilayers”, Phys. Rev. B 50, 13505 (1994).
11. Bharati Tudu et al., “Effect of Composition and Thickness on the Perpendicular Magnetic Anisotropy of (Co/Pd) Multilayers”, Sensors (Basel). 2017 Dec; 17(12): 2743.
12. Ja-Bin Lee et al., “Thermally robust perpendicular Co/Pd-based synthetic antiferromagnetic coupling enabled by a W capping or buffer layer”, Scientific Reports volume6, Article number: 21324 (2016).
13. T. Kato et al., “Perpendicular Anisotropy and Gilbert Damping in Sputtered Co/Pd Multilayers”, IEEE TRANSACTIONS ON MAGNETICS, VOL. 48, NO. 11, NOVEMBER 2012.
14. Enlong Liu et al, “Seed Layer Impact on Structural and Magnetic Properties of [Co/Ni] Multilayers with Perpendicular Magnetic Anisotropy”, Journal of Applied Physics 121, 043905 (2017).
15. M. Arora et al., “Origin of perpendicular magnetic anisotropy in Co/Ni multilayers”, Phys. Rev. B 96, 024401 (2017).
16. Bernd Zimmermann et al., “Anisotropy of Spin Relaxation in Metals”, PRL 109, 236603 (2012).
17. Bernd Zimmermann et al., “Fermi surfaces, spin-mixing parameter, and colossal anisotropy of spin relaxation in transition metals from ab initio theory”, PHYSICAL REVIEW B 93, 144403 (2016).

18. Petra Högl et al., “Magnetoanisotropic Andreev Reflection in Ferromagnet-Superconductor Junctions”, PRL 115, 116601 (2015).
19. Shashi K. Upadhyay et al., “Probing Ferromagnets with Andreev Reflection”, Phys. Rev. Lett. 81, 3247 (1998)
20. Jun Okabayashi et al., “Anatomy of interfacial spin-orbit coupling in Co/Pd multilayers using X-ray magnetic circular dichroism and first-principles calculations”, Scientific Reportsvolume 8, Article number: 8303 (2018)

Chapter 6

Summary and Future Work

6.1 Summary of Previous Works

In this thesis, I have worked on three major parts. The first part is the sign change of anomalous Hall effect in MgO/Py/HM based magnetic trilayer thin films. The second part is the nonzero spin polarization induced in Pt in YIG/Pt based thin film structures. The last part is perpendicular magnetic anisotropy induced in Ru/Co/Ru trilayer systems and its origin as studied by Andreev reflection spectroscopy.

In the first part, anomalous Hall effect is studied in MgO/Py/HM structures as is measured by 4 point contact magnetic transport measurement. It was found that the sign of the anomalous Hall effect changes when a certain HM is used as the top capping layer. In MgO(2nm)/Py(1.6nm)/Ta(0-4nm) structures the sign of the AHE changes from negative to positive as Ta capping layer thickness increases. The transition from negative to positive occurs at when Ta is about 2nm, at this Ta thickness, the AHE curve is almost a flat line on the x axis. The magnitude of the AHE stopped increasing as the Ta thickness is beyond

3~4nm. The MgO underlayer is crucial for the sign change in the MgO/Py/Ta structure as the sign of the AHE does not change without MgO under layer even if the thickness of the tantalum increases up to 8nm. Merely adding 1nm of MgO under the Py layer will change the sign of the AHE in the MgO/Py(1.6nm)/Ta(4nm) structure and the magnitude of the AHE does not increase after the MgO under layer is above 2nm suggesting that the role of MgO in the AHE sign change is interface effect. Varying the thickness of the Py will not change the sign of the AHE in this structure but the magnetic anisotropy of the structure does change as the Py thickness changes. Thin film samples naturally possess in plane magnetic anisotropy. Perpendicular magnetic anisotropy is not obtained in this structure but the in plane magnetic anisotropy is weakest when the thickness of the Py layer is about 1.6nm, the sample at this stage almost shows the out of plane magnetic anisotropy. After replacing the Ta capping layer by other materials, some materials also show the sign change effect in AHE and some not. The Hf, Ru, Pt, Cu capping layer will change the sign of the AHE while W and Al will not change the sign of the AHE. The Py surface oxidation and the carrier charge type in the HM capping layer is not the reason for the sign change in AHE because no sign change is observed without the presence of the MgO underlayer. The sign of spin Hall angle of the various HM capping layers also cannot explain the sign change in Hall resistivity in the trilayer structures. I propose several possible reasons for the sign change in AHE observed in the

trilayer structures. One is intrinsic contribution to the AHE due to Berry curvature contribution. Another is the surface scattering and interface scattering effects which can be significant in the thin film samples. The Berry curvature can change sign when the thickness of certain HM capping layer changes due to strong spin orbit couplings and orbital hybridization. This is demonstrated by the ARS measurement and the fact that no sign change is observed in Al capped samples which have small spin orbit coupling. The relative contribution from the above mechanisms can also change which might have different sign intrinsically. These can all make the sign of the AHE change in the structure I made.

The second part is about induced nonzero spin polarization in the Pt layer when grown on YIG substrate. The YIG is a ferrimagnetic insulator. The Pt which intrinsically has zero spin polarization due to nonmagnetic property, shows nonzero spin polarization when grown on YIG. This nonzero spin polarization disappears when a 1.2nm NiO layer is inserted between the Pt layer and YIG. The spin polarization of the Pt layers is even higher when a 1.2nm Cu layer or 0.6nm ultrathin NiO layer is inserted between Pt and YIG. The spin polarization of the 0.6nm ultrathin NiO inserted sample increases with increasing temperature while the one with Pt grown directly on YIG shows no temperature dependence. There are two reasons for the induced spin polarization in the Pt layer. One is the magnetic proximity effect at the interface while another is the spin pumping from the YIG layer into the Pt

layer. The NiO and Cu insertion can effectively block the magnetic proximity effect while nonzero spin polarization can still be observed in the Pt layer when the NiO layer is thin enough. This demonstrates that at least the spin pumping makes significant contribution to the induced spin polarization in the Pt layer. The magnons in the NiO layer might even enhance the spin current transport between the YIG and Pt which is demonstrated by the even larger spin polarization in the Pt layer and the temperature dependence.

The last part I completed is the perpendicular magnetic anisotropy(PMA) in the Ru/Co/Ru trilayer structures. The PMA can be obtained in the Ru/Co/Ru trilayer with proper thickness engineering of the magnetic Co layer as well as the base layer and the capping layers. PMA is preserved in multilayer structures with repetitions up to 6. There are two possible reasons for the PMA observed in thin film structures, one is the spin orbit coupling which is the orbital hybridization between different atoms at the interface, the other is the lattice strain induced by the lattice mismatch. I studied the origin of the PMA by Andreev reflection spectroscopy method. I did the magnetic field orientation dependence of the ARS differential conductivity for the sample. If the PMA originates from the spin orbit coupling, differential conductance will change with different magnetic field orientation while if the PMA originates from lattice strain, it will not change. In my measurement,

no profound change is observed which implied that the PMA is due to lattice strain.

6.2 Future Works

In the first part, clear mechanisms for the sign change in the trilayer structure is still not found yet. Berry curvature calculations can be done to find out exactly the value of the Berry curvature with different HM capping layer thickness to find out the contribution from it. Also, how to quantitatively measure and separate the contribution from surface scattering, interfacial scattering and the side jump effect is still a challenge. One possible method is to do the scaling analysis of the samples[5]. The scaling analysis is a good way to separate the contribution from intrinsic and extrinsic mechanisms. The Py layer is NiFe alloy which is composed mostly of Ni and Fe. We can replace Py layer by pure Ni and Fe layer respectively to find out which element contribute to the sign change in AHE or the alloy is crucial for sign change in AHE. We have shown that the magnetic anisotropy of the structure tends to point more to out of plane after annealing or left in ambient environment for 5 months. This can be attributed to interface change. Detailed interface quality is still not known in the trilayer structure. We can do transmission electron microscope measurement to find out the quality of the interface in the trilayers. In the second part, we can do more detailed thickness dependence of the NiO insertion layer to find out the cut of

thickness of the spin current pumping and temperature dependence analysis. In the last part, we can use the magnetic force microscope to find out the domain patterns in the PMA trilayer samples and its evolution with external magnetic field.

REFERENCE

1. Yugui Yao et al., "Theoretical Evidence for the Berry-Phase Mechanism of Anomalous Hall Transport: First-principles Studies on $CuCr_2Se_{4-x}Br_x$", Phys. Rev. B 75, 020401(R) (2007)
2. Huei-Ru Fuh et al., "Intrinsic anomalous Hall effect in nickel: A GGA + U study", PHYSICAL REVIEW B 84, 144427 (2011).
3. H. L. Wang et al., "Scaling of Spin Hall Angle in 3d, 4d, and 5d Metals from $Y_3Fe_5O_{12}$/Metal Spin Pumping", PRL 112, 197201 (2014).
4. Di Xiao et al., "Berry phase effects on electronic properties", Reviews of Modern Physics, volume 82, July–September 2010
5. Yuan Tian et al., "Proper Scaling of the Anomalous Hall Effect", PRL 103, 087206 (2009)

REFERENCES

Rolf E. Hummel, “Electronic Properties of Materials.”

Stephen Blundell, “Magnetism in Condensed Matter.”

Charles Kittel, “Introduction to Solid State Physics.”

Robert O’Handley, “Modern Magnetic Materials: Principles and Applications.”

Soshin Chikazumi, “Physics of Ferromagnetism.”

Naoto Nagaosa et al., “Anomalous Hall effect,” reviews of modern physics, volume 82, April–June 2010

J. E. Hirsch, “Spin Hall effect”, Phys. Rev. Lett. 83, 1834 (1999)

M. I. Dyakonov and V. I. Perel, “Current-induced spin orientation of electrons in semiconductors”, Phys. Lett. A35, 459 (1971)

M. Born, “Atomic Physics”, Dover Publications Inc, New York (1989)

R. Karplus, J. M. Luttinger, “Hall effect in ferromagnetics” Phys. Rev. 95, 1154 (1954)

M. V. Berry, “Quantal phase factors accompanying adiabatic changes”, Proc. R. Soc. Lond. A 392, 45 (1984)

M. C. Chang and Q. Niu, “Berry phase, hyperorbits, and the Hofstadter spectrum: Semiclassical dynamics in magnetic Bloch bands” Phys. Rev. B 53, 7010 (1996)

G. Sundaram and Q. Niu, “Wave-packet dynamics in slowly perturbed crystals:

Gradient corrections and Berry-phase effects” Phys. Rev. B 59, 14915 (1999)
A. Fert and A. Friederich, “Skew scattering by rare-earth impurities in silver, gold, and aluminum” Phys. Rev. B 13, 397 (1976)

L. Berger, “Side-Jump Mechanism for the Hall Effect of Ferromagnets” Phys. Rev. B 2, 4559 (1970).

N. A. Sinitsyn, "Semiclassical theories of the anomalous Hall effect" J. Phys.: Condens. Matter 20, 023201 (2008).

Jessica Gifford, "Andreev Reflection Spectroscopy: Theory and Experiment."

Tinkham et al., "Introduction to Superconductivity."

W Vavra et al., "Magnetoresistance and Hall effect in epitaxial Co-Au superlattices," Phys. Rev. B 42, 4889 (1990).

F. Tsui et al., "Scaling Behavior of Giant Magnetotransport Effects in Co/Cu Superlattices," PhysRevLett.72.740 (1994)

C. L. Canedy, "Extraordinary Hall effect in (111) and (100)-orientated Co/Pt superlattices," Journal of Applied Physics 81, 5367 (1997)

W. J. Xu et al., "Anomalous Hall Effect in Fe/Gd Bilayers," EPL (Europhysics Letters), Volume 90, Number 2 (2010)

S. N. Song et al., "Anomalous Hall effect in (110)Fe/(110)Cr multilayers," Appl. Phys. Lett. 59, 479 (1991)

S. L. Zhang et al., "Large enhancement of the anomalous Hall effect in Co/Pt multilayers sandwiched by MgO layers," Appl. Phys. Lett. 97, 222504 (2010)

J. Zhao et al., "Large extraordinary Hall effect in [Pt/Co]5/Ru/[Co/Pt]5 multilayers," Physical Review B 81, 172404 (2010)

Z. B. Guo et al., "Effects of surface and interface scattering on anomalous Hall effect in Co/Pd multilayers," Physical Review B 86, 104433 (2012)

Xinli Kou et al., "Magnetic anisotropy and anomalous Hall effect of ultrathin Co/Pd bilayers," Journal of Applied Physics 112 093915 (2012)

O. Shaya et al., "Extraordinary Hall effect in Co-Pd bilayers," Journal of Applied Physics 102, 043910 (2007)

Sangrok Kim et al., "Magnetic properties of Pd/Co multilayer films studied by Hall effect," Journal of Applied Physics 73, 6344 (1993)

D. Rosenblatt et al., "Reversal of the extraordinary Hall effect polarity in thin Co/Pd multilayers," Appl. Phys. Lett. 96, 022512 (2010)

V. Keskin et al., “Temperature and Co thickness dependent sign change of the anomalous Hall effect in Co/Pd multilayers: An experimental and theoretical study,” Appl. Phys. Lett. 102, 022416 (2013)

Y. M. Lu et al., “Ultrasensitive anomalous Hall effect in SiO2/Fe-Pt/SiO2 sandwich structure films,” Appl. Phys. Lett. 100, 022404 (2012)

T. Y. Chen et al., “Pronounced effects of additional resistance in Andreev reflection spectroscopy”, Physical Review B 81, 214444 (2010)

Di Xiao et al., “Berry phase effects on electronic properties”, Reviews of Modern Physics, volume 82, July–September 2010

Yugui Yao et al., “Theoretical Evidence for the Berry-Phase Mechanism of Anomalous Hall Transport: First-principles Studies on CuCr2Se4−xBrx”, Phys. Rev. B 75, 020401(R) (2007)

F. D. M. Haldane, “Berry Curvature on the Fermi Surface: Anomalous Hall Effect as a Topological Fermi-Liquid Property”, Phys. Rev. Lett. 93, 206602 (2004)

Yugui Yao, et. al., “First principles calculation of anomalous Hall conductivity in ferromagnetic bcc Fe”, Phys. Rev. Lett. 92, 037204 (2004).

Huei-Ru Fuh et al., “Intrinsic anomalous Hall effect in nickel: An GGA+U study”, PHYSICAL REVIEW B 84, 144427 (2011).

David J. Griffiths, “Introduction to Quantum Mechanics”, Prentice Hall (1995).

Qi Wang et al., “Large intrinsic anomalous Hall effect in half-metallic ferromagnet $Co_3Sn_2S_2$ with magnetic Weyl fermions”, Nature Communications volume 9, Article number: 3681 (2018)

Wei-li Lee et al., “Dissipationless Anomalous Hall Current in the Ferromagnetic Spinel $CuCr_2Se_{4-x}Br_x$”, Science. 2004 Mar 12;303(5664):1647-9.

A. Fert et al., “Left-Right Asymmetry in the Scattering of Electrons by Magnetic Impurities, and a Hall Effect”, Phys. Rev. Lett. 28, 303 (1972)

T. Jungwirth et al., “Anomalous Hall effect in ferromagnetic semiconductors”, Phys Rev Lett. 2002 May 20;88(20):207208.

N. P. ONG et al., “Geometry and the Anomalous Hall Effect in Ferromagnets”.
Xinjie Wang et al., “Fermi-surface calculation of the anomalous Hall conductivity”, Phys. Rev. B 76, 195109 (2007)

Zhong Fang et al., “The Anomalous Hall Effect and Magnetic Monopoles in Momentum Space”, *Science* Vol. 302, Issue 5642, pp. 92-95 03 Oct 2003.

D. L. Smith, “Thin film deposition”, McGraw-Hill, Inc., New York (1995)

Donald M. Mattox, “Handbook of Physical Vapor Deposition (PVD) Processing”, William Andrew, (2010)

John F. O’Hanlon, “A User’s Guide to vacuum technology”, John Wiley & Sons, New York, (2003)

Oura, K. Lifshits, et al., “Surface Science: An Introduction.” Springer-Verlag. ISBN 3-540-00545-5 (2003).
Feldman, L.C, et al., “Materials Analysis by Ion Channeling.” Academic Press (1982).

Feldman, L.C. et al., “Fundamentals of Surface and Thin Film Analysis.” Prentice-Hall (1986).

Sarvesh Kumar et al., “Preparation of Gold Target through Electron Vapor Deposition and " Paras " the Rutherford Back Scattering Experimental setup.” Conference: NCIL 2015, Volume: 1

S. Foner, “Versatile and Sensitive Vibrating-Sample Magnetometer” Rev. Sci. Instrum. 30, 548 (1959).

“Lakeshore Model 7304 Vibrating Sample Magnetometer” Manual.

Chandra, H., et al. Open-Source Automated Mapping Four-Point Probe. Materials 2017, 10(2), 110.

Heaney, Michael B. “Electrical Conductivity and Resistivity.” Electrical Measurements, Signal Processing, and Displays. Ed. John G Webster. CRC Press, 2003. 7-1.

C. Christides et al., “Polarity of anomalous Hall effect hysteresis loops in $[Pt/Co]_{15}$/AF/$[Co/Pt]_{15}$ (AF=FeMn, NiO) multilayers with perpendicular anisotropy”, Journal of Applied Physics 97, 013901 (2004).

C. L. Canedy et al., “Large magnetic moment enhancement and extraordinary Hall effect in Co/Pt superlattices”, Phys. Rev. B 62, 508 (2000).

J. Caulet et al., “Influence of spin polarized Pt on the extraordinary Hall effect in sputtered Pt/Au/Co/Pt sandwiches”, Journal of Magnetism and Magnetic Materials, Volume 198, Issue 1-3, p. 318-320 (1999).

Zhiyong Wang et al., “Proximity-Induced Ferromagnetism in Graphene Revealed by the Anomalous Hall Effect”, PRL 114, 016603 (2015).

Sibylle Meyer et al., “Anomalous Hall effect in YIG/Pt bilayers”, Applied Physics Letters 106, 132402 (2015).

Xiao Liang et al., “Magnetic Proximity Effect and Anomalous Hall Effect in Pt/$Y_3Fe_{5-x}Al_xO_{12}$ Heterostructures”, PHYSICAL REVIEW APPLIED 10, 024051 (2018).

S. Monso et al., “Crossover from in-plane to perpendicular anisotropy in Pt/CoFe/AlOx sandwiches as a function of Al oxidation: A very accurate control of the oxidation of tunnel barriers”, s, Appl. Phys. Lett. 80 (2002) 4157.

B. Rodmacq et al., “Crossovers from in-plane to perpendicular anisotropy in magnetic tunnel junctions as a function of the barrier degree of oxidation”, J. Appl. Phys. 93 (2003) 7513.

A. Monchon et al., “Analysis of oxygen induced anisotropy crossover in Pt/Co/MOx trilayers”, J. Appl. Phys. 104 (2008) 043914.

B. Rodmacq et al., “Influence of thermal annealing on the perpendicular magnetic anisotropy of Pt/Co/AlO_x trilayers”,Phys. Rev. B 79 (2009) 024423.

L. E. Nistor et al., “Correlation between perpendicular anisotropy and magnetoresistance in magnetic tunnel junctions”, IEEE Trans. Magn. 46 (2010) 1412

S. Ikeda et al., “A perpendicular-anisotropy CoFeB–MgO magnetic tunnel junction”,Nature Mater. 9 (2010) 721.

A. Manchon et al., “X-ray analysis of oxygen-induced perpendicular magnetic anisotropy in Pt/Co/AlOx trilayers”, s, J. Magn. Magn. Mater. 320 (2008) 1889.

H. X. Yang et al., “Switching characteristics of submicrometer magnetic tunnel junction devices with perpendicular anisotropy”, y, J. Appl. Phys. 97 (2005) 10C919.

H. L. Wang et al., “Scaling of Spin Hall Angle in 3d, 4d, and 5d Metals from $Y_3Fe_5O_{12}$/Metal Spin Pumping”, PRL 112, 197201 (2014).
Sibylle. Meyer et al., “Anomalous Hall effect in YIG | Pt bilayers”, Appl. Phys. Lett. 106, 132402 (2015).

Y. M. Lu et al., “Pt Magnetic Polarization on $Y_3Fe_5O_{12}$ and Magnetotransport Characteristics”, PRL 110, 147207 (2013).

S. Y. Huang et al., “Transport Magnetic Proximity Effects in Platinum”, PRL 109, 107204 (2012).

B. F. Miao et al., “Physical Origins of the New Magnetoresistance in Pt/YIG”, PRL 112, 236601 (2014).

H. Nakayama et al., “Spin Hall Magnetoresistance Induced by a Nonequilibrium Proximity Effect”, PRL 110, 206601 (2013).

B. Heinrich et al., “Spin Pumping at the Magnetic Insulator (YIG)/Normal Metal (Au) Interfaces”, PRL 107, 066604 (2011).

Natalia Rinaldi-Montes et al., “Size effects on the Néel temperature of antiferromagnetic NiO nanoparticles”, AIP Advances 6, 056104 (2016).

Yu Wang et al., “Voltage-Controlled Sensitivity of the Spin Seebeck Effect in $Pt/Y_3Fe_5O_{12}/MgO/(PbMg_{1/3}Nb_{2/3}O_3)_{0.7}(PbTiO_3)_{0.3}$ Multiferroic Heterostructures”, PHYSICAL REVIEW APPLIED 10, 014004 (2018).

Weiwei Lin et al., “Enhancement of Thermally Injected Spin Current through an Antiferromagnetic Insulator”, PRL 116, 186601 (2016).

Weiwei Lin et al., “Electrical Detection of Spin Backflow from an Antiferromagnetic Insulator/$Y_3Fe_5O_{12}$ Interface”, PRL 118, 067202 (2017).

Kai Chen et al., “Temperature dependence of angular momentum transport across interfaces”, PHYSICAL REVIEW B 94, 054413 (2016).

M. A. Prosnikov et al., “Magnetic dynamics and spin-phonon coupling in the antiferromagnet Ni_2NbBO_6”, PHYSICAL REVIEW B 98, 104404 (2018).

L. Wang et al., “Co1-xFexS2: A Tunable Source of Highly Spin-Polarized Electrons”, PRL 94, 056602 (2005).

T. Y. Chen et al., “Enhanced Curie temperature and spin polarization in Mn4FeGe3”, Appl. Phys. Lett. 91, 142505 (2007).

S. X. Huang et al., “Spin polarization of amorphous CoFeB determined by point-contact Andreev reflection”, Appl. Phys. Lett. 92, 242509 (2008).

T. Y. Chen et al., “Determination of superconducting gap of $SmFeAsF_xO_{1-x}$ superconductors by Andreev reflection spectroscopy”, Physica C: Superconductivity, Volume 469, Issues 9–12 (2009).

Shashi K. Upadhyay et al., “Probing Ferromagnets with Andreev Reflection”, Phys. Rev. Lett. 81, 3247 (1998)

David Jiles, “Introduction to Magnetism and Magnetic Materials”.

B. D. Cullity et al., “Introduction to Magnetic Materials”.

N. Nakajima et al., “Perpendicular Magnetic Anisotropy Caused by Interfacial Hybridization via Enhanced Orbital Moment in Co/Pt Multilayers: Magnetic Circular X-Ray Dichroism Study”, Phys. Rev. Lett. 81, 5229 (1998).

D. Weller et al., “Orbital magnetic moments of Co in multilayers with perpendicular magnetic anisotropy”, Phys. Rev. B 49, 12888 (1994).

Alexander G Kolesnikov et al., “Enhancement of perpendicular magnetic anisotropy and coercivity in ultrathin Ru/Co/Ru films through the buffer layer engineering”, J. Phys. D: Appl. Phys. 49 (2016).

K. Ounadjela et al., “Perpendicular anisotropy and antiferromagnetic coupling in Co/Ru strained superlattices”, Phys. Rev. B 45, 7768 (1992).

Z. Zhang et al., “Angular dependence of ferromagnetic resonance in exchange-coupled Co/Ru/Co trilayer structures”, Phys. Rev. B 50, 6094 (1994).

P. J. H. Bloemen et al., “Oscillatory interlayer exchange coupling in Co/Ru multilayers and bilayers”, Phys. Rev. B 50, 13505 (1994).

Bharati Tudu et al., “Effect of Composition and Thickness on the Perpendicular Magnetic Anisotropy of (Co/Pd) Multilayers”, Sensors (Basel). 2017 Dec; 17(12): 2743.

Ja-Bin Lee et al., “Thermally robust perpendicular Co/Pd-based synthetic antiferromagnetic coupling enabled by a W capping or buffer layer”, Scientific Reports volume6, Article number: 21324 (2016).

T. Kato et al., “Perpendicular Anisotropy and Gilbert Damping in Sputtered
Co/Pd Multilayers”, IEEE TRANSACTIONS ON MAGNETICS, VOL. 48, NO. 11, NOVEMBER 2012.

Enlong Liu et al, “Seed Layer Impact on Structural and Magnetic Properties of [Co/Ni] Multilayers with Perpendicular Magnetic Anisotropy”, Journal of Applied Physics 121, 043905 (2017).

M. Arora et al., “Origin of perpendicular magnetic anisotropy in Co/Ni multilayers”, Phys. Rev. B 96, 024401 (2017).

Bernd Zimmermann et al., “Anisotropy of Spin Relaxation in Metals”, PRL 109, 236603 (2012).

Bernd Zimmermann et al., “Fermi surfaces, spin-mixing parameter, and colossal anisotropy of spin relaxation in transition metals from ab initio theory”, PHYSICAL REVIEW B 93, 144403 (2016).

Petra Högl et al., “Magnetoanisotropic Andreev Reflection in Ferromagnet-Superconductor Junctions”, PRL 115, 116601 (2015).

Jun Okabayashi et al., “Anatomy of interfacial spin-orbit coupling in Co/Pd multilayers using X-ray magnetic circular dichroism and first-principles calculations”, Scientific Reportsvolume 8,
Article number: 8303 (2018)